Electrochemical modeling of degradation effects at a wide range of temperatures for lithium ion polymer batteries

by

Xinchen Zhao

A dissertation submitted to the Graduate Faculty of
Auburn University
in partial fulfillment of the
requirements for the Degree of
Doctor of Philosophy

Auburn, Alabama
December 15, 2018

Key words: Degradation, Lithium ion batteries, Lithium plating, Lithium stripping, Reduced order model, Side reaction

Copyright 2018 by Xinchen Zhao

Approved by

Song-Yul Choe, Chair, Professor of Mechanical Engineering
Jeffrey Fergus, Professor of Materials Engineering
Roy Knight, Professor of Mechanical Engineering
John Hung, Professor of Electrical Engineering

Abstract

The durability of lithium-ion batteries (LiBs) drops gradually undergoing both storage and prolonged cycling conditions, which is greatly affected by the operating conditions, particularly temperatures. At high temperatures, side reaction that takes place between lithium ions and electrolyte solvents to form the solid electrolyte interphase (SEI) layer is the primary cause for degradation. At low temperatures, especially under charging, lithium ions are prone to deposit as lithium metal on instead of intercalating into the solid matrix of anode, known as “lithium plating” that becomes the predominant reason for degradation. At discharging, extra lithium ions can be released from the plated lithium resulting in the partial capacity reversed, known as “lithium stripping”.

An integrated physics-based reduced order model (ROM) considering degradation effects of side reaction and lithium plating/stripping at a wide range of temperatures is proposed and validated against experiments for both fresh and cycled LiBs, which has shown the capability of predicting the cell electrochemical performances and degradation, such as capacity fade, power fade and impedance rise etc. The degradation effects, including loss of recyclable lithium ions, loss of active material, growth of SEI and deposit layer, and the consumption of electrolyte solvents are considered at the entire temperature ranges. The growth of plated lithium and secondary SEI are added as extra sources of degradation at low temperatures. The model is capable of estimating capacity and power as a function of cycle number with an overall accuracy of 3% in the case that the capacity fade is less than 30%.

Acknowledgements

I would like to express my deep appreciation to my advisor, Dr. Song-Yul Choe, for giving me the opportunity to get involved in this research project. His wise suggestions and generous guidance assisted me to the fulfillment of my study. Without his valuable suggestions and detailed corrections to my papers and dissertation, I would hardly finish my research program. I also would like to acknowledge to my committee members, Dr. Roy Knight, Dr. John Hung and Dr. Jeffrey Fergus, for their continuous instructions and encouragement, which enabled me to develop a deep understanding in the research area. Last but not least, I would like to express my gratitude to my parents, Xiaopei Zhao and Xuefeng Chen, and my husband, Dr. Zhao Wu, for their unselfish support of my academic endeavor.

Table of Contents

List of Tables

List of Figures

List of Symbols

A	sandwich area of the cell (m^2)
a_s	specific surface area of electrode (m^{-1})
c	ion concentration (mol L^{-1})
D	diffusion coefficient(m^2 s^{-1})
F	Faraday constant (96,487 C mol^{-1})
I	current of the cell (A)
i_0	exchange current density of intercalation (Am^{-2})
j^{Li}	reaction rate of intercalation (Am^{-3})
k_s	isolation coefficient due to SEI
l	thickness of the micro cell (cm)
Q	capacity of the cell (Ah)
q	amount of ion loss caused (Ah)
R	resistance (Ω m^2) or universal gas constant (8.314 J mol^{-1} K^{-1})
R_s	radius of spherical electrode particle (m)
r	coordinate along the radius of electrode particle (m)
T	cell temperature (K)
t	time (s)
U	potential (V)
V	voltage (V) or volume of the composite electrode (m^3)

$\tilde{V}$	molar volume (m^3 mol^{-1})
x	stoichiometric number of the anode
y	stoichiometric number of the cathode

Greek symbols

α	transfer coefficient for an electrode reaction
δ	thickness (m)
ε	volume fraction of a porous medium
ϕ	potential (V)
η	overpotential of electrode reaction (V)
κ	ionic conductivity (S m^{-1})
σ	conductivity (S m^{-1})
λ	fraction of plated lithium to form secondary SEI

Subscripts

a	anodic
act	actual
aged	aged cell
ave	average value
c	cathodic
e	electrolyte phase
eq	equilibrium
error	error

exp	experiment
fresh	fresh cell
film	surface film including SEI and metallic lithium
ini	initial
Li	metallic lithium
main	main reaction
max	maximum
p	lithium plating
plating	lithium plating
Q	capacity
r	radial direction in electrode particle
s	solid phase
side	side reaction
sim	simulation
surf	electrode particle surface
0%	0% SoC
100%	100% SoC
+	positive electrode (cathode)
-	negative electrode (anode)

Superscripts

eff	effective
Li	lithium ion
Θ	standard

List of Abbreviations

AM	active material
BMS	battery management system
BoL	beginning-of-life
BV	Butler-Volmer
CC	constant current
CTL	charge transfer limitation
CV	constant voltage
DL	deposit layer
EC	ethylene carbonate
ECM	equivalent circuit model
EIS	electrochemical impedance spectroscopy
EKF	Extended Kalman filter
EoC	end-of-charge
EoD	end-of-discharge
EoL	end-of-life
EV	electric vehicle
FOM	full order model
FTIR	Fourier Transform Infrared Spectroscopy
KF	Kalman filter

LCO lithium cobalt oxide

LCP lithium cobalt phosphate

LFP lithium iron phosphate ($LiFePO_4$)

LFSF lithium iron fluorosulfate

LiB lithium-ion battery

LMO lithium manganese oxide

LTS lithium titanium sulfide

MPC model predictive control

MTL mass transfer limitation

NCA nickel cobalt aluminum oxide

NCM nickel cobalt manganese oxide

NMR nuclear magnetic resonance

NN neural network

OCV open-circuit voltage (V)

PDE partial differential equation

PF particle filter

POD proper orthogonal decomposition

ROM reduced order model

RPT reference preparation test

SOC state-of-charge

SOH state-of-health

SEI solid electrolyte interphase

SEM Scanning Electron Microscopy

SPM single particle model

TEM transmission electron microscopy

XPS X-Ray Photoelectron Spectroscopy

XRD X-Ray Diffraction

Chapter 1. Introduction

1.1 Background

With the rapid development of science and technology, our society is facing plenty of major challenges, such as energy efficiency, climate change and energy sustainability, global as well as local. On a global level, our choices of transportation solutions are closely related to the fuel consumption which are directly linked to the emission of carbon dioxide (CO_2). On a local level, the major challenge is to transport the citizens and goods in a high efficient and low-noise way. Different types of electric vehicles (EVs), including hybrid, full-electric, and plug-in hybrid EVs, could make contributions to help solve the aforementioned concerns. The selection of battery is the core part of the design of EVs, which should satisfy the requirements such as the balance between energy and power, thermal and mechanical specifications, and manufacturing costs etc. Currently, the most suitable battery technology for EVs, having the characteristics of both high-energy and high-power density, is the lithium-ion battery (LiB) technology.

Since LiBs are the most satisfactory choice of electrochemical energy storage devices, the selection of the active material of electrodes is of great significance. Graphite is the most commonly used active material of the negative electrode, while the most affecting factor is the active material of positive electrode. Fig. 1 depicts the approximate range of average discharge potentials and experimental specific capacity of the intercalation-type cathodes, including lithium

cobalt oxide (LCO), lithium manganese oxide (LMO), nickel cobalt manganese oxide (NCM), nickel cobalt aluminum oxide (NCA), lithium cobalt phosphate (LCP), lithium iron phosphate (LFP), lithium iron fluorosulfate (LFSF) and lithium titanium sulfide (LTS). [1] LFP, due to its high electrochemical and thermal stability[2], attracts great interests of researchers.

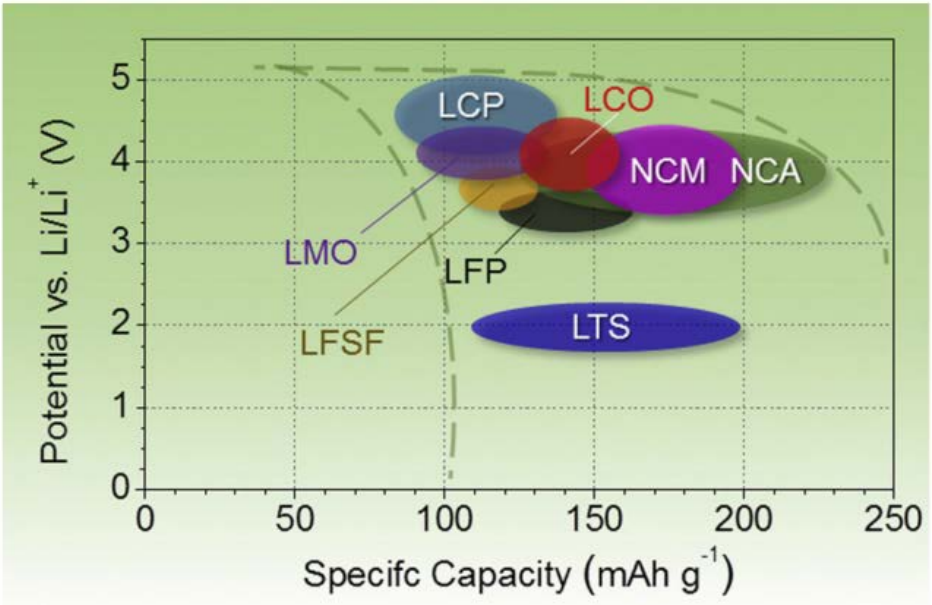

Fig. 1 Average discharge potentials and experimental specific capacity of cathodes [1]

1.2 Working principles of LFP/graphite cells

The elementary unit of a LFP/graphite single cell is a sandwich-like structured electrochemical microcell which is constructed by two composite electrodes, separator and two current collectors, as shown in Fig. 2. The composite electrode is mainly fabricated by electrode particles, electrolyte and binder. When the cells are discharged, reduction and oxidation reactions take place at the anode and cathode, respectively. The lithium ions de-intercalated from the anode

particles transport through the electrolyte to the cathode inside the cell while the electrons transport through the external circuit. Likewise, the reverse reaction takes place at charging.

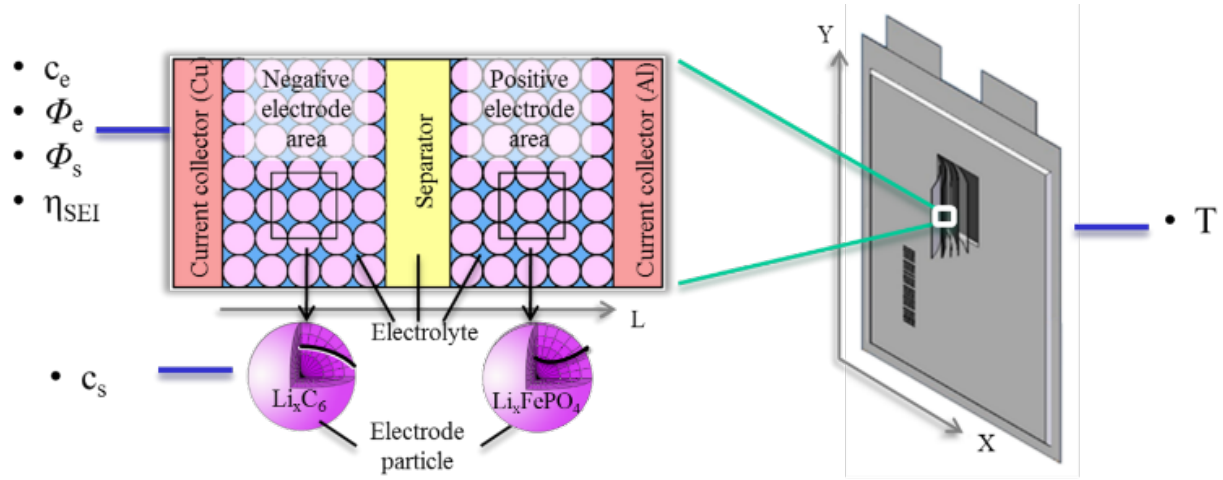

Fig. 2 Model set-up of a pouch-type single cell and a microcell [3]

State-of-charge (SOC) is defined as the ratio of releasable charges over the maximum number of charges stored in a LiB with a unit of percentage. At low SOC, the lithium-ion (Li^+) concentration of cathode is larger than that of anode. Under charging, the transportation of lithium ions from cathode to anode leads to a decrease of Li^+ concentration on cathode, as shown in Fig. 3. Then at full SOC, the Li^+ concentration of anode will reach the highest value, while that of cathode to the lowest.

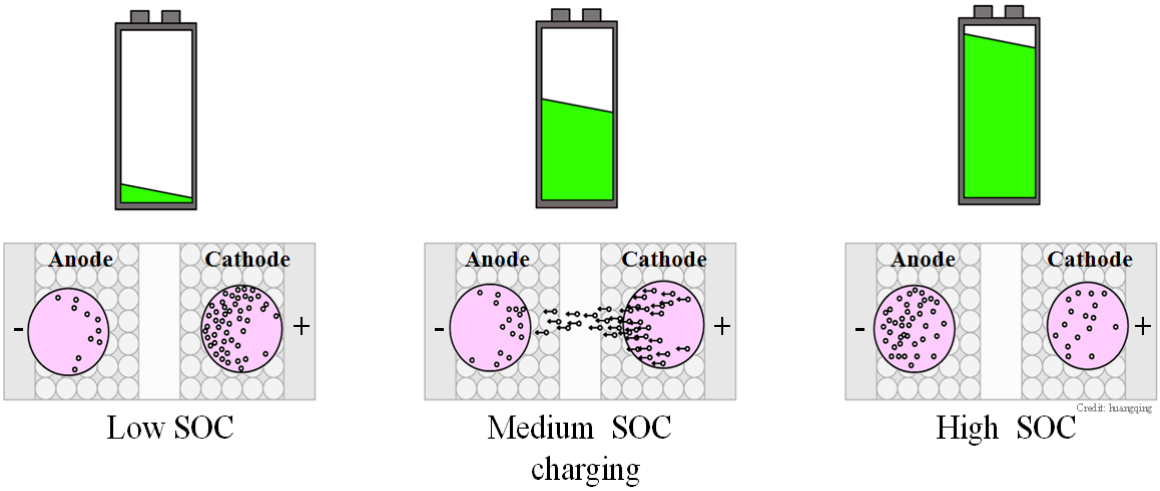

Fig. 3 Relationship between lithium-ion concentration and SOC on electrodes (by Meng Xiao)

1.3 Characteristics of LFP cathode

Compared with the electrodes embedded by Ni, Mn, Co, LFP based electrodes have the special characteristics of two-phase transition and path dependence in both charge and discharge cycles. The coexisting two phases in the cathode particles are lithium-deficient phase ($Li_{\alpha}FePO_4$, α phase) and lithium-rich phase ($Li_{1-\beta}FePO_4$, β phase).

1.3.1 Two-phase transition

The characteristic of two-phase transition is represented as a plateau in the voltage profile. Fig. 4 shows the schematic diagram of a shrinking-core model to describe phase transition during charge and discharge of LFP electrode. At the beginning of discharge, only α phase exists in the fully charged LFP particles. When discharge proceeds, the continuous transport of lithium ions from anode to cathode leads to the increase of the surface concentration of LFP particles. When the Li^+ concentration reaches a certain value, a new phase, β phase, does begin to generate at the

surface of α phase. Then the LFP particles are composed of two layers, α phase in the core and β phase on the shell. It ends when the core is completely consumed. The process of the two-phase transition under charging proceeds in the opposite way, resulting in a core of β phase covered by a shell of α phase.

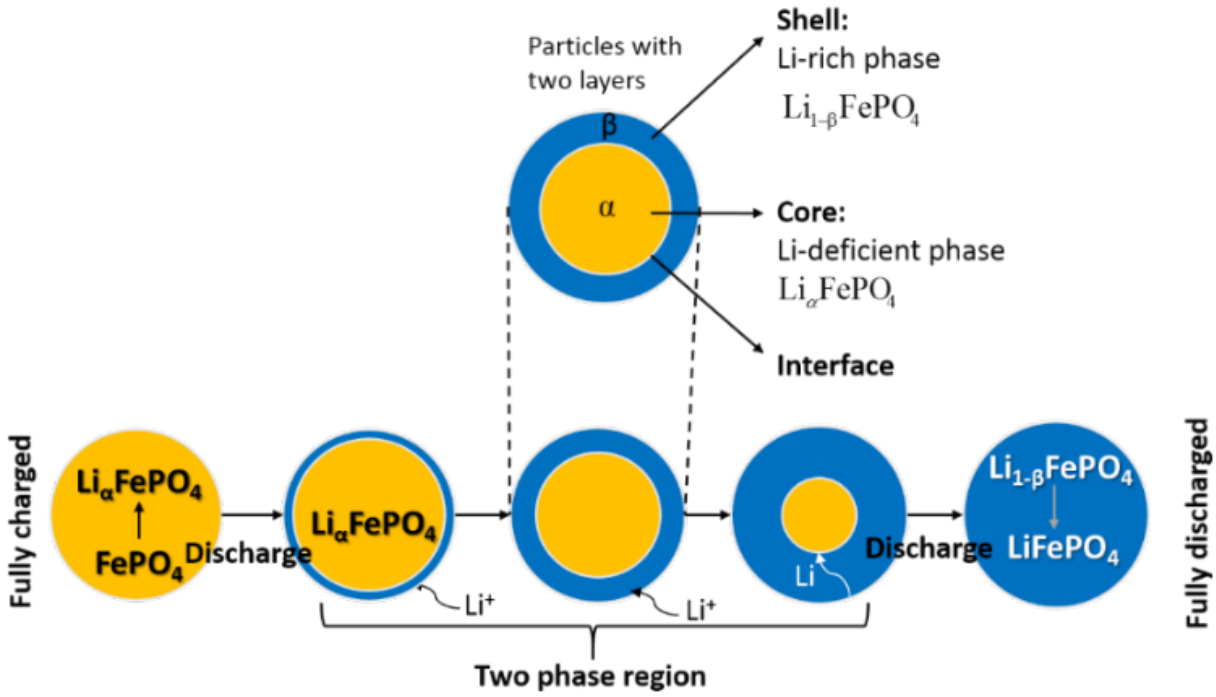

Fig. 4 Schematic diagram of two-phase transition of LFP electrode by a shrinking core

1.3.2 Path dependence

The schematic diagram of the shrinking-core model used to describe the juxtaposition of phases in LFP electrode is shown in Fig. 5. The blue and yellow color represent lithium-rich phase (β phase) and lithium-deficient phase (α phase) of LFP particles, respectively. Path (a) shows a typical charging process with constant current (CC) applied from 0% SOC to 100% SOC. At charging, a core of β phase covered by a shell of α phase is formed. Due to the moving boundary,

α phase on the shell expands while β phase in the core shrinks. The core is completely consumed at the end of charging with only α phase existing in the LFP particles. In path (b), the cell is discharged from the fully charged state, resulting in the formation of core-shell LFP particles, α phase in the core and β phase on the shell. Then the cell is charged from 50% SOC to 100% SOC. A new α phase starts to generate at the surface of particles when the surface Li^+ concentration decreases to a critical value. As charging proceeds, lithium ions transport from the surface through the new α phase to the interface between new α phase and pre-formed β phase, which results in the formation of three-layer coexisting particles with two interfaces. Charging continues until the core is consumed completely. The releasable capacity of LiBs tested in path (a) and path (b) is distinguished from each other.

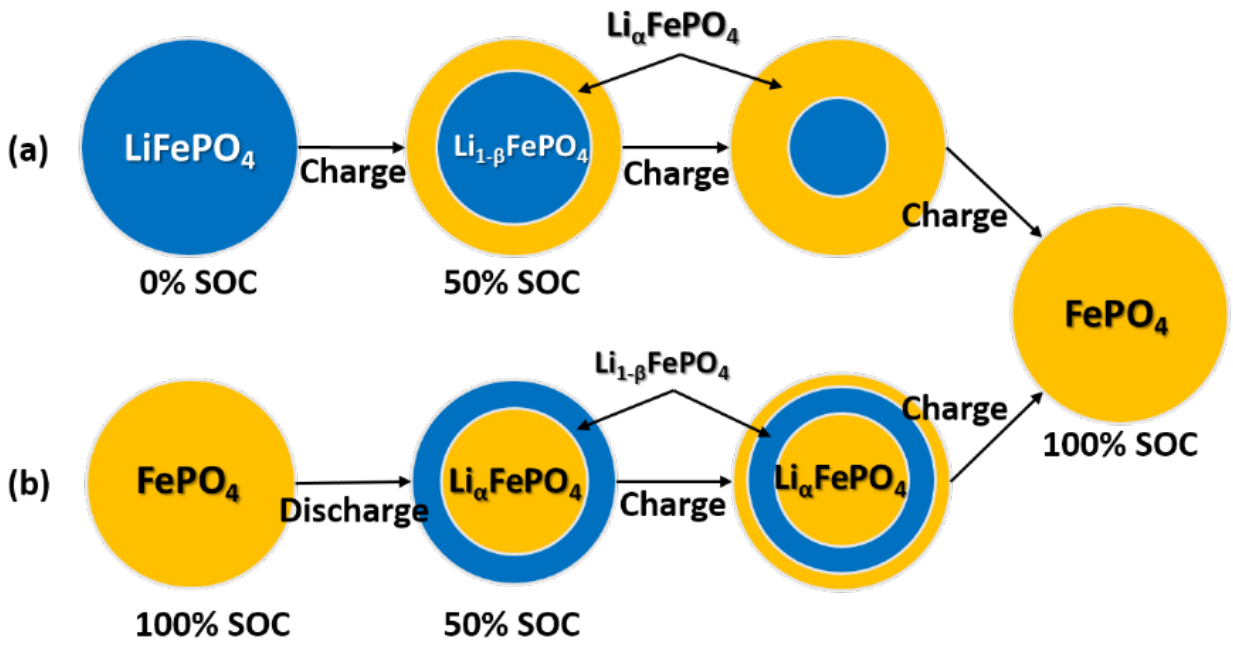

Fig. 5 Schematic diagram of the juxtaposition of phases in LFP particles at different SOCs with different usage history: blue and yellow color for β and α phase, respectively

1.4 Motivation and objectives

Dynamic responses of LiBs are usually required in the design of EVs, including fast charging by high currents, driving patterns of braking and acceleration, and prolonged cycling in normal and harsh environment etc. A robust and reliable battery management system (BMS), which relies on the models, empirical or physical, is used to evaluate the states of LiBs in order to optimize the usage. Considering both the accuracy and time consumption, an electrochemical reduced order model (ROM) can be embedded in the BMS to predict the states of batteries, including terminal voltage, current, temperature, ion concentration and SOC etc. Advanced control technology is applied to eliminate the errors caused by measurements, sensors and noise disturbance to further improve the model accuracy.

However, the lifespan of the LiBs are not as long as those of other mechanical components in the EVs. The degradation is affected by the usage history and operating conditions, particularly temperatures. The schematic diagram of dominant degradation reaction at various operating temperatures is plotted in Fig. 6. At charging, when the temperature is higher than 0°C, side reaction whose effects is accelerated by the elevated temperatures is the predominant cause for degradation. With the decrease of temperature, the influence of side reaction on degradation decreases, while that of lithium plating increases. When the temperature is lower than -20°C (extremely low temperature), lithium plating becomes the key reason of degradation, while side reaction can be neglected. At discharging, lithium stripping at low temperatures, especially extremely low temperatures is the main reaction necessary to be considered. Therefore, understanding the degradation mechanisms and effects on battery performances as a function of temperature is of crucial significance for the safe and durable use of LiBs.

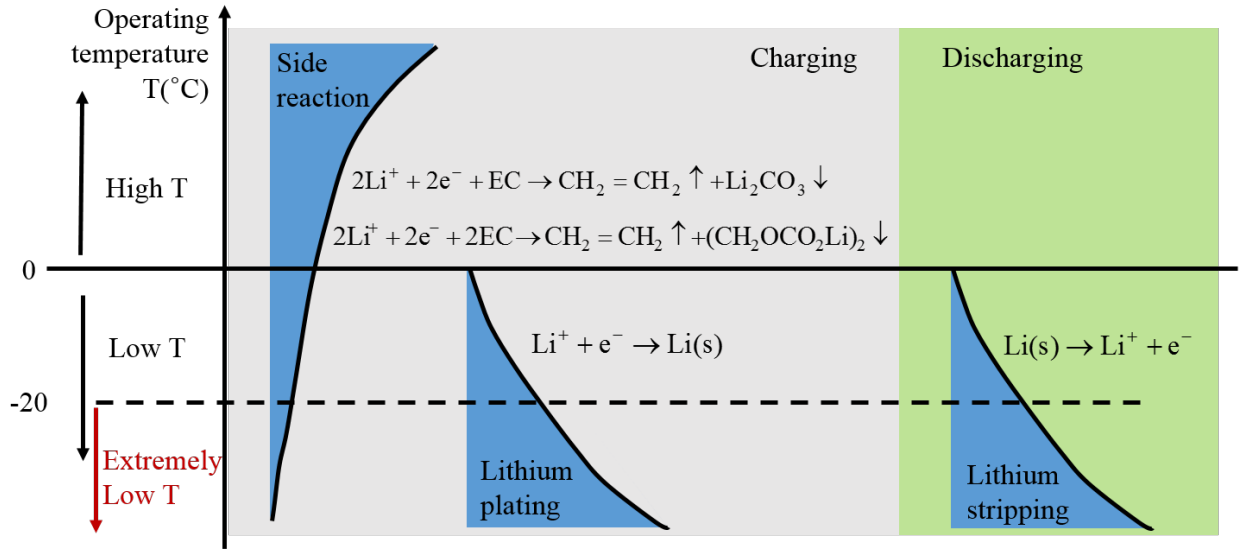

Fig. 6 Schematic diagram of dominant degradation reaction at various operating temperatures

The objective for the dissertation is to mathematically develop and experimentally validate a physics-based model considering degradation effects of both side reaction and lithium plating/stripping on capacity and power fade for LiBs at a wide range of temperatures. The ROM previously developed and validated will be used as a framework for integration of the developing degradation models.

1.5 Dissertation structure

The basic structure of the dissertation is shown as follows.

1. Introduction

   This chapter includes the research background, motivation and objectives.

2. Development of a ROM with the incorporation of the Extended Kalman filter (EKF)

This chapter includes the brief introduction of the electrochemical ROM and the principles of EKF. A hybridized algorithm combing EKF and Coulomb counting is introduced to do SOC estimation more accurately.

3. Development of a physics-based degradation model I considering side reaction at high temperatures

   Side reaction, as the dominant cause of degradation at high temperature, is described using the reformulated Butler-Volmer (BV) equation. The integrated model is developed and validated against experimental measurements at different operating conditions, including temperatures, SOC levels and SOC cycling limits.

4. Development of a physics-based degradation model considering lithium plating/stripping at low temperatures

   The degradation effects of lithium plating and lithium stripping are analyzed using the integrated model based on the reformulated BV equation. The degradation model is developed and validated against the experiments at different operating conditions, including temperatures, charging C-rates and discharging C-rates.

5. Conclusion and future work

Chapter 2. Development of a ROM with incorporation of EKF

2.1 Literature review

The electrochemical behaviors, including intercalation/de-intercalation of lithium ions to/from the electrode, kinetics of chemical reaction taking place at the interface between electrode and electrolyte, ion transportation and diffusion through electrode particles and electrolyte, as well as the state estimation algorithms, are attempted to describe by two methods, the equivalent circuit model (ECM) and the physics-based electrochemical model. Despite the merits of fast calculation with decent accuracy, the high dependence on the experimental data and empirical parameters is a limiting factor of the ECMs. The physics-based electrochemical thermal models have overcome the demerits of the ECMs with the predictive capability of the electrochemical behaviors of the LiBs. The sandwich-like structured model was firstly developed by Doyle [4] based on the concentrated solution theory to simulate galvanostatic charge/discharge behaviors. Srinivasan and Newman [5], Wang et al.[6] and Kavasajjula et al [7] successively proposed a full order model (FOM) based on the concept of a shrinking core to simulate the discharge behaviors of both half and full cells with consideration of phase transformation rate, two-phase interface mobility and diffusion coefficients in both lithium-rich and lithium-deficient phase. The electrochemical behaviors of charging profiles were validated by incorporating Laudau transformation to generate a moving boundary. [8]

In spite of high accuracy, complexity of the parameters and high computational efforts limit the real-time application of FOM. Plenty of reduction methods have been applied to reduce the execution time with accuracy maintained, such as single particle model (SPM) [9], enhanced SPM [10,11], state-variable model [12], reformulated model [13], proper orthogonal decomposition (POD) [14] model and volume averaging model [15]. Furthermore, many attempts have been made to achieve a more accurate SOC estimation based on either open-loop system such as open circuit voltage (OCV) look-up table and Coulomb counting, or closed-loop system that feedbacks through battery models.

OCV method is a directly experimental measurement of the relationship between OCV and SOC. In practical application, due to the disturbance of overpotentials, the measured terminal voltages are different from OCVs. Coulomb counting, as another alternative, calculates SOC by accumulating current over time. However, the accuracy of SOC estimation is limited by the following factors: 1) the measurement error caused by the sensors, 2) inaccurate knowledge of initial SOC, and 3) the varying maximum capacity caused by degradation and low temperature effects. In fact, the open-loop approaches cannot reduce SOC estimation errors at perturbations. Particularly for LFP cells, there is a flat plateau of terminal voltage over a wide range of SOC, where several millivolts of voltage difference corresponding to a variation of 50% SOC. Consequently, neither the OCV-SOC method nor Coulomb counting accomplishes the required accuracy in SOC estimations. Therefore, closed-loop approaches with mathematical models are preferred.

To compensate the model, measurement and initial errors, closed-loop control methods are generally employed, including Kalman filter (KF), EKF [16], particle filter (PF) [17], fuzzy control [18], model predictive control (MPC) and neural networks (NNs) [19]. With a physics-based

model, Santhanagopalan et al. applied the EKF to estimate the SOC using a SPM incorporated into the porous electrode model. [20] Domenico et al. used an average model that considered an average value representing solid ion concentration distribution along the electrode with the incorporation of a linear KF. [21] Klein et al. compared the FOM and ROM and added temperature as a state of the battery model and successfully reduced the SOC estimation error within 3%. [22] Stetzel et al. estimated the SOC and certain internal variables using a one-dimensional ROM with EKF and provided bounds for errors. [23]

In summary, the developed ROM for porous electrode is not only capable of simulating single discharge/charge cycles with applied currents up to 4C-rate, but also multiple cycle tests by dynamic current profiles. In order to obtain a more accurate SOC estimation, a hybrid algorithm combining both classical Coulomb counting method and EKF is proposed.

2.2 Mathematical principles

2.2.1 ROM

The principles of the electrochemical model are summarized in Fig. 7. The mass and charge transfer processes are governed by Fick's law and Ohm's law, respectively. The electrochemical kinetics are governed by the BV equation under consideration of both anodic and cathodic reactions. The polynomial approach, state space approach, simplification and linearization are applied to reduce the order of the equations of ion concentration of electrode phase, ion concentration of electrolyte phase, electric potential of electrolyte phase and current density, respectively.

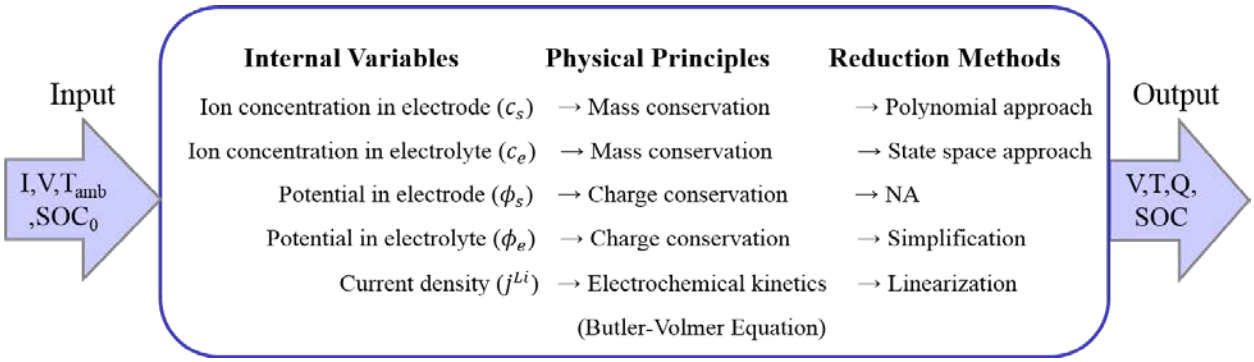

Fig. 7 Schematic diagram of model principles

In the model, the ion behaviors of the two-phase transition and the existence of path dependence are considered by two set of parameters and number of layers coexisting in the LFP particles, respectively. The moving interfaces of the coexisting layers dependent upon the usage history of LiBs have induced a moving boundary problem, or Stephen problem that describes the location of the boundary as a function of time and space, which can be solved by the variable space grid method. The governing equations and their corresponding boundary conditions of both FOM and ROM and the applied reduction methods are summarized in Table 1. The simplified governing equations of ion concentration in the solid particles are shown in Table 2.

Table 1 Governing equations of the FOM and ROM [3]

	FOM	Reduction method	ROM	
Ion concentration in electrode	$\frac{\partial c_s}{\partial t}=\frac{D_{s,\beta}}{r^2}\frac{\partial}{\partial r}\left(r^2\frac{\partial c_s}{\partial r}\right);\ D_{s,\beta}\frac{\partial c_s}{\partial r}\Big\vert_{r=r_1}=0$ $\frac{\partial c_s}{\partial t}=\frac{D_{s,\alpha}}{r^2}\frac{\partial}{\partial r}\left(r^2\frac{\partial c_s}{\partial r}\right);\ D_{s,\alpha}\frac{\partial c_s}{\partial r}\Big\vert_{r=R_s}=\frac{-j^{Li}}{a_sF}$ $\left(c_{s,\alpha\beta}-c_{s,\beta\alpha}\right)\frac{\mathrm{d}r_0}{\mathrm{d}t}=D_{s,\beta}\frac{\partial c_{s,\beta}}{\partial r}\Big\vert_{r=r_0}-D_{s,\alpha}\frac{\partial c_{s,\alpha}}{\partial r}\Big\vert_{r=r_0}$	Polynomial approach	See Table 2	(1)
Ion concentration in electrolyte	$\frac{\partial(\varepsilon_{\mathrm{e}}c_{\mathrm{e}})}{\partial t}=\frac{\partial}{\partial x}\left(D_{\mathrm{e}}^{\mathrm{eff}}\frac{\partial}{\partial x}c_{\mathrm{e}}\right)+\frac{1-t_+^0}{F}j^{\mathrm{Li}}$ $\frac{\partial c_{\mathrm{e}}}{\partial t}\Big\vert_{x=0}=\frac{\partial c_{\mathrm{e}}}{\partial t}\Big\vert_{x=L}=0$	State space approach	$\dot{\mathbf{c}}_{\mathbf{e}}=\mathbf{A}\cdot\mathbf{c}_{\mathbf{e}}+\mathbf{B}\cdot I$ $\mathrm{y}=\mathbf{C}\cdot\mathbf{c}_{\mathbf{e}}+\mathbf{D}\cdot I$	(2)
Ohm's law in electrode	$\frac{\partial}{\partial x}\left(\sigma^{\mathrm{eff}}\frac{\partial}{\partial x}\phi_{\mathrm{s}}\right)-j^{\mathrm{Li}}=0$ $-\sigma^{\mathrm{eff}}\frac{\partial}{\partial x}\phi_{\mathrm{s}}\Big\vert_{x=0}=-\sigma^{\mathrm{eff}}\frac{\partial}{\partial x}\phi_{\mathrm{s}}\Big\vert_{x=L}=\frac{I}{A}$ $\frac{\partial}{\partial x}\phi_{\mathrm{s}}\Big\vert_{x=L_-}=\frac{\partial}{\partial x}\phi_{\mathrm{s}}\Big\vert_{x=L_-+L_{\mathrm{sep}}}=0$		$\frac{\partial}{\partial x}\left(\sigma^{\mathrm{eff}}\frac{\partial}{\partial x}\phi_{\mathrm{s}}\right)-j^{\mathrm{Li}}=0$ $-\sigma^{\mathrm{eff}}\frac{\partial}{\partial x}\phi_{\mathrm{s}}\Big\vert_{x=0}=-\sigma^{\mathrm{eff}}\frac{\partial}{\partial x}\phi_{\mathrm{s}}\Big\vert_{x=L}=\frac{I}{A}$ $\frac{\partial}{\partial x}\phi_{\mathrm{s}}\Big\vert_{x=L_-}=\frac{\partial}{\partial x}\phi_{\mathrm{s}}\Big\vert_{x=L_-+L_{\mathrm{sep}}}=0$	(3)
Ohm's law in electrolyte	$\frac{\partial}{\partial x}\left(\kappa^{\mathrm{eff}}\frac{\partial}{\partial x}\phi_{\mathrm{e}}\right)+\frac{\partial}{\partial x}\left(\kappa_{\mathrm{D}}^{\mathrm{eff}}\frac{\partial}{\partial x}\ln c_{\mathrm{e}}\right)+j^{\mathrm{Li}}=0$ $\frac{\partial}{\partial x}\phi_{\mathrm{e}}\Big\vert_{x=0}=\frac{\partial}{\partial x}\phi_{\mathrm{e}}\Big\vert_{x=L}=0$	Simplification with assumption: Ce has no influence on reaction current	$\frac{\partial}{\partial x}\left(\kappa^{\mathrm{eff}}\frac{\partial}{\partial x}\phi_{\mathrm{e}}\right)+j^{\mathrm{Li}}=0$	(4)
Electrochemical kinetics	$j^{\mathrm{Li}}=a_{\mathrm{s}}i_0\left\{\exp\left[\frac{\alpha_{\mathrm{a}}F}{RT}\eta\right]-\exp\left[-\frac{\alpha_{\mathrm{c}}F}{RT}\eta\right]\right\}$ $\eta=\phi_{\mathrm{s}}-\phi_{\mathrm{e}}-U_{eq}$	Linearization	$\frac{\partial}{\partial x}\left(\frac{\partial}{\partial x}\phi_{se}\right)=j^{Li}\left(\frac{1}{\sigma^{eff}}+\frac{1}{k^{eff}}\right)$ $j^{Li}=\frac{a_{\mathrm{s}}i_0F}{RT}\left(\phi_{se}-U\right)$	(5)

Table 2 Simplified governing equations of the ion concentration of solid phase

	ROM equations	
$c_{s,surf}$	$\frac{\left(c_{s,surf}-c_{s,\beta\alpha}\right)\left(k_2-2k_1\left(r_s-r_0\right)\right)-\left(c_{s,ave}-c_{s,\beta\alpha}\right)\left(2k_3\left(r_s-r_0\right)-k_4\right)}{k_2k_3-k_1k_4}=\frac{-j^{Li}}{a_sF}$	(6)
$c_{s,ave}$ of outer layer	$c_{s,ave0}^{k+1}\frac{4}{3}\pi\left(r_s^3-\left(r_0^{k+1}\right)^3\right)-c_{s,ave0}^{k}\frac{4}{3}\pi\left(r_s^3-\left(r_0^{k}\right)^3\right)$ $+c_{s,ave1}^{k+1}\frac{4}{3}\pi\left(r_0^{k+1}\right)^3-c_{s,ave1}^{k}\frac{4}{3}\pi\left(r_0^{k+1}\right)^3=\frac{-j^{Li}}{a_sF}4\pi r_s^2$	(7)
Interface	$\left(c_{s,\beta\alpha}-c_{s,\alpha\beta}\right)\frac{\mathrm{d}r_0}{\mathrm{d}t}=-D_{s,\beta}\frac{\left(c_{s,surf}-c_{s,\beta\alpha}\right)k_2-\left(c_{s,ave}-c_{s,\beta\alpha}\right)k_4}{k_2k_3-k_1k_4}$ $+\frac{D_s}{r_0}\left(35\left(c_{s,surf}-c_{s,ave}\right)-8q_{ave}r_0\right)$	(8)
$c_{s,ave}$ of inner layer	$\frac{d}{dt}c_{s,ave}-3\frac{D_s}{r_0^2}\left(35\left(c_{s,surf}-c_{s,ave}\right)-8q_{ave}r_0\right)=0$	(9)
q_{ave} of inner layer	$\frac{d}{dt}q_{ave}+\frac{1}{2}\frac{D_s}{r_0^3}\left(60q_{ave}r_0-45\right)\left(35\left(c_{s,surf}-c_{s,ave}\right)-8q_{ave}r_0\right)=0$	(10)
Notes	$k_1=\frac{3}{4}\left(\frac{r_s^4-r_0^4}{r_s^3-r_0^3}\right)-r_0,\ k_2=\frac{3}{5}\left(\frac{r_s^5-r_0^5}{r_s^3-r_0^3}\right)-\frac{3}{2}r_0\left(\frac{r_s^4-r_0^4}{r_s^3-r_0^3}\right),$ $k_3=r_s-r_0,\ k_4=\left(r_s-r_0\right)^2$	

2.2.2 ROM with EKF

Since the ROM includes nonlinear functions, EKF is applied to treat the nonlinearity and suppress normal distributed disturbance and measurement noise at the same time. The applied current and SOC are regarded as the input and output, respectively, where the average volume ion

concentration of anode ($c_{s,ave}$) is regarded as a state and the terminal voltage (V_t) is the measuring output. The principles of the EKF is summarized in Table 3.

Table 3 Principles of EKF

Prediction (Time update)	State prediction: $\hat{x}_k^- = f\left(\hat{x}_{k-1}, u_{k-1}\right)$ Error covariance prediction: $P_k^- = A_k P_{k-1} A_k^T + W_k Q_{k-1} W_k^T$	(11)
Correction (Measurement update)	Kalman gain: $K_k = P_k^- H_k^T \left(H_k P_k^- H_k^T + V_k P_{k-1} V_k^T\right)^{-1}$ State correction: $\hat{x}_k = \hat{x}_k^- + K_k\left(z_k - h\left(\hat{x}_k^-\right)\right)$ Error covariance correction: $P_k = \left(1 - K_k H_k\right) P_k^-$	(12)
Note	$A = \left.\frac{\partial f}{\partial x}\right\|_{x_{k-1}}, W = \left.\frac{\partial f}{\partial w}\right\|_{w_{k-1}}$ $H = \left.\frac{\partial h}{\partial x}\right\|_{x_k}, V = \left.\frac{\partial h}{\partial w}\right\|_{w_k}$	(13)

When a current profile is applied to the system, the terminal voltage is fed back to the model to correct the voltage output of the ROM, where the Kalman gain of the EKF is updated and optimized to suppress the noise of the measurement. SOC is calculated using the average ion concentration of anode by Eq. (17). The process is carried out recursively and repetitively. The formulations of the EKF using ROM is shown in Table 4.

As the voltage error between the measurement of a battery and the ROM becomes small, EKF updating fails and leads to a high error of SOC estimation even though the covariance matrices, *Q* and *R*, have been optimized, which is inevitable regardless of any single control technique. One of the solutions is to measure the SOC using the classic Coulomb counting method

until the voltage difference is large enough that EKF can remove the errors efficiently. A flowchart of the hybridized solution of ROM with EKF and Coulomb counting is depicted in Fig. 8, where the voltage difference is defined as a switching factor (τ) that controls which method should be actively used at each time step. When the error of terminal voltage between the measured and estimated state is less than τ, the SOC estimation is performed by Coulomb counting mode. Otherwise, the EKF is on for the duration of the estimation.

Table 4 Formulations of EKF using ROM

State and measurement	$x = \left[\overline{c_{s,ave}^{-}}\right]$ $y = \left[V_t\right]$	(14)
System	$\overline{c_{s,ave}^{-}}^{k} = \overline{c_{s,ave}^{-}}^{k-1} - \frac{3 j^{L1} I}{R_s a_s F A L^{-}}$ $V_t = U^{+}\left(\bar{y}\right) - U^{-}\left(\bar{x}\right) - \eta$	(15)
Jacobians	$A = I$ $H = \frac{\partial V_t}{\partial \overline{c_{s,ave}^{-}}} = \frac{\partial U_{OCV}^{+}}{\partial \bar{y}} \frac{\partial \bar{y}}{\partial \overline{c_{s,ave}^{+}}} \frac{\partial \overline{c_{s,ave}^{+}}}{\partial \overline{c_{s,ave}^{-}}} - \frac{\partial U_{OCV}^{-}}{\partial \bar{x}} \frac{\partial x}{\partial \overline{c_{s,ave}^{-}}}$	(16)
SOC estimation	$SoC = \left[\frac{1}{L_{-}} \int_0^{L_{-}} \frac{(c_{\text{s,ave-}} - c_{\text{s,max}} \cdot x_0)}{c_{\text{s,max}} \cdot (x_{100} - x_0)} \cdot dx\right] \cdot 100\%$	(17)

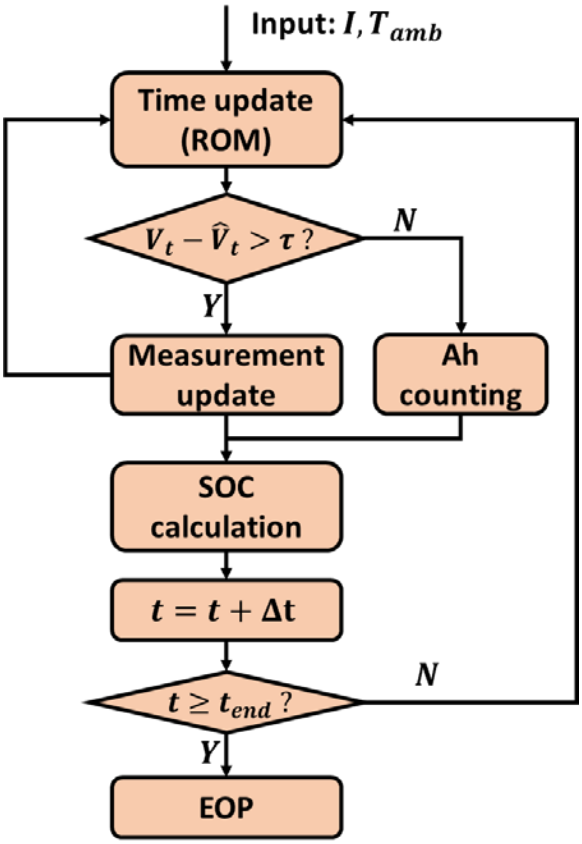

Fig. 8 Flow chart of the hybrid algorithm of SOC estimation

2.3 Experimental and simulated evidence of existence of path dependence

Experiments and simulations of ROM with the hybrid algorithm are preformed to investigate the effects of path dependence of LFP cathode, where the juxtaposition of phases depends on the battery usage history. The theoretical principles have been introduced in section 1.3.2. The experiments are conducted in two different paths as shown in Fig. 9. In path 1 (the blue solid line), the cell is: ① discharged from 100% SOC to 50% SOC by 0.1C-rate (2A) current; ② sufficiently rested for about 2 hours; ③ discharged further to 0% SOC by 4C-rate (80A) current. In path 2 (the red solid line), the cell is: ① charged from 0% to 50% SOC by 0.1C-rate current; ② sufficiently rested for about 2 hours; ③ discharged further to 0% SOC by 4C-rate current.

Final releasable capacity of both experiments and simulations conducted in different paths are different. When the cell is discharged from a fully charged state as shown in path 1, a core of α phase covered by a shell of β phase is shrunk due to the continuous intercalation of lithium ions into the core. The diffusion distance through β phase for lithium ions is increased. On the other way, the cell is charged from a fully discharged state to 50% SOC, with a core of β phase covered by a shell of α phase. When it is discharged further, the old shell of α phase will be covered by the newly generated β phase. In this case, the diffusion can only be through the new shell of β phase. The diffusion distance is relatively shorter than that in path 1, which causes a reduction of the final capacity.

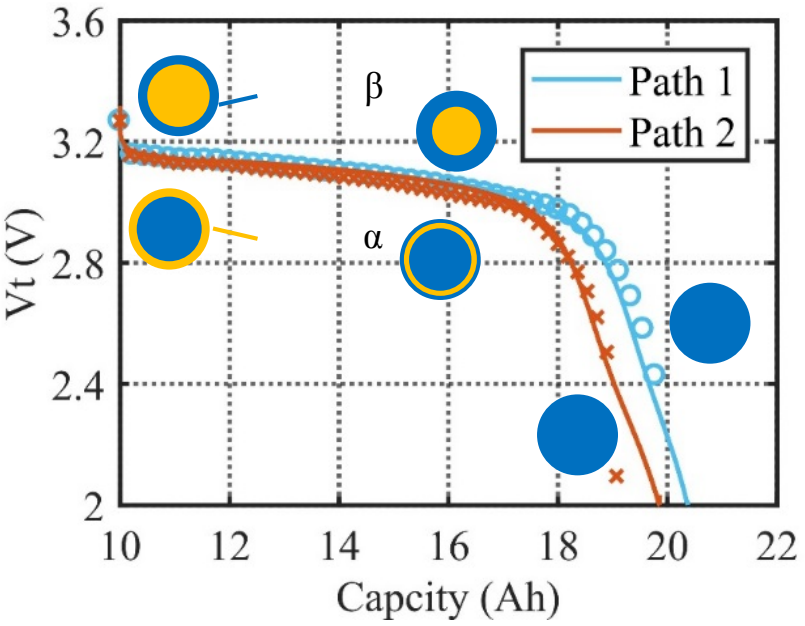

Fig. 9 Experimental and simulated evidence of existence of path dependence

2.4 Validation of beginning-of-life (BoL)

Cells used for experiments are the large-format pouch-type $LiFePO_4$/graphite cells whose specifications are shown in Table 5. The LiBs are tested in a thermal chamber with three K-type thermocouples adhesive to the cell surface to measure temperatures. A programmable power supply and an electric-load are connected in parallel to supply the programmed charge/discharge current profiles. Impedance spectra are measured by electrochemical impedance spectroscopy (EIS) equipment, GAMRY, and the parameters are found by fitting the ECM.

Table 5 Specifications of testing cells

Material	Cathode	LFP
	Anode	Graphite
	Electrolyte	Confidential
End-of-charge (EoC) voltage		3.6V
End-of-discharge (EoD) voltage		2.0V
Nominal capacity		20Ah

The experiments of fresh cells include measurement of the OCV, application of the charge/discharge profiles in the single cycles and multiple cycles. The OCV is measured at the ambient temperature of 25°C using a very small current of 0.05C-rate (1A) in order to allow the terminal voltage and OCV to be equal in the maximum likelihood. The charge/discharge protocols in the single and multiple cycles are as follows: 1) Pre-tests: 5 initial cycles at constant current (CC) of 1C-rate (20A) with 30 minutes' rest between each consecutive charge/discharge cycle; 2) Single-cycle tests: ① Charge the cell using CC until EoC voltage (3.6V); ② Rest for 30 minutes;

③ Discharge the cell using CC until EoD voltage (2V). The CC applied at charging and discharging varies among 1C-rate, 2C-rate and 4C-rate at different ambient temperatures (25/40/55°C, respectively). 3) Multiple-cycle tests: Discharge the cell to 2V and then charge it to 3.6V continuously without resting using CC at 1/2/4C-rate; 4) Post-tests: EIS and capacity measurements.

In order to verify the accuracy of the ROM with EKF, the experimental data and their corresponding simulation results with different discharge/charge currents applied are compared at different operating temperatures. The comparison of the discharge profile between the pre-developed ROM and the ROM with EKF is depicted in Fig. 10. The constant discharging current of 1C-rate with resting is applied to a fresh LFP/graphite cell at the operating temperature of 25°C. The markers, the pink solid line and the blue solid line represent the results of experiments, ROM and ROM with EKF, respectively. For the CC discharging, the terminal voltage of both the ROM and the ROM with EKF shows a good match with the experimental data. However, the terminal voltage estimated using ROM could not reach the end-of-discharge (EoD) cutoff voltage. Furthermore, the prediction of voltage recovery during resting is underestimated by the ROM, but in an excellent match with the ROM with EKF. Therefore, the incorporation of the EKF into the developed ROM achieves a better accuracy of the estimation of the terminal voltage.

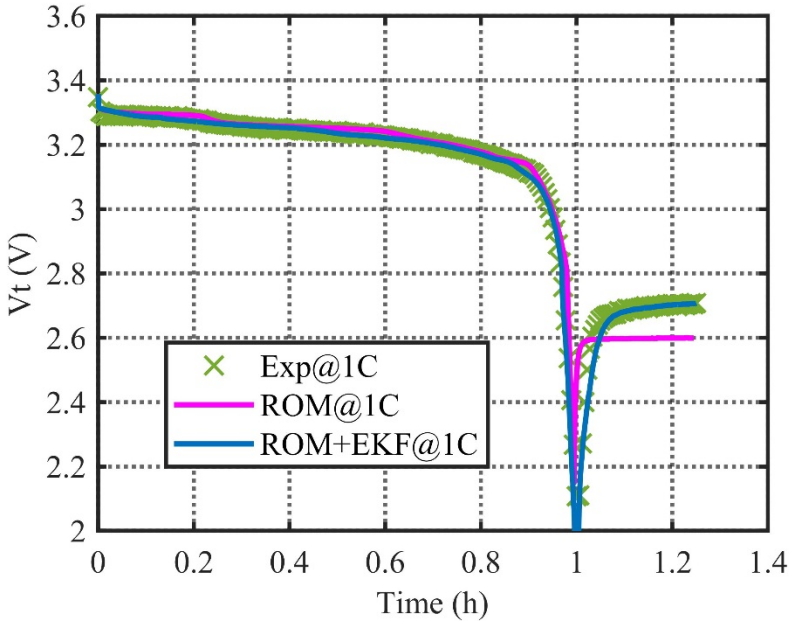

Fig. 10 Comparison of discharge behaviors between experimental data and simulation results of ROM with/without EKF at 25°C

The comparisons of terminal voltage and SOC between experimental data and simulation results of the ROM with EKF with different discharge and charge currents (1/2/4C-rate) applied at 25°C are plotted in Fig. 11 and Fig. 12, respectively. Since constant currents are applied to the cells, the slope of the SOC should be a constant. The markers and the solid lines represent the experiments and simulations, respectively. The responses of terminal voltages and SOCs have a good match with experiments for different discharge and charge profiles at 25°C. The error between the experimental measurements and the estimated results obtained from the ROM with EKF are summarized and depicted in Fig. 13. The estimated errors of terminal voltage and SOC are within 2% and 4%, respectively.

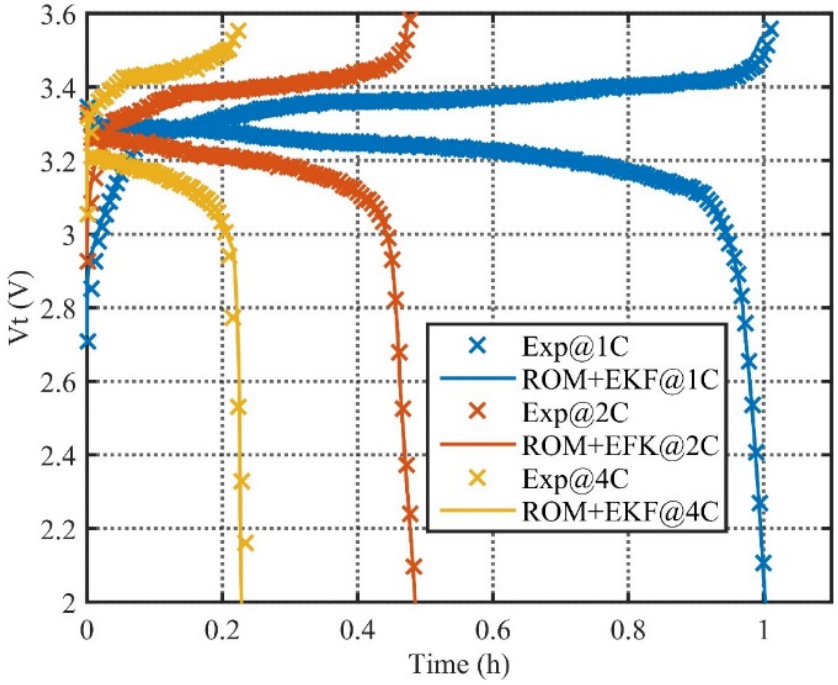

Fig. 11 Comparison of terminal voltage at various charging/discharging C-rates between experiments and simulations at 25°C

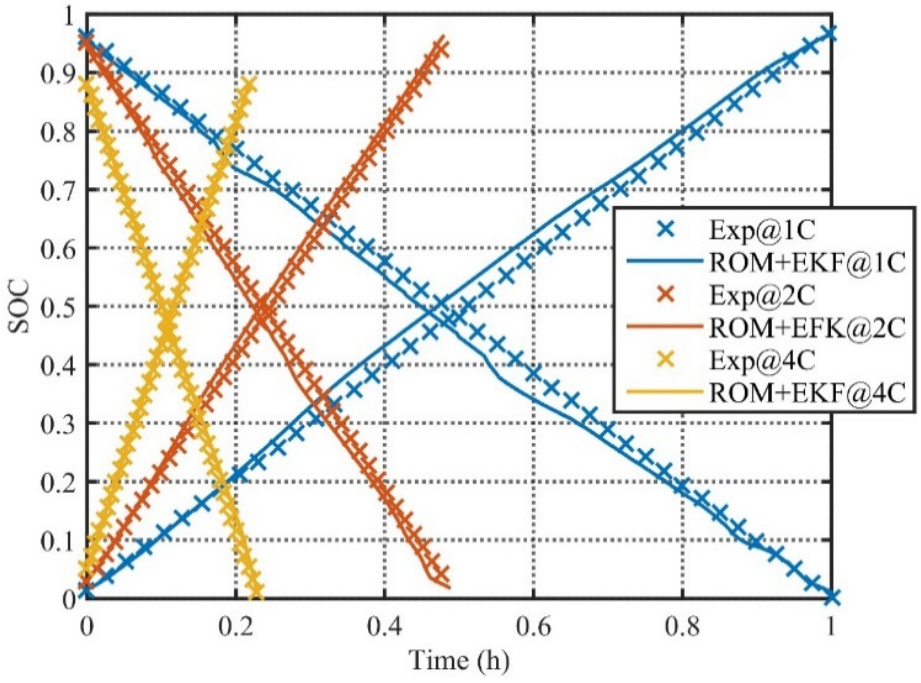

Fig. 12 Comparison of SOC at various charging/discharging C-rates between experiments and simulations at 25°C

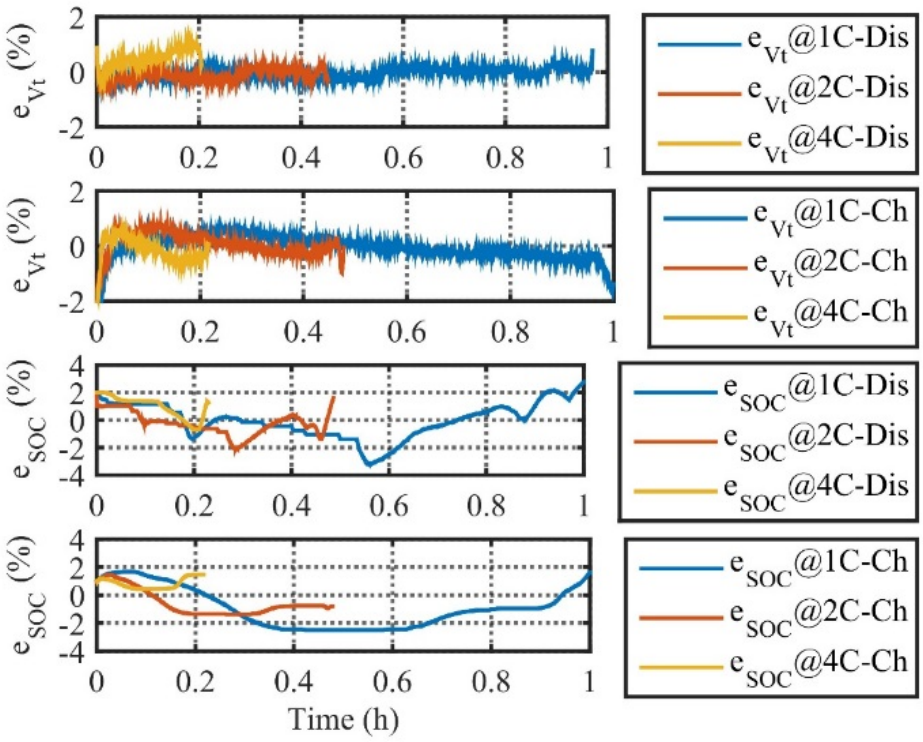

Fig. 13 Estimation error of terminal voltage and SOC at 25°C. Dis and Ch are for discharge and charge, respectively.

Some parameters of the ROM are highly sensitive to the temperatures, such as the diffusion coefficients of electrode and electrolyte phase. According to the analysis of parameter sensitivity, the diffusion coefficient of solid phase has influence on the releasable capacity, while that of the electrolyte phase has influence on the overpotential. Thus, dependency of the diffusion coefficient on temperature are reflected using the Arrhenius equation which is shown in Eq.(18). The curve fitting of solid diffusion coefficient as a function of temperature is presented in Fig. 14.

$$D_s = D_{s0} \cdot \exp\left[\frac{E_a}{R}\left(\frac{1}{T_0} - \frac{1}{T}\right)\right] \tag{18}$$

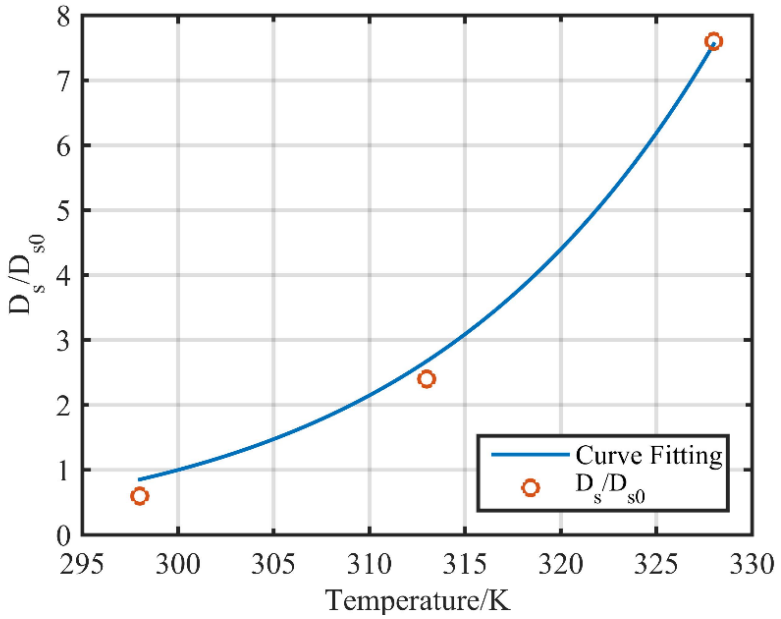

Fig. 14 Curve fitting of diffusion coefficient as a function of temperature

Different discharging currents (1/2/4C) are applied to the cells at 40°C and 55°C. The comparison results of the electrochemical behaviors, terminal voltage and SOC, are plotted in Fig. 15. The upper two subplots are the comparisons of terminal voltage and SOC at 40°C from left to right, while the lower two subplots are those at 55°C. Both terminal voltage and SOC estimations are in a good match.

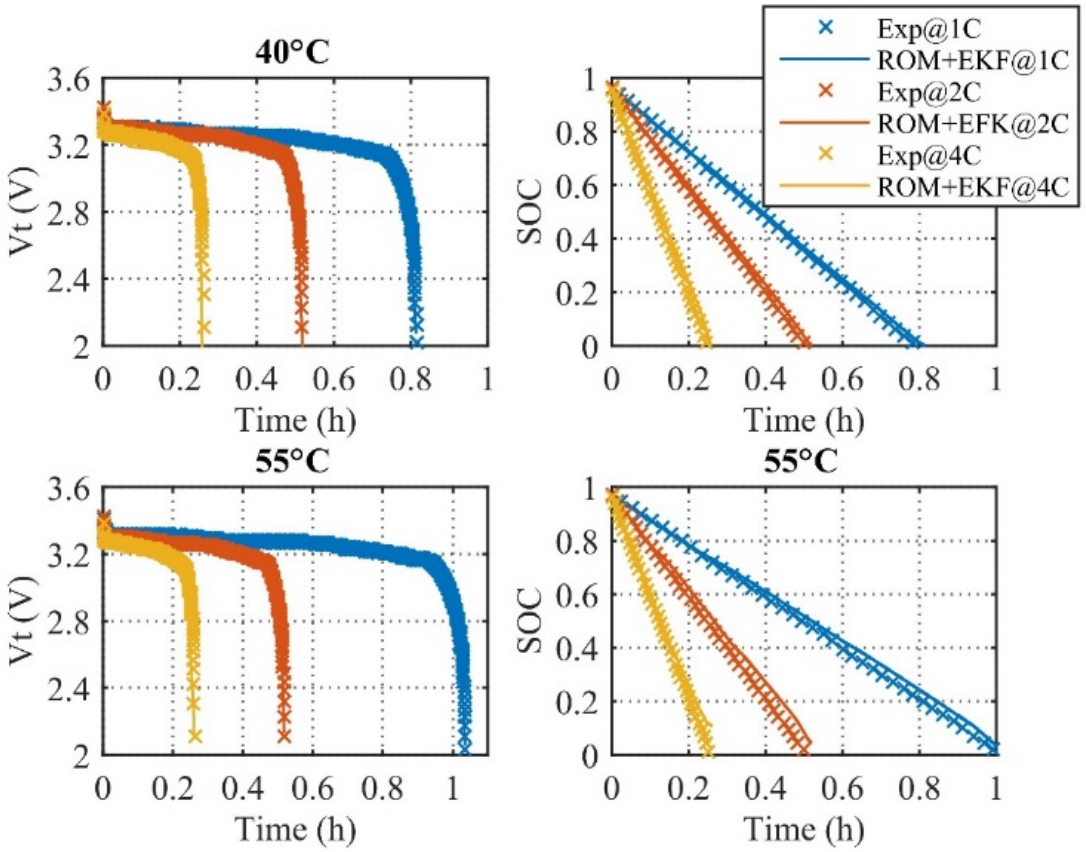

Fig. 15 Comparison of discharge behaviors, terminal voltage and SOC, at 40°C and 55°C

Besides the validation of the static response of the ROM with EKF, such as constant discharging and constant charging, the transient response of the model is validated against multiple cycle tests. The top subplot in Fig. 16 depicts the load current profiles to the cells. The positive and negative sign of the current is defined as the discharging and charging current, respectively. The middle subplot is the response of terminal voltage at multiple cycles at 25°C. The bottom subplot is then the SOC comparison between experiments and simulations at 25°C. The maker, 'X', and solid line represent the experimental measurements and simulation results, respectively. Furthermore, the simulation results show a great match with experimental measurements.

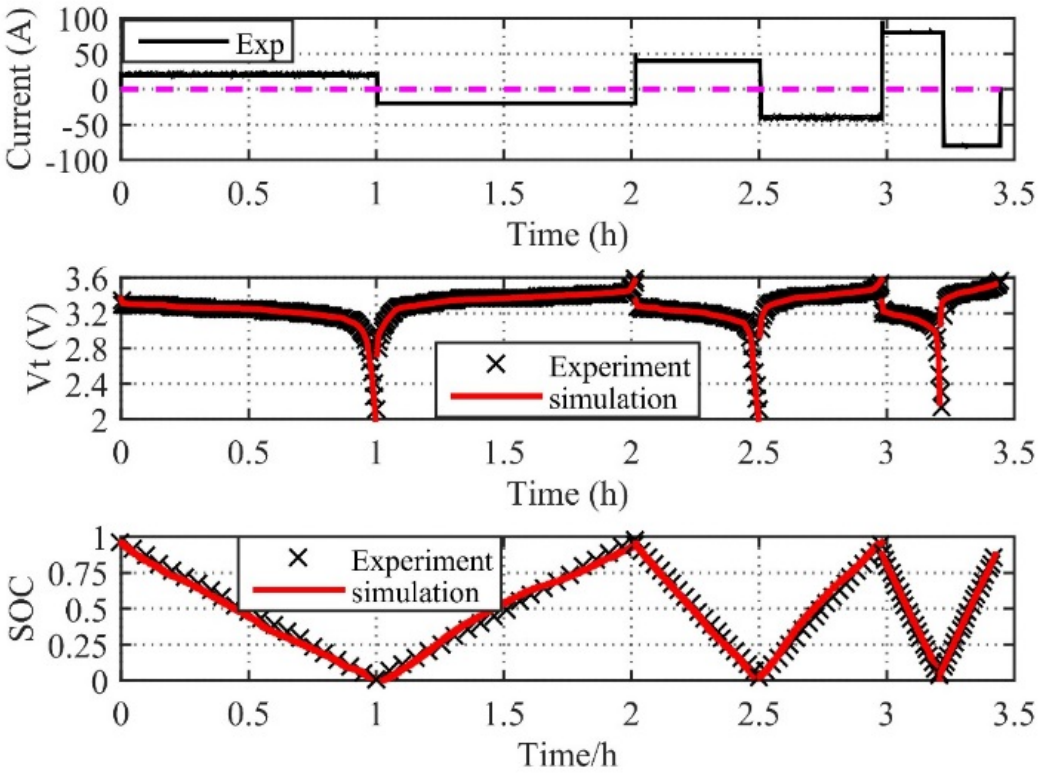

Fig. 16 Dynamic response of multiple cycles at 25°C

2.5 Summary

An electrochemical thermal ROM incorporated with EKF has been developed to optimize the SOC estimation method. Polynomial approach, state space approach and linearization are applied to reduce the order of partial differential equations (PDEs) and nonlinear equations, so that the efficiency of the model has been improved. The usage of EKF allows for suppression of measurement errors and better prediction of average ion concentration that is used to estimate the SOC. However, EKF itself cannot predict the state of LFP cells well enough due to the existence of voltage plateau which is caused by the special characteristics of two-phase transition for a wide range of SOC. Therefore, Coulomb counting method is used to compensate the ineffectiveness of

the EKF, which leads to a hybridized method. This method has been tested under various testing conditions including different current rates and different temperatures in both single and multiple cycles. The results show that the terminal voltage error never exceeds 2% and the SOC error can be kept within 5%.

Chapter 3. Physics-based degradation model considering side reaction at high temperatures

3.1 Literature review

The degradation of LiBs corresponding to calendar life [24,25] and cycle life [26–29] is as the results of exposing to the ambient environment and cycling usage, respectively. The capacity and power fade are not caused by a single reason, but from large varieties. The inter-dependency of various degradation causes makes the comprehension of degradation mechanism more difficult. Schematic diagram of potential degradation mechanism taking place at composite electrodes, separator and current collectors is depicted in Fig. 17.

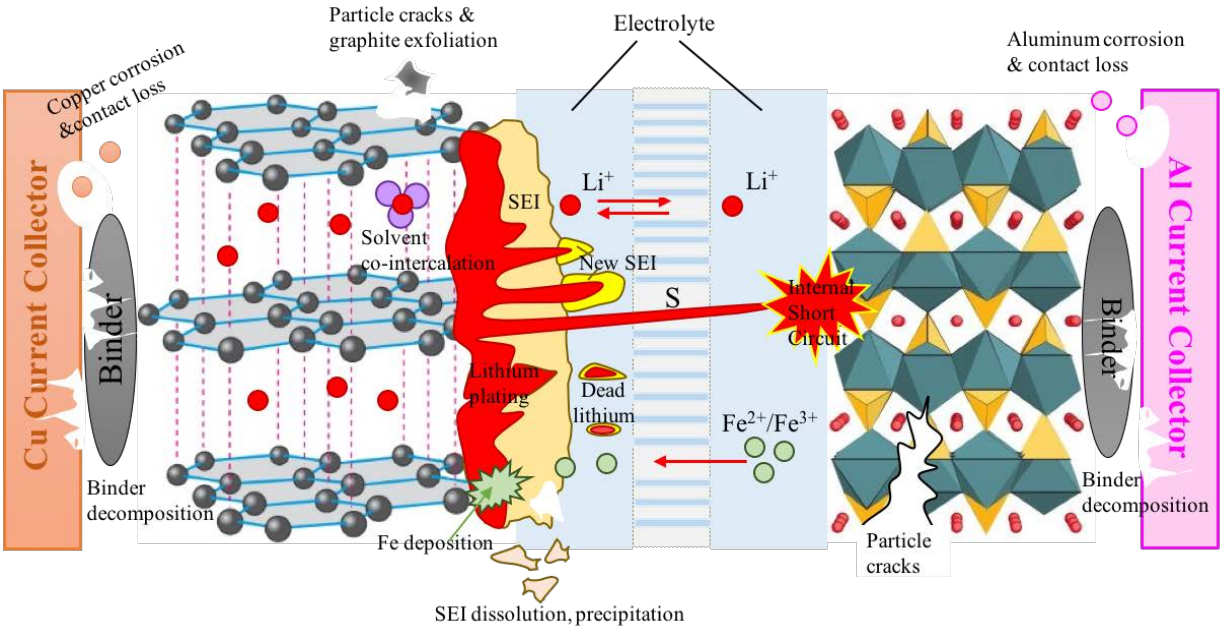

Fig. 17 Schematic diagram of degradation mechanism in LFP/graphite cells.

Degradation phenomena occurring at positive and negative electrode are significantly different. Researchers have identified the side reaction taking place at the interface between electrode and electrolyte at the anode as the predominant cause of degradation for LiBs [30,31,40,32–39]. The main reaction is the intercalation/de-intercalation of lithium ions to/from the electrode solid matrix during cycling. The side reaction takes place between the lithium ions and the electrolyte solvents, which leads to the formation of the unsolvable byproducts that are the main components of the solid electrolyte interphase (SEI) layer. The side reaction is described in Eq. (19) and (20).

$$2Li^+ + 2e^- + EC \rightarrow CH_2 = CH_2 \uparrow + Li_2CO_3 \downarrow \quad (19)$$

$$2Li^+ + 2e^- + 2EC \rightarrow CH_2 = CH_2 \uparrow + (CH_2OCO_2Li)_2 \downarrow \quad (20)$$

Other byproducts of the side reaction, such as LiOH, Li_2O, and ROLi etc., are neglected as minor components. The major compositions of the SEI after the reduction of ethylene carbonate (EC) based electrolyte are lithium carbonate (Li_2CO_3) and lithium ethylene dicarbonate ($(CH_2OCO_2Li)_2$). The SEI is prone to form at initial cycles, especially in charging protocol, which is used to protect the electrode from possible corrosion and prevent electrolyte from being decomposed. The SEI is permeable to lithium ions and electrolyte solvents, but impermeable to electrons, which can be treated as a natural barrier of the main reaction on the covered surface of anode. Therefore, the lithium ions and electrolyte solvents take side reaction after diffusing through the formed SEI. The schematic diagram of SEI formation at anode is shown in Fig. 18. The new SEI is formed at the interface between the pre-formed SEI and electrode particles. In addition, the SEI grows over time, clogs pores and isolates graphite particles that cause a decrease of the accessible area for lithium ions to participate in reduction reactions, which provokes loss of active anode material. When the graphite particle is fully covered by the SEI, the isolation of electrons makes it impossible to participate in the chemical reaction anymore, which is treated as one source of the loss of recyclable lithium ions. The continuous consumption of lithium ions is the other source of ion losses, which could result in capacity fade during prolonged cycles.

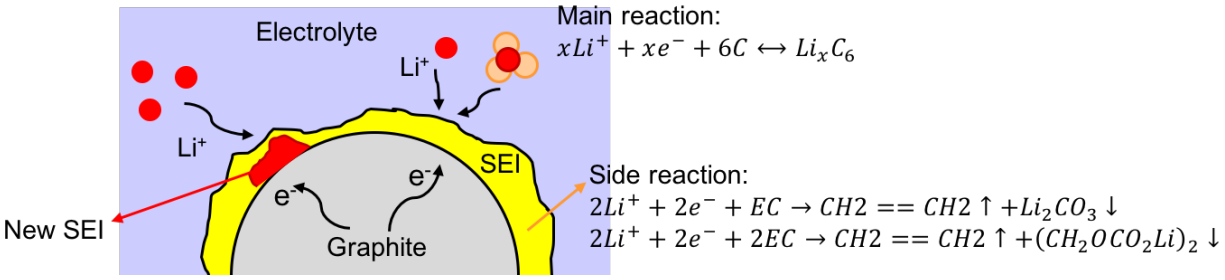

Fig. 18 Schematic diagram of SEI formation at anode

Previous study shows that the byproducts of side reaction are not only accumulated on the surface of graphite particles, but also on the interface between the composite anode and separator, which is defined as the deposit layer (DL) [41]. As the increasing thickness of the SEI and DL, the ionic conductivity decreases, which causes power fade. The continuous electrolyte decomposition and its attribute to side reaction leads to the impedance rise of electrolyte, which induces power fade as well. Thereby, loss of recyclable lithium ions and loss of AM of graphite electrode mainly result in capacity fade of LiBs, while the impedance rise induced from the growth of SEI and DL and electrolyte decomposition are the main causes for power fade.

To degradation effects of LFP cathode, researchers [42–44] have identified iron deposition on the surface of graphite electrode using various characterization techniques, such as transmission electron microscopy (TEM) and Raman spectroscopy. It was also proposed that the iron dissolution from LFP electrode surface was caused by the chemical reaction between acidic species in the electrolyte and Fe^{3+} impurities [45]. In a failure case, the deposited irons on the surface of graphite electrode could grow as dendrites to cause internal short circuit. However, Liu et al. [46] revealed that the iron dissolution from LFP electrode was only a minor effect of degradation compared with those taking place on anode. Therefore, the degradation effects of iron dissolution on cathode are not considered in the development of the physics-based degradation model.

The various causes, impact factors and inter-dependencies of degradation mechanism make it extremely challenging to describe the degradation effects of LiBs mathematically. The models to predict the degradation phenomena can be divided into two groups, empirical/semi-empirical models [27,47–50] and physics-based electrochemical thermal models [51,52]. The models in the first group were developed by fitting the experimental data to obtain the empirical equations or extract degradation parameters to predict the capacity fade or impedance rise for both calendar life

and cycle life. Even though it has the strengths of high accuracy, it is still limited by its high dependence on experimental data and empirical coefficients. In addition, the accuracy cannot be maintained if operating conditions are out of the experimental ranges. Conversely, the physics-based degradation models consider the side reaction whose rate was quantified by the reformulated Butler-Volmer equation based on the concept provided by Newman [53]. Considering the phase change phenomenon of LFP based cells, M. Safari and C. Delacourt [54,55] proposed the FOM incorporating side reaction based on the resistive-reactant perspective. The physical boundary between two phases was replaced by the concentration-dependent diffusion coefficients. P. Gambhire et al. [51] developed a ROM by volume averaging methods with concentration-dependent diffusivities and then incorporated SEI formation by side reaction. No capacity or power fade could be estimated in the model. An integrated ROM with EKF considering degradation effects was developed and validated for both fresh and aged LFP/graphite cells. The capacity and power fade resulting from different degradation mechanism were discussed using the integrated model.

3.2 Experimental analysis

The test matrix of both calendar life and accelerated cycling tests is shown in Table 6. For calendar life tests, the capacity and impedance are measured at the beginning and end of storage, while for accelerated long-term cycling tests, those are measured every 30 or 60 cycles. To guarantee the comparability of the experimental data at different operating conditions, all the measurements of capacity and impedance are conducted at 25°C. Capacity is measured as follows: 1) Charge the cell using CC protocol (CC: 1C-rate) to 3.6V; 2) Rest for 30 minutes; 3) Discharge

the cell with 1C-rate CC to 2V. EIS is measured: 1) Charge the cell to 50% SOC by 1C-rate CC; 2) Rest for 3 hours; 3) Conduct EIS test at the frequency from 10mHz to 1kHz.

Table 6 Test matrix

Calendar life tests				
T(°C)	SOC	Duration		
25 55 -10	10/30/50/70/90%	8months		
Cycling tests				
T (°C)	Cha./Dis. Current	ΔSOC		
		25-95%	5-75%	45-55%
25	4C/4C	1440 cycles 3000 cycles		3500 cycles
40		900 cycles		
55		870 cycles	540 cycles	
EIS test	Frequency range: 10mHz to 1kHz			

3.2.1 Analysis of calendar life tests

The LFP/graphite cells with different initial SOCs (10%, 30%, 50%, 70% and 90%, respectively) are stored at different temperatures (-10°C, 25°C and 55°C, respectively) for about 8 months. To investigate the degradation behaviors, capacity fade and impedance rise are necessary to be discussed.

3.2.1.1 Capacity fade analysis

The percentage of the capacity fade is defined as

$$Q_{fade} = \frac{Q_{ini} - Q_{act}}{Q_{ini}} \times 100\% \quad (21)$$

where Q_{ini} and Q_{act} are the initial and actual capacity measured at the beginning and end of calendar life tests by 1C-rate discharge current, respectively.

The capacity fade of 15 cells at different storage conditions is shown in Fig. 19. The cells stored at high temperature (e.g. 55°C) and high SOC levels (e.g. SOC=90%, 70%) suffer larger capacity fade than those stored at relatively low temperature (e.g. 25°C and -10°C) and low SOC levels (e.g. SOC=30%,10%). The capacity fade is mainly caused by side reaction, whose rate is increased by the elevated temperature. High SOC induces large overpotential, which leads to more capacity decay. In addition, the temperature dependent degradation effects have more influence on the cells stored at high SOC levels. Therefore, the capacity fade is aggravated with the increase of storage temperature and SOC.

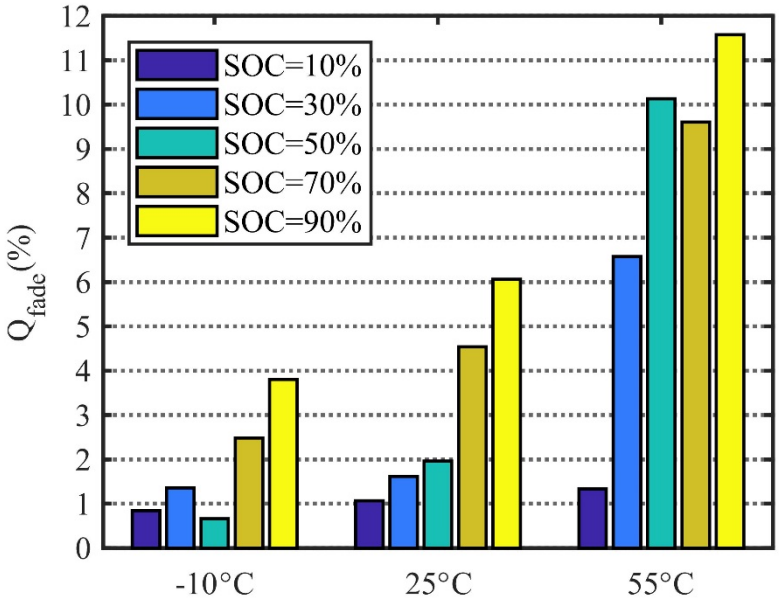

Fig. 19 Capacity fade of the stored cells at different SOC levels and temperatures

3.2.1.2 EIS analysis

ECM is a highly efficient tool that can be used to analyze the characteristics of the impedances measured by EIS. The EIS-ECM developed is similar to those reported in the literatures and its configuration is shown in Fig. 20. In the model, L is used to model the mutual inductance of external wires in high frequency domain (>1kHz). R_0 is the Ohmic resistance caused by electrolyte, deposit layer, separator, current collector and electrode, which equals to the left intercept between impedance spectrum and the x-axis at high frequency (≈1kHz). R_1 and C_1 indicate SEI resistance and capacitance at anode, which dominate the shape of the first semi-circle in high frequency domain from 1kHz to several Hz. R_2 and C_2 indicate charge transfer resistance and double layer capacitance, respectively. They affect the shape of the second semi-circle, which is less obvious in the lower frequency range (several Hz to several mHz). W_a is the Warburg

admittance that represents ion diffusion in the electrolyte and C_{int} is the intercalation capacitance that indicates the process of ion intercalation. Both W_a and C_{int} dominate the impedance in the low frequency region (< several mHz).

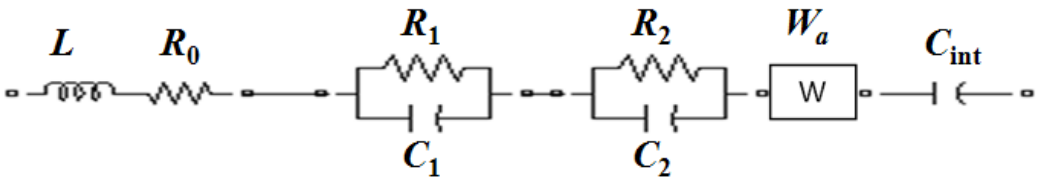

Fig. 20 EIS equivalent circuit model.

The impedance spectra of the cells stored at various initial SOCs at 25°C, 55°C and -10°C, are plotted in Fig. 21, Fig. 22, and Fig. 23, respectively. Dots and solid lines represent the experimental measurements and the fitted curves obtained using the ECM, respectively. After having stored for 8 months, two apparent effects can be observed whatever the storage condition is. (1) The impedance spectra shift rightwards slightly, which implies the increase of Ohmic resistance. (2) The increase of the radius of the first semi-circle denotes the increase of SEI resistance. The impedances including both Ohmic and SEI ones are increased with the increasing storage temperature. The relationship between storage SOC and impedance rise is not obvious regardless of the temperature. Therefore, the characteristics of impedances are more sensitive to storage temperature rather than SOC.

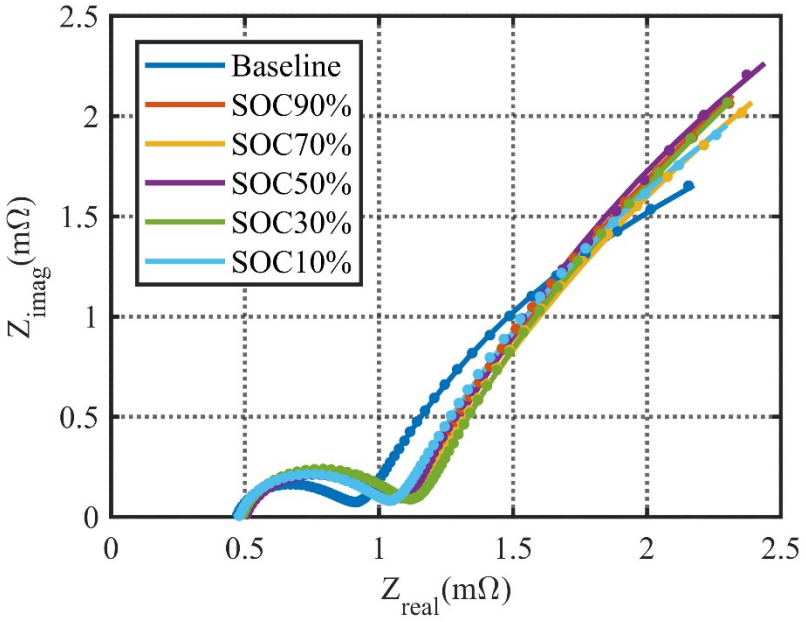

Fig. 21 Impedance spectra of the cells stored at various initial SOCs at 25°C

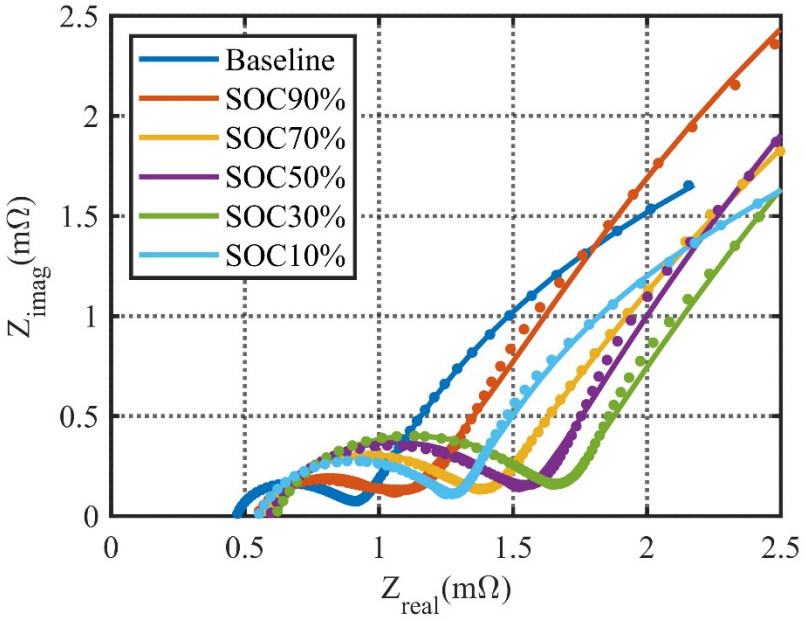

Fig. 22 Impedance spectra of the cells stored at various initial SOCs at 55°C

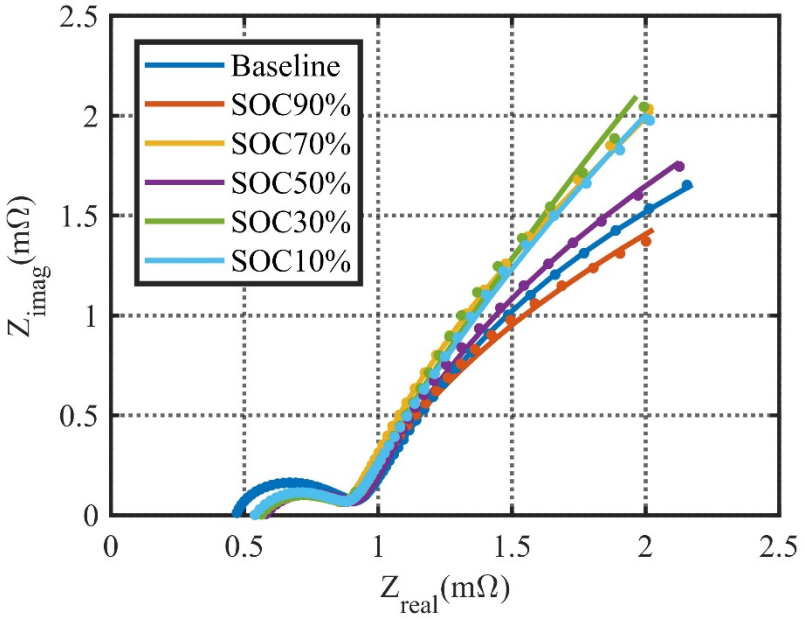

Fig. 23 Impedance spectra of the cells stored at various initial SOCs at -10°C

3.2.2 Analysis of accelerated cycling tests

Undergoing prolonged cycles, CC charging and CC discharging profiles with 4C-rate currents applied are performed to the LiBs. According to the test matrix summarized in Table 6, the effects of operating conditions, including operating temperature from 25°C to 55°C, SOC level and SOC cycling limit around an average of 50% SOC, on degradation are explored. Degradation performances will be discussed from the aspects of capacity fade and impedance rise.

3.2.2.1 Capacity fade analysis

State-of-health (SOH) is described by the ration of releasable capacity over nominal capacity, which is used to evaluate the available capacity or power of the LiBs. The capacity

retention of the cells cycled at various operating conditions, which is represented by SOH_Q, is plotted in Fig. 24. The capacity fade profiles of two cells cycled at the same condition (ΔSOC: 25-95%, T: 25°C), which are depicted by markers, "X", show a great repeatability of experiments. At the same temperature, the capacity decays faster at larger SOC cycling limit, which induces more lithium ions to take part in the side reaction. At the same number of cycles, the capacity fade of the cell cycled at a high SOC (25-95%) is more than that cycled at the relative low SOC. In summary, degradation is accelerated by the elevated temperature, high SOC and large SOC cycling limit. Compared the three affecting factors with each other, the temperature is of the uttermost influence on degradation.

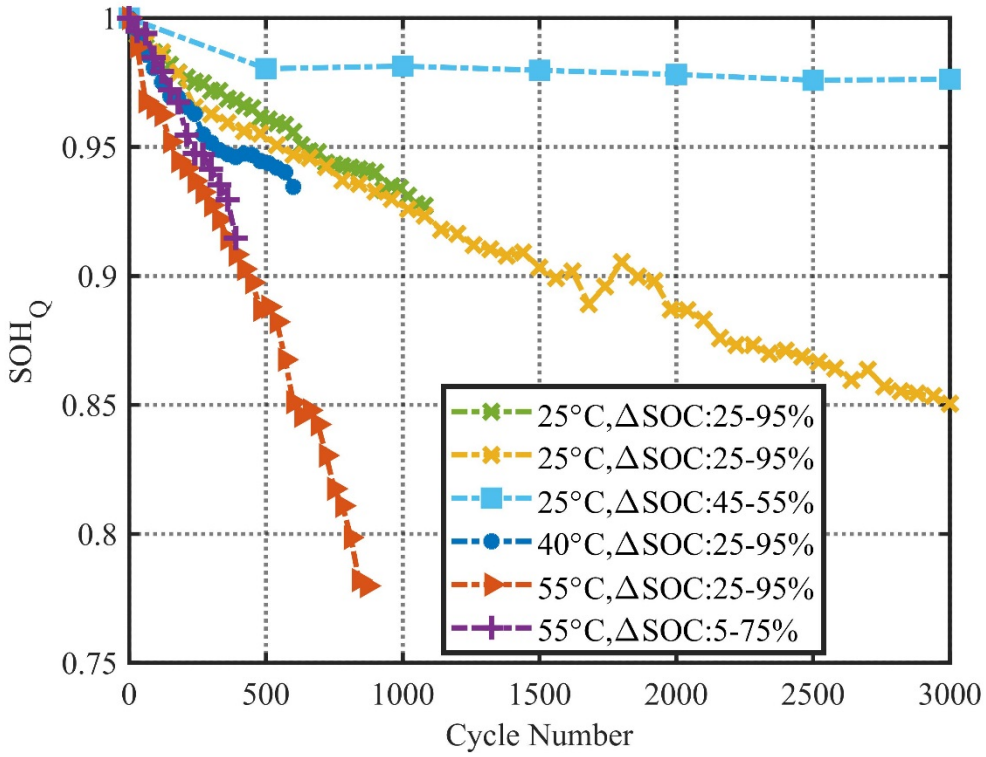

Fig. 24 Capacity fade of cycled cells at different operating conditions

3.2.2.2 EIS analysis

The impedance rise leading to power fade is discussed at various operating conditions as a function of cycle number. With the increase of cycle number, electrolyte solvents, as the reactants of side reaction, are continuously consumed. The ionic conductivity of electrolyte is decreased so that the Ohmic resistance including electrolyte resistance is increased, which is represented by the rightward shift of the impedance spectrum. Moreover, the byproducts produced by side reaction, which are the main compounds of SEI, are accumulated. The increase of the radius of the first semi-circle represents the increase of SEI resistance.

The impedance spectra of the cells cycled at 25°C from 25% SOC to 95% SOC up to 3000 cycles are plotted in Fig. 25, while those from 45% SOC to 55% SOC are plotted in Fig. 26. The effects of SOC cycling limit are explored. Under prolonged cycling, the amount of lithium ions that take part in side reaction is increased as the enlargement of SOC cycling limit. The impedance rise resulting from both electrolyte consumption and SEI growth are enhanced by a large SOC cycling limit.

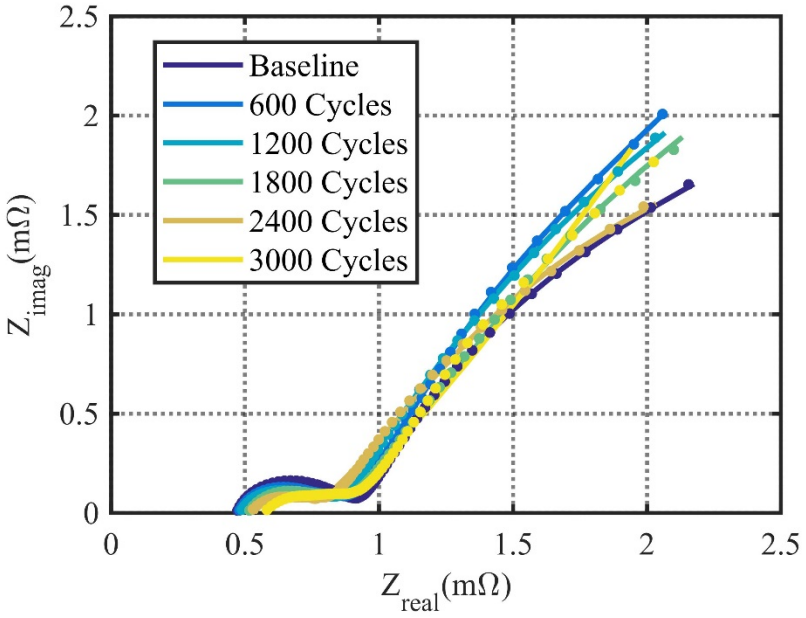

Fig. 25 Impedance spectra of the cell cycled from 25% to 95% SOC at 25°C

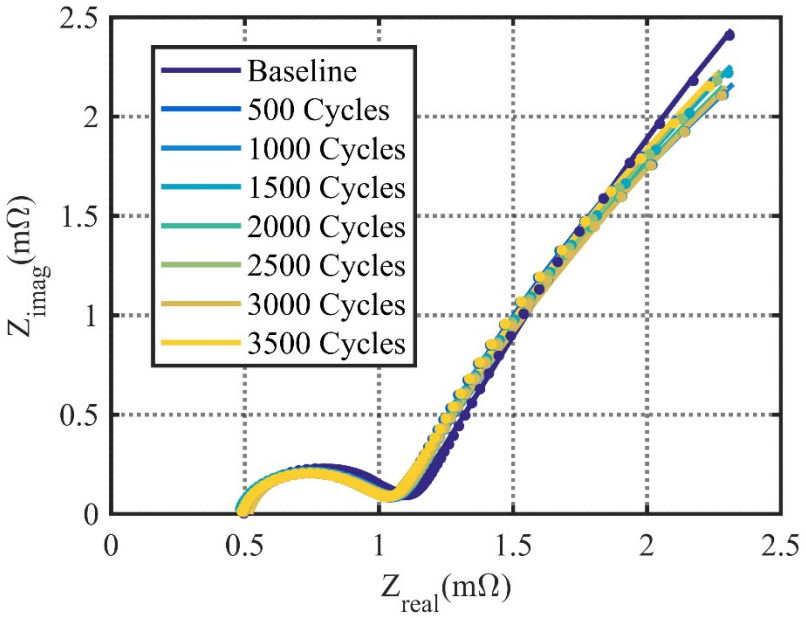

Fig. 26 Impedance spectra of the cell cycled from 45% to 55% SOC at 25°C

In addition, the effects of temperature on the degradation corresponding to the aspect of impedances are discussed in Fig. 25, Fig. 27 and Fig. 28. Fig. 27 and Fig. 28 show the impedance spectra of the cells cycled at the same SOC cycling limit at 40°C and 55°C, respectively. With the increase of operating temperature, the side reaction rate is increased, which induces more degradation. Not only the rightward shift of the spectra, but also the increasing radius of the semi-circle, can be observed more obviously at the elevated temperatures.

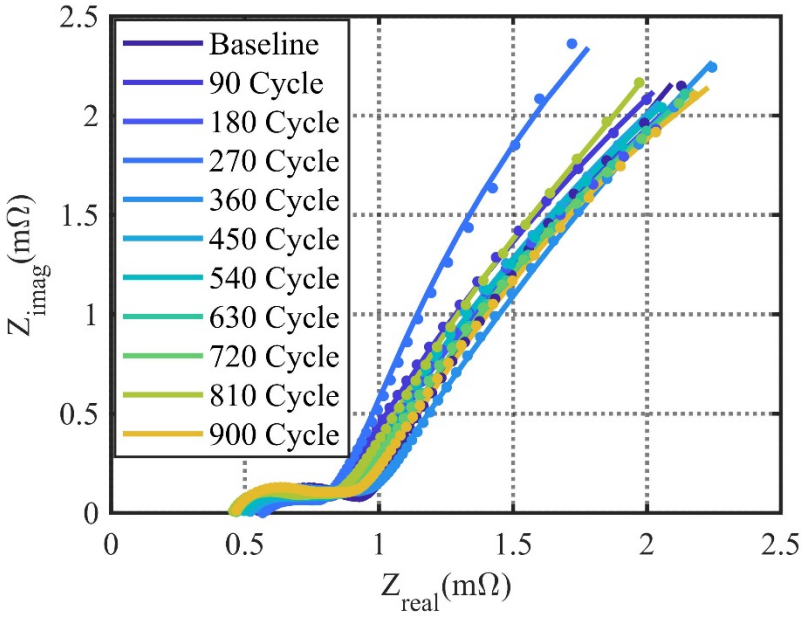

Fig. 27 Impedance spectra of the cell cycled from 25% to 95% SOC at 40°C

Fig. 29 shows the impedance spectra of the cells cycled from 5% SOC to 75% SOC at 55°C, which is compared with those in Fig. 28, the effects of SOC level are discussed. Under the same SOC cycling limits and temperature, the high SOC triggers the side reaction due to the large overpotential. Besides the impedance spectrum at 540th cycle, the shifting distance and semi-circle radius at corresponding cycle number are larger when the cells are cycled at high SOC levels.

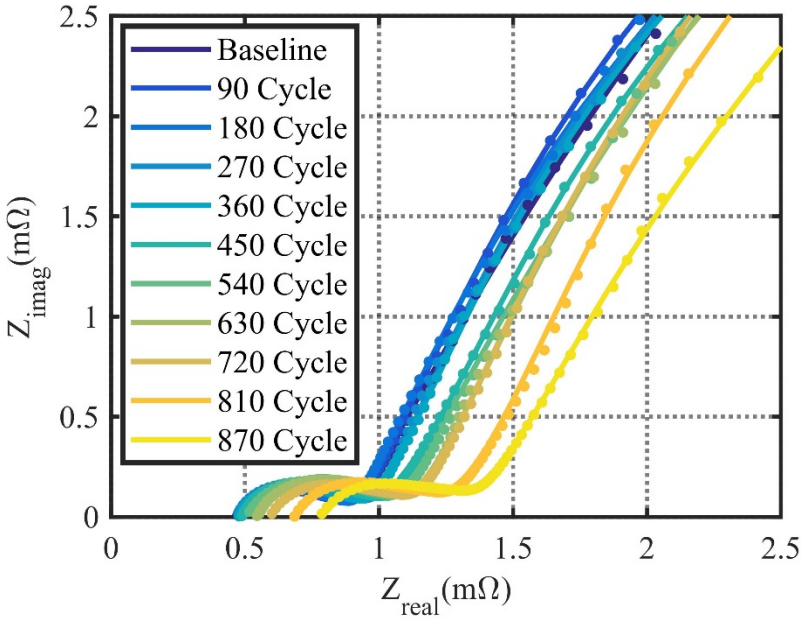

Fig. 28 Impedance spectra of the cell cycled from 25% to 95% SOC at 55°C

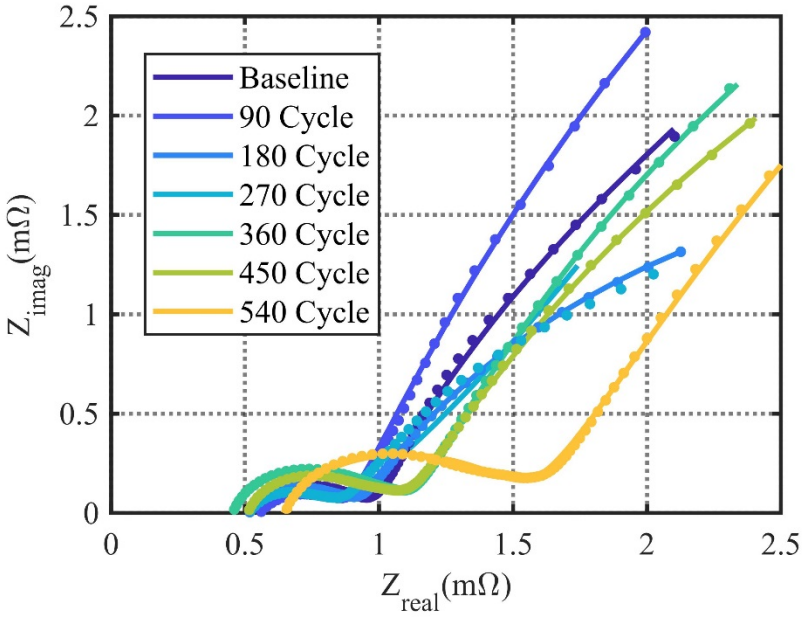

Fig. 29 Impedance spectra of the cell cycled from 5% to 75% SOC at 55°C

3.3 Mathematical principles

3.3.1 Modeling of main reaction and side reaction

In order to develop a physics-based degradation model, several assumptions have been made:

1. The byproducts of side reaction are only the mixture of Li_2CO_3 and $(CH_2OCO_2Li)_2$ based on Eq. (19) and Eq. (20).
2. The reduction reaction rate of side reaction is much higher than the oxidation reaction rate, which implies that the side reaction is an irreversible process.
3. Degradation effects on cathode, such as iron dissolution, are neglected.
4. No overcharge nor undercharge process is considered.
5. No mechanical failure, such as graphite exfoliation, electrode volume change and particle cracks, is considered.

In the former developed ROM with EKF, the BV equation of Eq.(5) only describes the main reaction. Considering side reaction, the reformulated BV equation describes the total reaction rate which is the sum of the reaction rate of the main and side reaction. Based on the assumptions of irreversible process, the side reaction rate only considers the reduction reaction. The corresponding equations about degradation are summarized in Table 7. Compared to the overpotential of Eq. (5), the potential drop caused by SEI formation has been added in the model.

Table 7 Equations for physics-based degradation model

	Main reaction – intercalation/de-intercalation	Side reaction
reaction rate	$j^{\mathrm{Li}} = a_{\mathrm{s}} i_0 \left\{ \exp\left[\frac{\alpha_{\mathrm{a}} F}{RT} \eta \right] - \exp\left[-\frac{\alpha_{\mathrm{c}} F}{RT} \eta \right] \right\}$ $\xrightarrow{linearization}$ $j^{Li} = a_s i_0 \frac{(\alpha_a + \alpha_c) \cdot F}{RT} \eta$	$j_{side}^{Li} = -i_{0,side} a_s \exp(-\frac{\alpha_{c,side} n_{side} F}{RT} \eta_{side})$
over-potential	$\eta = \phi_s - \phi_e - U_{eq} - \frac{R_{SEI}}{a_S} j_{total}^{Li}$	$\eta_{side} = \phi_s - \phi_e - U_{eq,side} - \frac{R_{SEI}}{a_S} j_{total}^{Li}$
equilibrium potential	$U_{eq-} = U_{eq-}^{\Theta}(x) + \frac{RT}{nF} \ln(\frac{c_{e-}}{c_{e0}})$ $U_{eq+} = U_{eq+}^{\Theta}(y) + \frac{RT}{nF} \ln(\frac{c_{e+}}{c_{e0}})$	$U_{eq,side} = U_{eq,side}^{\Theta} + \frac{RT}{n_{side} F} \ln(\frac{c_e}{c_{e0}})$
total reaction rate	$j_{total}^{Li} = j^{Li} + j_{side}^{Li}$	
Notes [2]	$U_{eq+}(y) = 3.4323 + 0.8428 \exp\left(-80.2493 y^{1.3198}\right) + 3.2474 \times 10^{-6} \exp\left(20.2645 y^{3.8003}\right)$ $- 3.2482 \times 10^{-6} \exp\left(20.2646 y^{3.7995}\right)$	

The equilibrium potential of main reaction, U_{eq}, is a function of the stoichiometric number and ion concentration in electrolyte according to the Nernst equation where U_{eq-}^{Θ} and U_{eq+}^{Θ} are the standard equilibrium potential of anode and cathode when $c_e = c_{e0}$, respectively. The equilibrium potential of cathode, U_{eq+}, is estimated by an empirical equation derived from ref. [2]. Then the equilibrium potential of anode, U_{eq-}, can be calculated by the difference between measured OCV and U_{eq+}. However, the standard equilibrium potential of the side reaction, $U_{eq,side}^{\Theta}$, is no longer a function of the stoichiometric number, but depends on the material composition of the electrolyte.

Various recommendation values of $U_{eq,side}^{\Theta}$ are provided by ref. [34], such as 2V, 1.7V, 0.8V and 0.4V. The specific value of $U_{eq,side}^{\Theta}$ in this model is obtained by fitting experimental data of terminal voltage at various operating conditions.

3.3.2 Analysis of degradation effects of side reaction

The degradation effects of LiBs are inextricably linked to the side reaction. The schematic diagram of degradation mechanism is depicted in Fig. 30. Loss of recyclable lithium ions, loss of AM, growth of SEI and DL and electrolyte solvent consumption pertaining to main degradation effects are considered in the physics-based degradation model. The yellow shade in Fig. 30 denotes the byproducts of the side reaction, which are the major components of SEI and DL. The byproducts located at the interface between electrode particles and electrolyte are SEI, which partially or fully covers the graphite particle surface. The DL is defined as a layer composed of the byproducts that are prone to accumulate at the interface between the composite anode and the separator. The particles with marker "X" represent the totally isolated electrode particles which cannot be involved in any further chemical reaction.

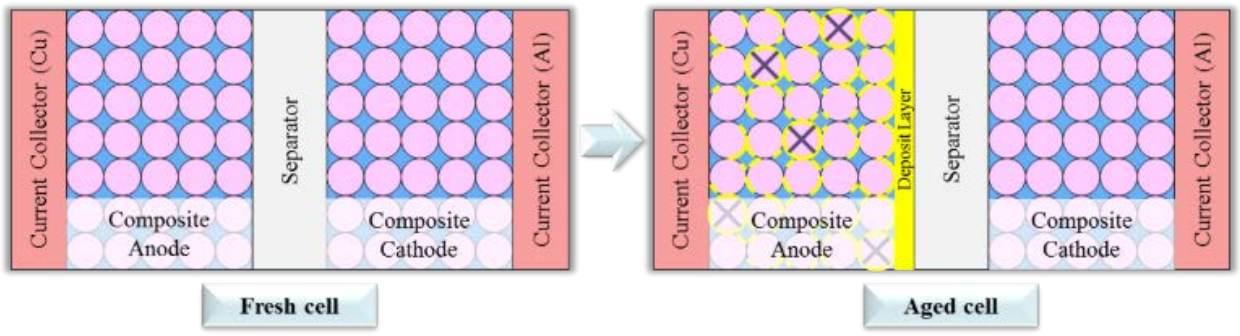

Fig. 30 Schematic diagram of degradation mechanism at anode of a microcell.

The degradation effects resulting from the side reaction can be discussed from two aspects, the consumption of the reactants and the accumulation of the products. With regard to the analysis of the reactants, the amount of consumed lithium ions in the side reaction can be calculated by integrating the side reaction rate over time and volume of the composite anode.

$$q_{side}^{Li}(t) = \int_{x=0}^{\delta_-} \left(\int_{\tau=0}^{t} j_{side}^{Li}(x,\tau) d\tau \right) A dx \tag{22}$$

where q_{side}^{Li} is the amount of consumed lithium ions with a unit of Ah. δ_- is the thickness of the composite anode. A denotes the cross section area of the LiB.

The consumption of the electrolyte solvent is analyzed by the change of the volume fraction of electrolyte, given by Eq.(23).

$$\frac{\partial \varepsilon_e}{\partial t} = -\frac{\alpha \tilde{V}_e}{\delta_- F} \int_{x=0}^{\delta_-} j_{side}^{Li} dx \tag{23}$$

where ε_e is the volume fraction of electrolyte solvent. $\tilde{V}_e$ is the molar volume of the electrolyte. α is a dimensionless coefficient indicating how many moles of the electrolyte solvents are involved in the side reaction when one mole of the lithium ions is consumed.

Provided that the byproducts of the side reaction are only Li_2CO_3 and $(CH_2OCO_2Li)_2$, the consumed molars of the electrolyte solvent are 0.5 and 1, respectively. Under the assumption of the same reaction rate for Eq.(19) and Eq.(20), α equals to 0.75. Correspondingly, the decrease of the volume fraction of the electrolyte solvents leads to a decrease of the effective diffusion coefficient in the electrolyte.

$$D_e^{eff} = D_e \cdot \varepsilon_e \tag{24}$$

The increasing rate of the SEI thickness is proportional to the reaction rate of the side reaction, given in Eq.(25).

$$\frac{\partial \delta_{SEI}}{\partial t} = -\frac{\tilde{V}_{SEI}}{2a_s F} j_{side}^{Li} \tag{25}$$

where δ_{SEI} and $\tilde{V}_{SEI}$ are the thickness and molar volume of the SEI layer, respectively.

The resistance increase of the SEI layer is given in Eq. (26).

$$\Delta R_{SEI} = \delta_{SEI} / \kappa_{SEI} \tag{26}$$

where κ_{SEI} is the ion conductivity of the SEI.

The growth of the SEI layer limits the accessible area of composite electrode, which causes the loss of AM, described in Eq.(27).

$$\Delta \varepsilon_s = -k_s a_s \delta_{SEI} \tag{27}$$

where ε_s is the volume fraction of the active electrode material, and k_s is a dimensionless coefficient.

The increasing rate of the thickness and impedance of the DL are described in Eq.(28) and Eq.(29).

$$\frac{\partial \delta_{DL}}{\partial t} = -\frac{R_s \tilde{V}_{DL}}{2F} j_{side, x=\delta_-}^{Li} \tag{28}$$

$$\Delta R_{DL} = \delta_{DL} / \kappa_{DL} \tag{29}$$

Where δ_{DL}, $\tilde{V}_{DL}$ and κ_{DL} are the thickness, molar volume and ion conductivity of the DL, respectively.

Since the LFP/graphite cells discussed in this research is difficult to get aged, the degradation effects of side reaction rate and other corresponding parameters, such as volume fraction of electrode and electrolyte, resistance of the SEI and DL, ion loss and AM loss, can be better analyzed by the validation results at 55°C. The distribution of side reaction rate along the

direction of anode thickness as a function of cycle number is depicted in Fig. 31. The x-axis and y-axis denote the dimensionless anode thickness and side reaction rate, respectively. The dimensionless anode thickness, $\delta_{-}=0$ and $\delta_{-}=1$, illustrates the location of the interface between copper current collector and the composite anode and that between the composite anode and separator, respectively. The analysis has shown that side reaction rate at the anode/separator interface is higher due to the higher ion concentration. The lithium ions are accumulated at the anode/separator interface in a charging period, which promotes the side reaction and results in the formation of the DL. In addition, as the number of cycles increases, the side reaction rate increases as well, which induces the growth of SEI.

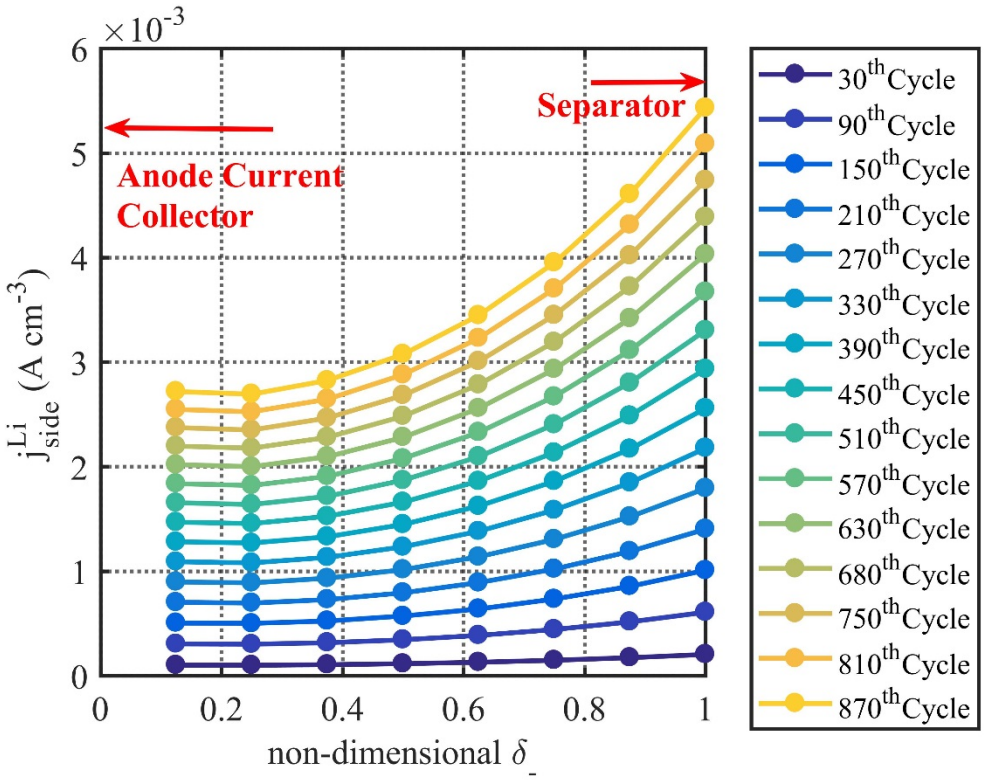

Fig. 31 Distribution of side reaction rate along the direction of anode thickness as a function of cycle number

Lithium ions, as the reactants, are continuously consumed due to the participation in the side reaction. The loss of recyclable ions as a function of cycle number is plotted in the upper subplot of Fig. 32. As the prolonged cycling proceeds, the byproducts of side reaction are accumulated resulting in the growth of SEI layer which can clog pores and isolate particles so that the accessible area gets reduced. The AM losses with the increasing cycle number are shown in the lower subplot of Fig. 32. Both ion losses and AM losses are accumulated as the LiBs get aged.

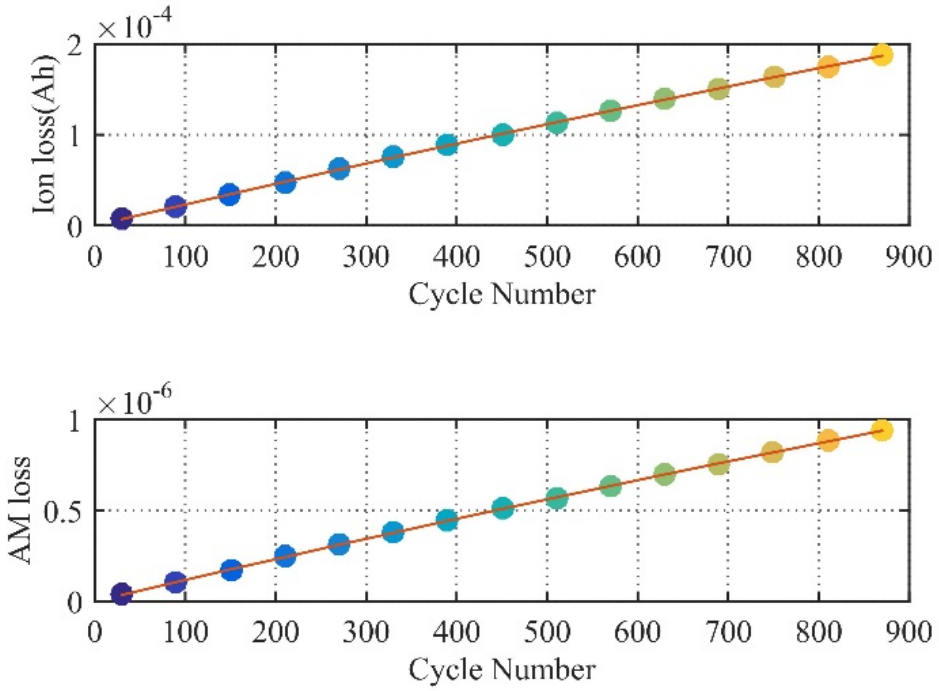

Fig. 32 Analysis of ion losses and AM losses as a function of cycle number

The variations of SEI resistance and electrode volume fraction over time along the anode thickness direction are plotted in Fig. 33. Accordingly, the resistance of SEI (R_{SEI}) increases, while the electrode volume fraction (ε_s) decreases over time.

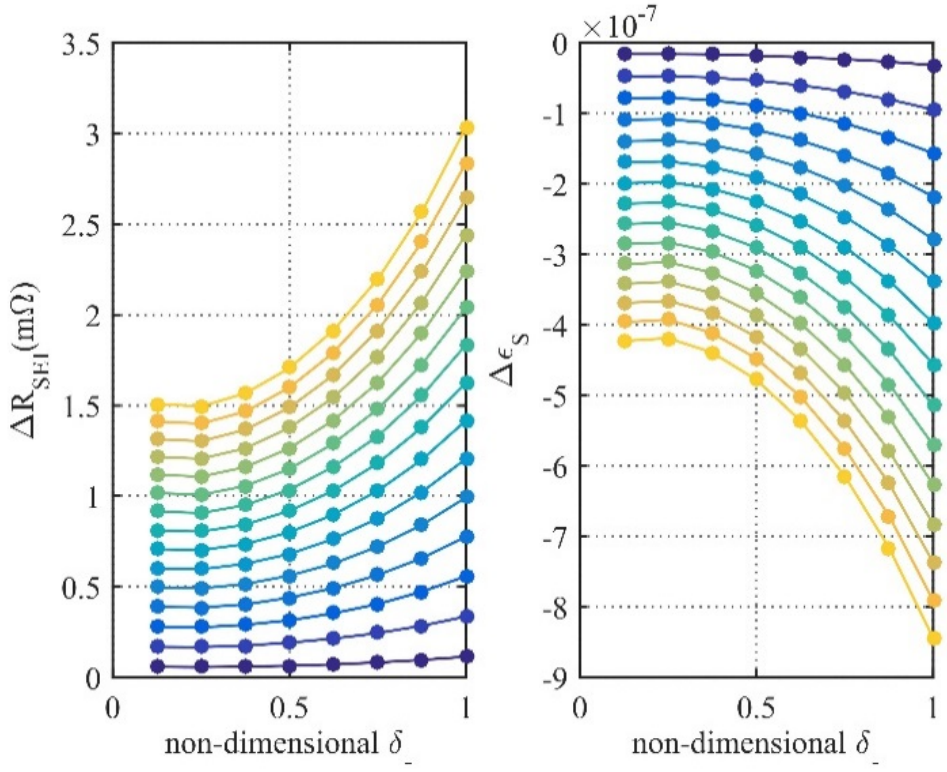

Fig. 33 Analysis of the change of SEI resistance and volume fraction of anode as a function of cycle number

The variations of electrolyte volume fraction and resistance of the DL as a function of cycle number are plotted in Fig. 34. According to the side reaction describing by Eq. (19) and (20), the electrolyte, as one of the reactants, is consumed continuously, which leads to the decrease of electrolyte volume fraction (ε_e). The thickness of the DL increases over time, so that the resistance of DL (R_{DL}) increases with the increasing cycle number. In summary, the analysis of the degradation effects of side reaction based on the variation of the electrochemical parameters can be summarized in Table 8.

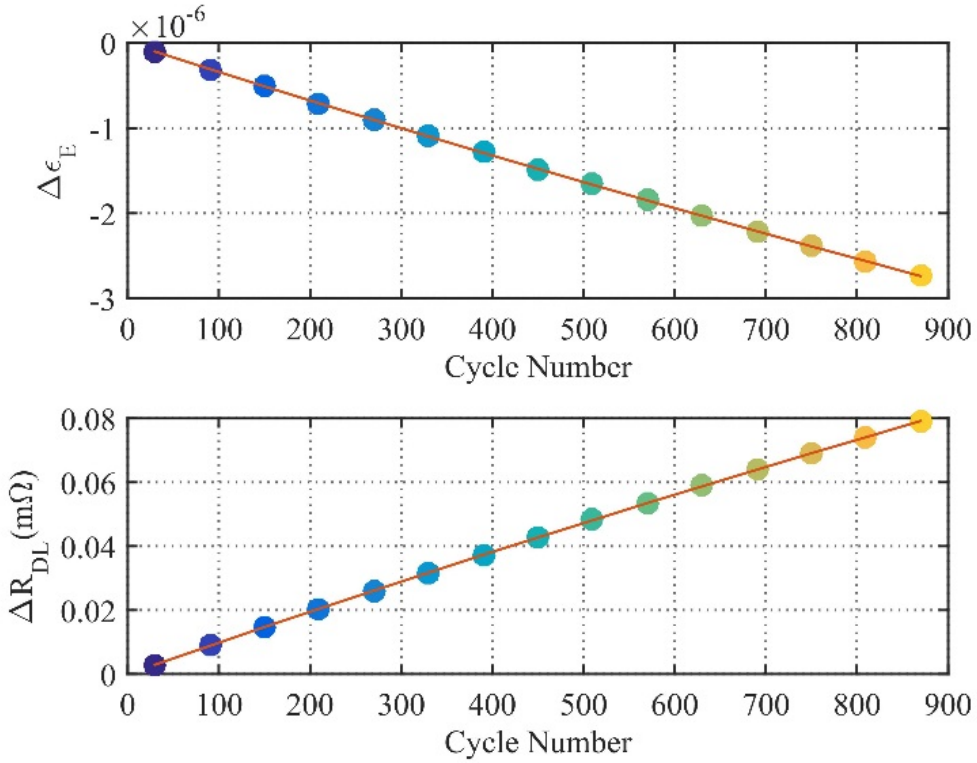

Fig. 34 Analysis of the change of electrolyte volume fraction and resistance of DL as a function of cycle number

Table 8 Degradation effects and parameters of side reaction

Causes	Effects	Degradation parameters	Consequences
Side reaction rate $\left\|j_{side}^{Li}\right\| \uparrow$	Ion loss	$q_{side}^{Li}(t) \uparrow$	Capacity fade
	AM loss	Electrode volume fraction $\varepsilon_s \downarrow$	Capacity fade
	SEI growth	SEI resistance $R_{SEI} \uparrow$	Impedance rise
	DL growth	DL resistance $R_{DL} \uparrow$	Impedance rise
	Electrolyte consumption	Electrolyte volume fraction $\varepsilon_e \downarrow$	Impedance rise

3.4 Validation of end-of-life (EoL)

Compared with the effects of temperature, those of SOC cycling limit, SOC level and charging C-rate have less influence on the degradation of LFP/graphite cells. [41] Thus, temperature, as the key factor to accelerate degradation, will be investigated in more details. For prolonged cycling, the comparisons of terminal voltage with 1C-rate discharging current applied between simulation results obtained using the physics-based degradation model and experimental data measured from the cells cycled at 25°C, 40°C and 55°C, are plotted in Fig. 35, Fig. 36 and Fig. 37, respectively. The dots and solid lines denote the simulations and experiments, respectively. The simulations well capture the variations of terminal voltage with experiments. The prediction of terminal voltage is estimated up to 1080, 900 and 870 cycles at 25°C, 40°C and 55°C, respectively.

As the cell gets aged with the increasing number of cycles, the time to reach EoD voltage has been reduced, which implies the reduction of releasable capacity. Due to side reaction, an extra voltage drop resulting from the SEI is considered in the estimation of terminal voltage. It is observed that terminal voltage at the same SOC drops with the cell getting aged. Both the decrease of releasable capacity and terminal voltage at the same SOC are enhanced by the elevated operating temperature.

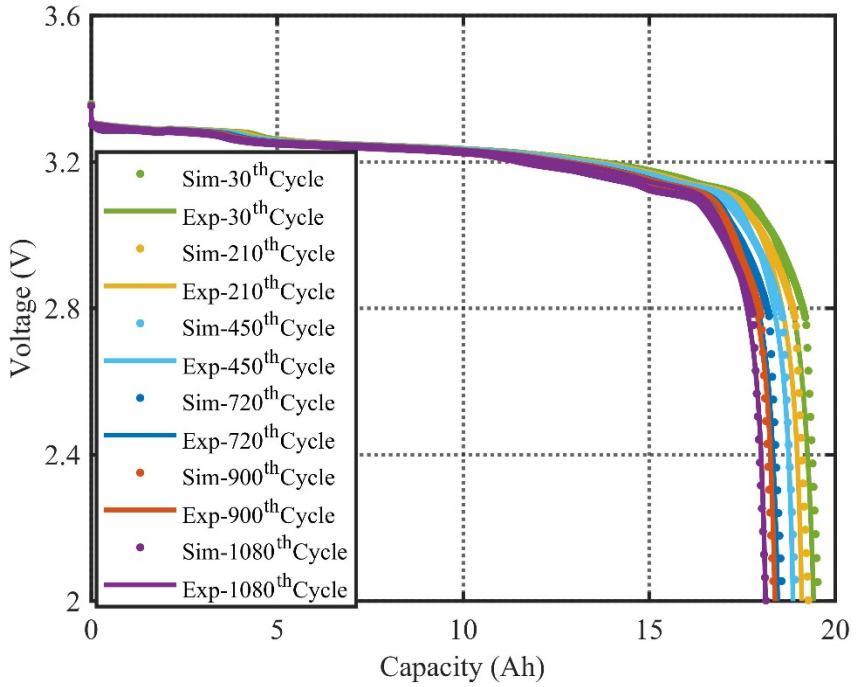

Fig. 35 Validation of discharge behaviors by 1C-rate current for EoL at 25°C

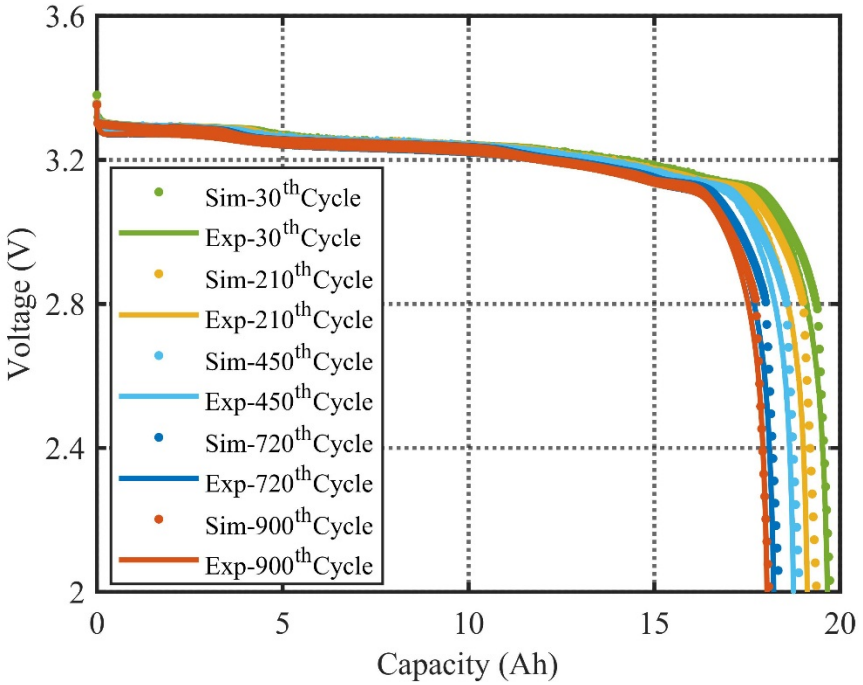

Fig. 36 Validation of discharge behaviors by 1C-rate current for EoL at 40°C

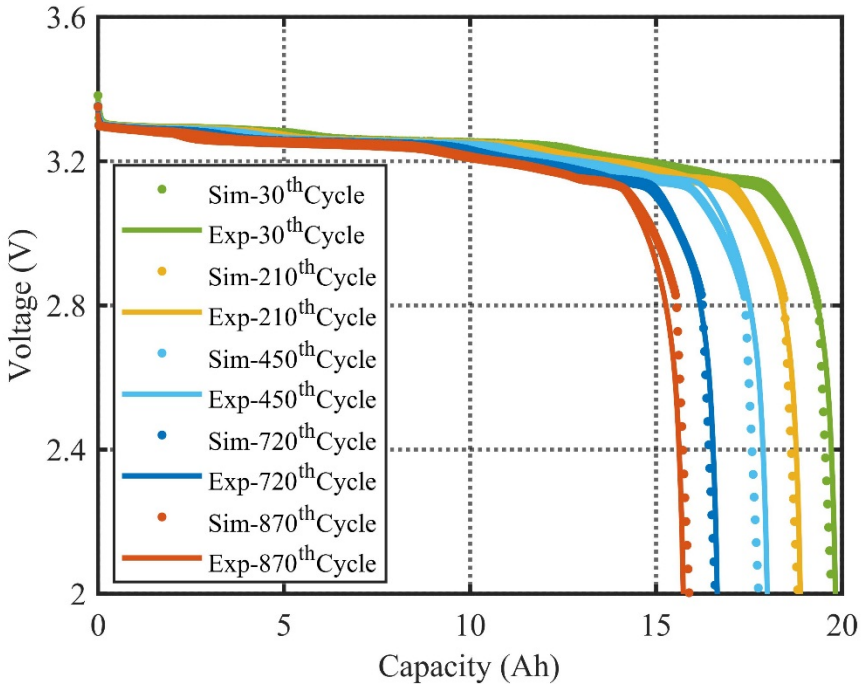

Fig. 37 Validation of discharge behaviors by 1C-rate current for EoL at 55°C

Capacity fade is one of the most significant criteria to evaluate performance of degraded LiBs, which is mainly caused by ion loss and AM loss. The comparison of simulated capacity and the Ah-based measured capacity as the function of cycle number is shown in the upper subplot of Fig. 38. Furthermore, the corresponding error between measurements and simulation results is plotted in the lower subplot. In order to display the capacity variations comparably, the dimensionless capacity retention is defined as the capacity ratio of the aged cell over the fresh cell in Eq.(30). The relative capacity error is calculated by Eq.(31).

$$\mathrm{SOH}_Q = \frac{Q_{aged,cell}}{Q_{fresh,cell}} \times 100\% \tag{30}$$

$$Q_{error} = \frac{Q_{\exp} - Q_{sim}}{Q_{\exp}} \times 100\% \tag{31}$$

The color of purple and red, orange and yellow, and cyan and blue in the upper subplot of Fig. 38 denotes the capacity retention calculated based on experimental data and simulation results at 25°C, 40°C and 55°C, respectively. The error shown in the lower subplot of Fig. 38 is within 1%, 2%, and 2% at 25°C, 40°C and 55°C, respectively.

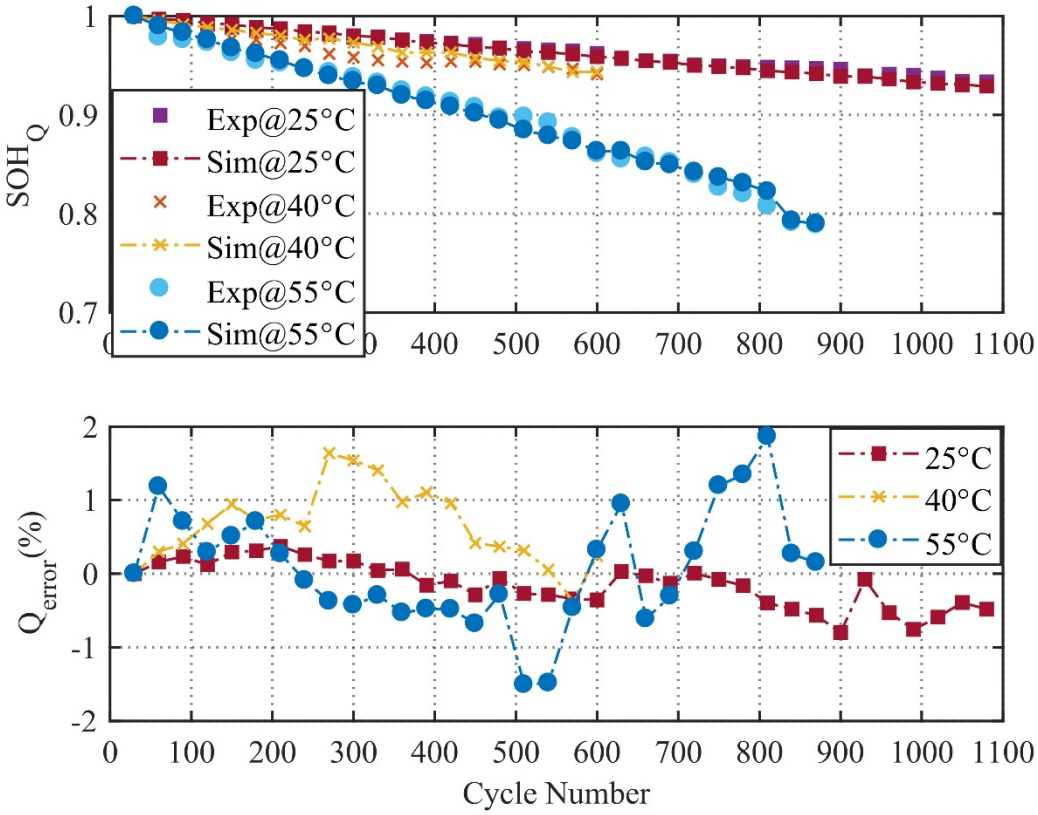

Fig. 38 Comparison between Ah-based measured capacity and simulated capacity at 25/40/55°C

The other major consequence of degradation is the rise of impedances that leads to power fade. The ion-consuming SEI and DL growth and the dryness of electrolyte due to side reaction result in the power fade. The SEI resistances extracted from the ECM based on the EIS experimental data are compared with the simulated results obtained from the integrated degradation model at different operating temperatures, which is shown in Fig. 39. The markers of cross, 'X', and circle, 'O', represent experimental data and simulation results, respectively. The growth of SEI resistance matches well with each other. The comparison manifests that elevated operating temperature accelerates the degradation of LFP/graphite cells.

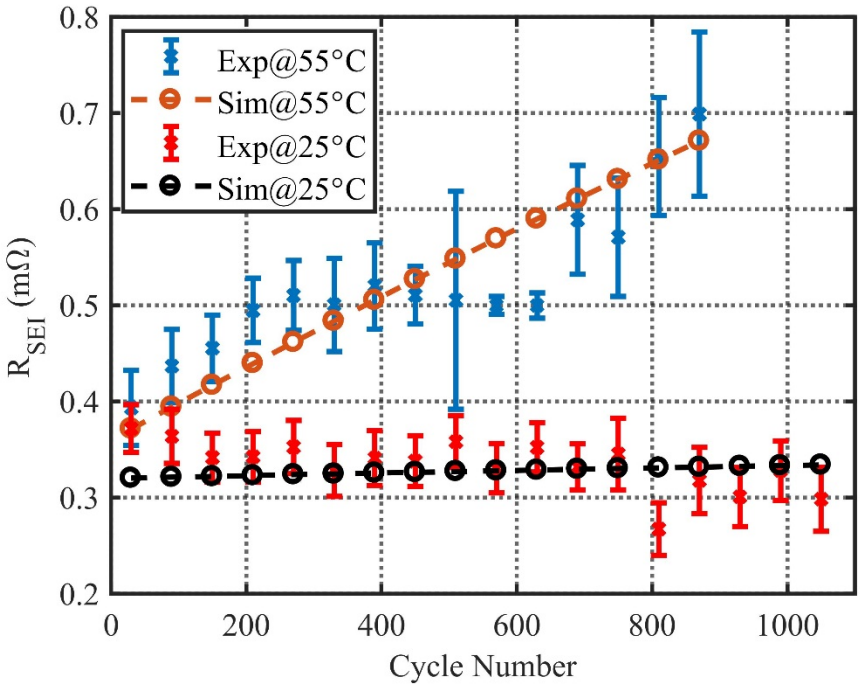

Fig. 39 Comparison of SEI resistance at different temperatures with increasing cycle number

Power fade is predicted at different operating temperatures as shown in Fig. 40. The upper subplot displays the comparison of power between measurements and simulations at different

operating temperatures. The lower subplot presents the corresponding error of power at 25°C and 55°C, respectively. With consideration of the change of ionic conductivity of SEI and DL, the power decreases as the increase of cycle number. The overall error of power estimation is within 3%.

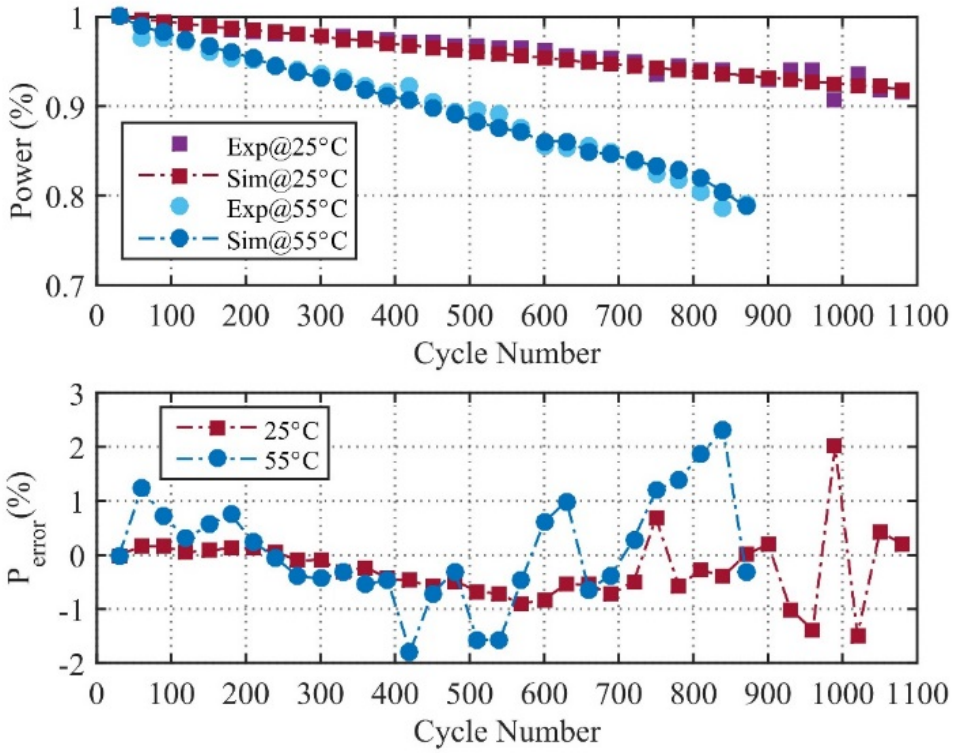

Fig. 40 Comparison of power fade at different temperatures with increasing cycle number.

3.5 Summary

A physics-based degradation model considering side reaction has been developed and validated by LFP/graphite cells cycling at different operating conditions, such as temperatures, SOC cycling limits and SOC levels. According to the experimental studies on degradation

mechanism, side reaction has been identified as the predominant cause for both calendar and cycle life, which is accelerated by the elevated temperatures, high SOC levels and large SOC cycling limits. These phenomena are formulated by modifying BV equation that is incorporated into the developed ROM with EKF. The capacity fade is caused by loss of recyclable lithium ions and loss of AM, while the power fade is the growth of SEI and DL and electrolyte solvent consumption. The estimation error of capacity and power as the function of cycle number at different temperatures have been remained within 2% and 3%, respectively.

Chapter 4. Physics-based degradation model considering lithium plating/stripping at low temperatures

4.1 Literature review

When LiBs are operated in low ambient temperatures, the capability of delivering or accepting energy or power drops, which is a dramatic limitation of lifetime and safety issues. Particularly under charging, the lithium ions are inclined to form metallic lithium that is deposited on instead of intercalating into the negative electrode, which is called “lithium plating”, also known as “lithium deposition reaction”. As unwanted side reaction, the lithium deposition reaction leads to capacity and power fade, impedance rise, and the growth of dendritically metallic lithium even triggers internal short circuit [56]. Therefore, understanding of mechanisms and effects of the lithium plating on battery performances at low temperatures is of crucial significance for safe and durable design of LiB systems.

At the temperatures larger than 0^{o}C, side reaction is regarded as the dominant cause for degradation and is accelerated by the elevated temperatures, large SOC cycling limits and high SOC levels, which has been extensively investigated [31,34,35,39,40,57]. Lithium ions and electrolyte solvents take part in side reaction at the interface between electrode and electrolyte to form the unsolvable byproducts, lithium carbonate (Li_2CO_3) and lithium ethylene dicarbonate ($(CH_2OCO_2Li)_2$), which are the main compounds in SEI. In contrast, at low temperatures, due to the sluggish charge transfer kinetics and low diffusivities of lithium ions, lithium plating is prone to

take place. Schematic diagram of degradation mechanisms on anode at low temperatures is depicted in Fig. 41. At initial cycles, a thin layer (primary SEI: Yellow Color) is formed at the interface between carbon particles and electrolyte to protect the electrode from further corrosion and the electrolyte from being decomposed by participating in chemical side reaction. Since the SEI is conductive to lithium ions, but isolative to electrons, the lithium plating occurs at the interface between carbon particles and the primary SEI to form metallic lithium (Red Color) at low temperatures. The plated lithium can react with electrolyte solvents to form the secondary SEI (Blue Color) that has the same compounds as the primary SEI. Formation of the primary SEI, plated lithium, and secondary SEI only occur under charging.

At discharging, the plated lithium can be partially dissolved and extra lithium ions are released, which results in a certain amount of reversible capacity, called “lithium stripping”, also known as “lithium dissolution reaction”. If the dissolved lithium ions are unfortunately fully covered by the pre-formed SEI, the ions are isolated, which is called “dead lithium”, resulting in the irreversible capacity loss. Therefore, the lithium deposition/dissolution reaction contains both reversible and irreversible processes that are accelerated by the decreasing temperatures.

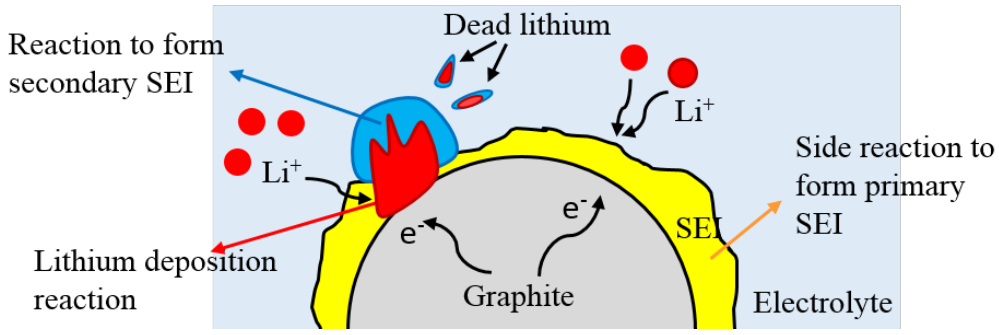

Fig. 41 Schematic diagram of degradation mechanisms on anode at low temperature

Due to the detrimental effects of lithium plating on battery performances, considerable efforts have been made to develop methods to detect the onset of metallic lithium and its growth, experimentally and mathematically. In-situ and ex-situ experimental techniques have been proposed [58]. The in-situ experiments [59–62] include constant charging/discharging, incremental capacity measurement, differential analysis [63] and EIS etc. in the field of electrochemistry, while in-situ neutron diffraction method [64,65] in the field of material. The ex-situ techniques mainly imply to the postmortem analysis [66], such as SEM (Scanning Electron Microscope) [67–71], XRD (X-Ray Diffraction) [72,73], XPS (X-Ray Photoelectron Spectroscopy) [74], and TEM [75]. However, in most cases, only the dendrite-like morphology has been detected without any evidence of the compounds in the deposits. Moreover, few calculate the amount of the plated lithium quantitatively.

Numerical approach by modeling the behaviors of lithium plating is a great way to quantify the amount of plated lithium. Arora et al. [76] firstly proposed the equations that describe the lithium deposition reaction at overcharge based on Doyle's model [4]. Tang et al. [77] improved the Arora's model to 2D and found that the lithium deposition tended to occur at electrode edges and an extension of the anode edge was capable of preventing the onset of lithium plating. Perkins et al. [78] developed a control-oriented ROM of lithium overcharge deposition in order to accomplish an optimal design of a tradeoff between LiB performance and durability. Most recently, Ge et al. [79] validated the charging behaviors of fresh cells at low temperatures and extracted part of parameters by nuclear magnetic resonance (NMR). Yang et al. [80] proposed a physics-based aging model considering lithium plating to describe the transition from linear to nonlinear behaviors at room temperature. However, none of the electrochemical model was capable of

estimating the degradation effects caused by both lithium plating and lithium stripping simultaneously at low temperatures.

In this section, effects of lithium plating and lithium stripping on the degradation will be experimentally analyzed and quantified, which enables to predict the capacity and power fade, particularly at extremely low temperatures. The degradation effects include loss of recyclable lithium ions, loss of AM, growth of plated lithium and secondary SEI, and the consumption of electrolyte. In addition, a physics-based electrochemical-thermal model considering lithium plating/stripping is developed and validated against both fresh and aged cells at different operating conditions, including temperatures, charging and discharging C-rates.

4.2 Experimental analysis

Since LFP/graphite cells tested in upper temperatures are hard to get aged and the degradation effects mainly take place on anode, NMC/Carbon LiBs whose active material of anode is the same as LFP based cells are chosen to be the alternative. The specifications of the NMC/Carbon cells are summarized in Table 9.

Table 9 Specifications of testing cells

Material	Cathode	NMC622 ($Li(Ni_{0.6}Mn_{0.2}Co_{0.2})O_2$)
	Anode	Carbon (NG 70% + AG 30%)
EoC voltage, current		4.2V, 3A
EoD voltage		2.5V
Nominal capacity @ 1/3C-rate		58.9Ah
Dimension (mm^3)		99.7×301.5×13.3

To explore the performance of fresh cells at low temperatures, the OCV as a function of SOC is measured at the ambient temperature of -20°C by a very small current of 1/30 C-rate (≈ 2A) with sufficient resting no less than 1h at each testing point in order to allow the terminal voltage and OCV to be equal in the maximum likelihood. For BoL, the cell is charged by a constant current (CC) followed by a constant voltage (CV, 4.2V) protocol until reaching a cutoff current of 3A. After resting for 30 minutes, the cell continues to be discharged by CC to 2.5V. The constant current applied at charging and discharging profile varies among 1/2C-rate, 1/3C-rate, 1/4C-rate and 1/10C-rate at different temperatures (-20/-25/-30°C).

For EoL, the cells are involved into the cycling tests according to the test matrix summarized in Table 10. Effects of operating temperatures (0/-10/-20/-25/-30°C), charging and discharging current rates (1/3C-rate, 1/4C-rate) on the electrochemical performance of LiBs are discussed. Each consecutive cycle is performed by a CC-CV charging and CC discharging protocol. Periodically, the cell is detached from cycling and conduct a series of reference performance tests (RPTs) at 25°C, including the measurement of capacity, power and EIS. In each RPT, the capacity is measured as follows: (1) Charge the cell using a CC-CV protocol (CC: 1/3C-rate, CV: 4.2V, EoC current: 3A); (2) Rest for 30 minutes; (3) Discharge the cell by 1/3C-rate current to 2.5V. The power is measured: (1) Charge the cell to 50% SOC using 1/3C-rate current; (2) Pulse charge and discharge by 1/3C-rate current: 2s discharge – 2s rest – 2s charge – 30s rest – 10s discharge – 10s rest – 10s charge – 30s rest – 30s discharge – 30s rest – 30s charge – 30s rest. EIS is measured: (1) Charge the cell to 50% SOC by 1/3C-rate CC; (2) Rest for 3h; (3) Conduct EIS test at the frequency from 10mHz to 1kHz. After cycling, the cells are discharged to 0% SOC and dissembled in a glove box fulfilled with argon gas to perform post-mortem analysis. The morphological variation and

identification of the compounds in the deposits are performed by SEM and FTIR (Fourier Transform Infrared Spectroscopy), respectively.

Table 10 Test conditions

Temperature (°C)	Charge/discharge current		SOC cycling limit	Cycle No.	Capacity fade
0	0.25C/0.25C			8	1.4%
-10	0.25C/0.25C			8	1.7%
	Effects of	(1/3)C/(1/3)C		8	29.8%
-20	charging	0.25C/0.25C	0-100%	8	24.1%
	C-rate	0.25C/(1/3)C		8	14.3%
-25	0.25C/0.25C			6	21.1%
-30	0.25C/0.25C			6	43.9%

Fig. 42 presents the capacity retention of the cells cycled at different operating conditions. The upper subplot shows the capacity retention at various temperatures (-30 ~ 0°C), where the capacity decay is accelerated by the lower temperatures. In order to allow the lithium plating/stripping to take place to the most degree, the cells cycled at the temperatures lower than -20°C become preferential selections. The lower subplot shows the capacity retention at various charging and discharging current rates (1/3C-rate, 1/4C-rate) at -20°C. When the cell is charged at the same current, the same amount of lithium metal is plated. Due to the existence of lithium stripping at discharge, larger discharging C-rates promote the exfoliation of plated lithium, resulting in more capacity reversed and less capacity fade. When the same discharging current is applied, larger charging current leads to more lithium plating formed and more capacity fade.

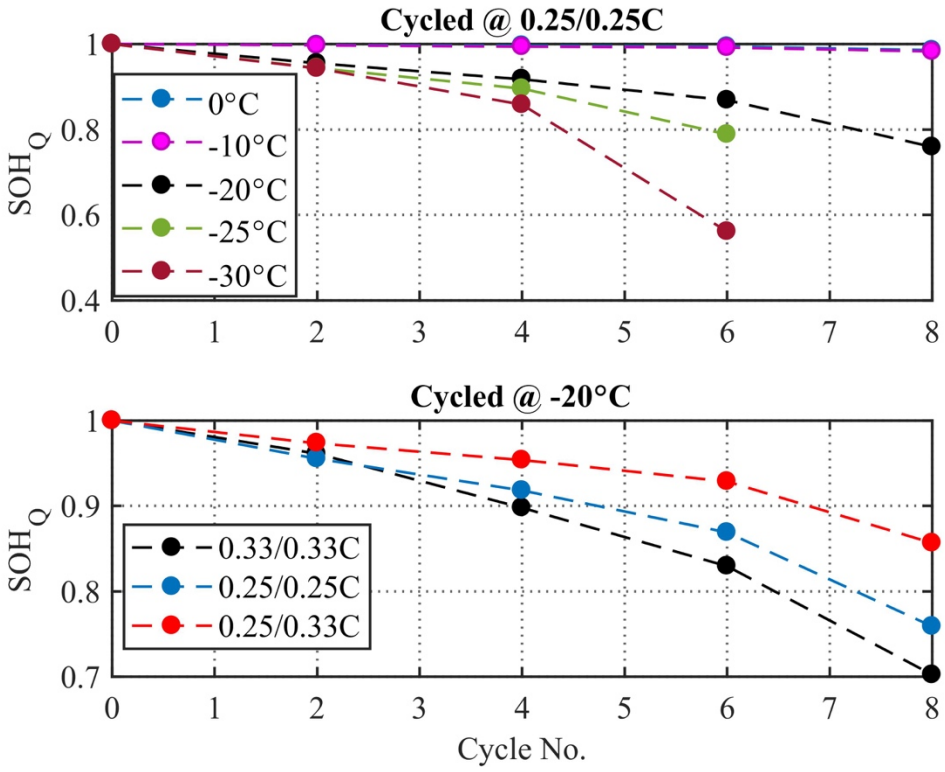

Fig. 42 Capacity retention at different cycling conditions, including operating temperatures, charging and discharging current rates

The impedance spectra of the cell cycled by 1/4 C-rate charging/discharging current at the temperature of -20°C are shown in Fig. 43. In this case, the dominant cause of impedance rise is lithium plating. Due to the reaction of secondary SEI formation, the electrolyte solvents are consumed as reactants to increase the Ohmic resistance, which is represented by the rightward shift of impedance spectrum. Besides the spectrum at 8th cycle, the radius of the first semi-circle only has a slight variation, which illustrates that the SEI resistance does not have large changes.

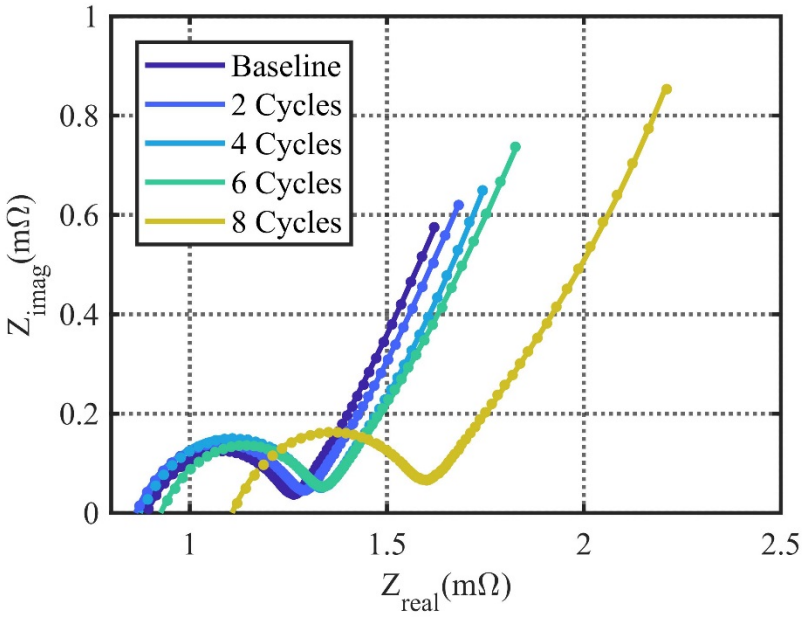

Fig. 43 Impedance spectra of the cell cycled by1/4C-rate charging/discharging current at -20°C

By means of the ECM, the Ohmic and SEI resistances of the cell cycled at the same condition as Fig. 43 are extracted and displayed in Fig. 44. The capacity retention as a function of cycle number is treated as a reference. Due to the ignorance of side reaction, only source of the SEI resistance comes from the products of the reaction taking place between the plated lithium and electrolyte solvents, which is called secondary SEI. Therefore, the slight variation of SEI resistance at the first 6 cycles implies that the ignorance of side reaction at temperatures below -20°C is reasonable, while the increase of SEI resistance at the last 2 cycles results from the secondary SEI formation.

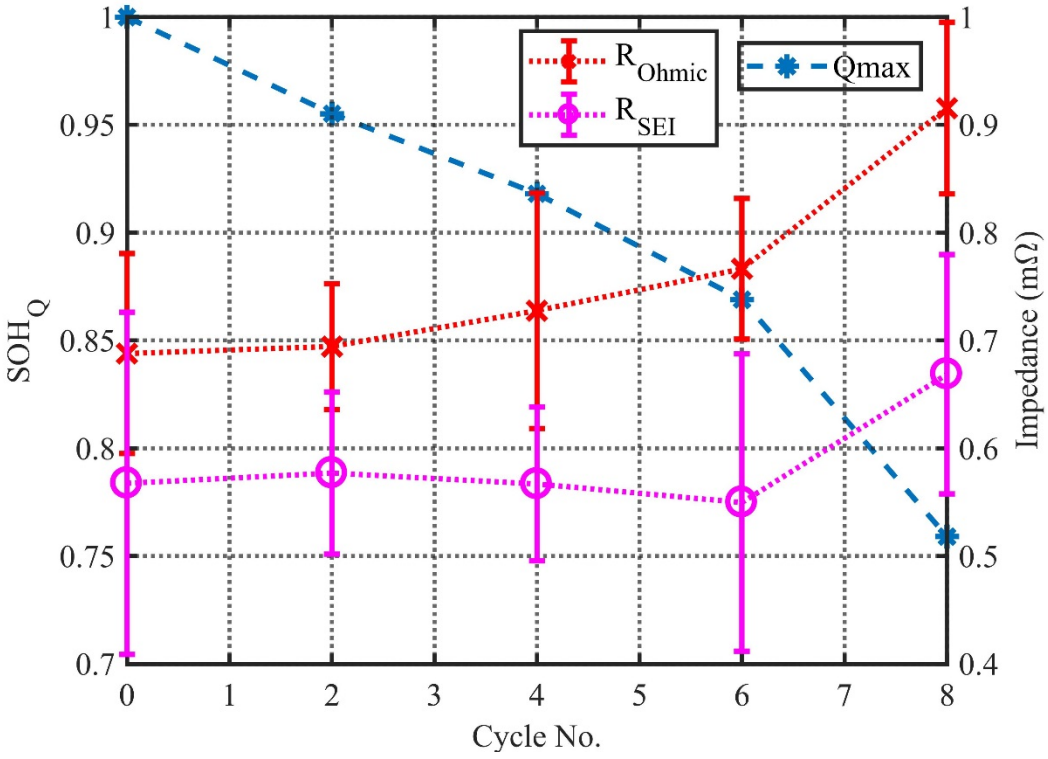

Fig. 44 Experimental analyses of Ohmic and SEI resistances with the reference of capacity retention for the cell cycled by 1/4C-rate charging/discharging current at -20°C

Fig. 45 shows the impedance spectra of the cell cycled by 1/3 C-rate charging/discharging current at -20°C, which is compared with those plotted in Fig. 43 to explore the effects of charging C-rates on degradation from the aspect of impedances. The elevated charging C-rate provokes the occurrence of lithium plating and induces more degradation. The impedance spectrum at the same cycle number shifts rightwards further when 1/3 C-rate charging current is applied. The increasing rate of impedance are enhanced by large charging currents.

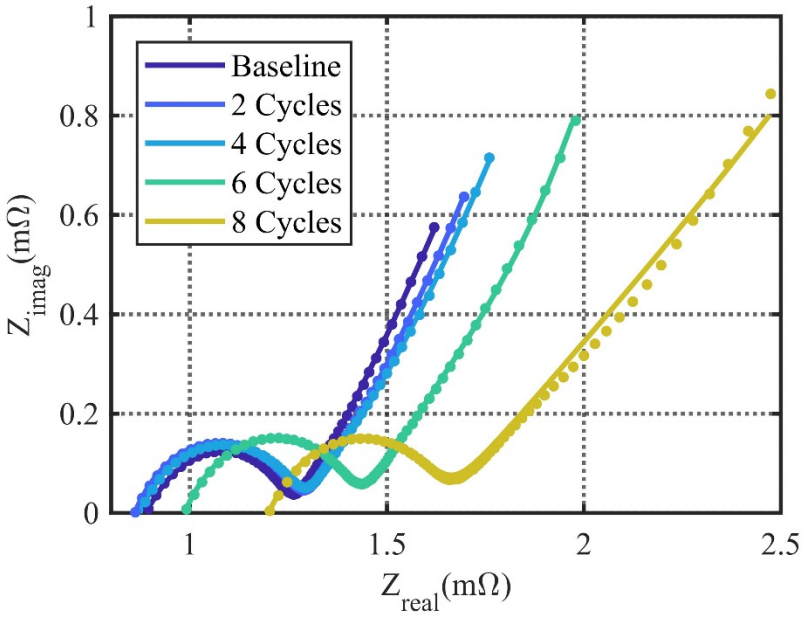

Fig. 45 Impedance spectra of the cell cycled by1/3C-rate charging/discharging current at -20°C

With regard to the effects of temperature on degradation, the impedance spectra of the cells cycled at -25°C and -30°C are depicted in Fig. 46 and Fig. 47, respectively. Compared with the behaviors at -20°C, both the shift of impedance spectrum and the increase of the semi-circle radium are strengthened with the decrease of temperature.

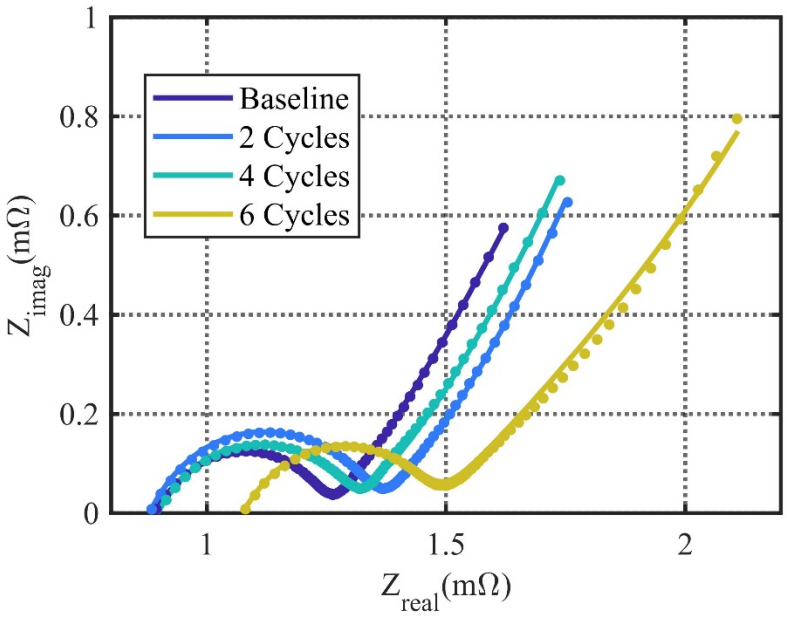

Fig. 46 Impedance spectra of the cell cycled by1/4C-rate charging/discharging current at -25°C

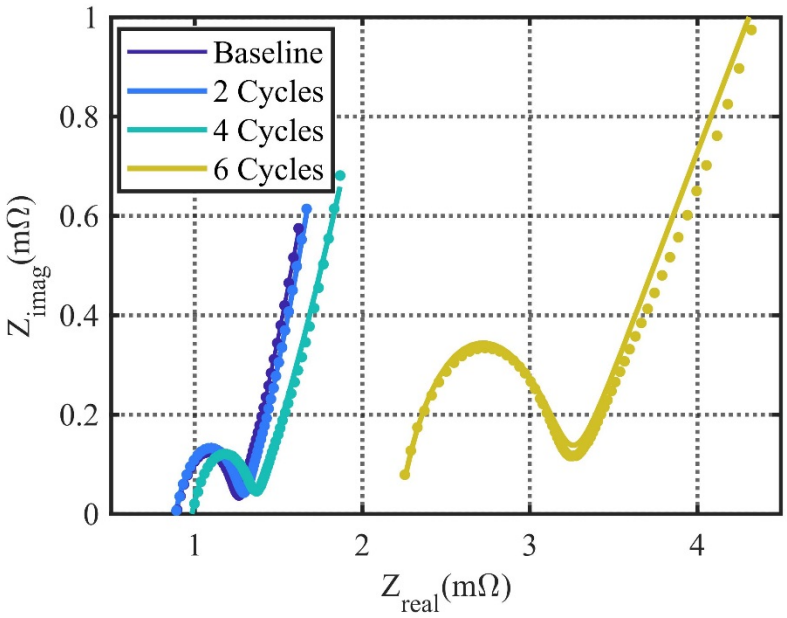

Fig. 47 Impedance spectra of the cell cycled by1/4C-rate charging/discharging current at -30°C

Fig. 48 shows the FTIR analyses of the cells cycled at various operating conditions. The peaks represent the existence of the compounds, Li_2CO_3 and $ROCO_2Li$, which are the main components of SEI. Due to the ignorance of side reaction, the SEI detected by FTIR comes from the products of the reaction between lithium metal and electrolyte solvents, which can be regarded as an indirect evidence of the existence of lithium plating.

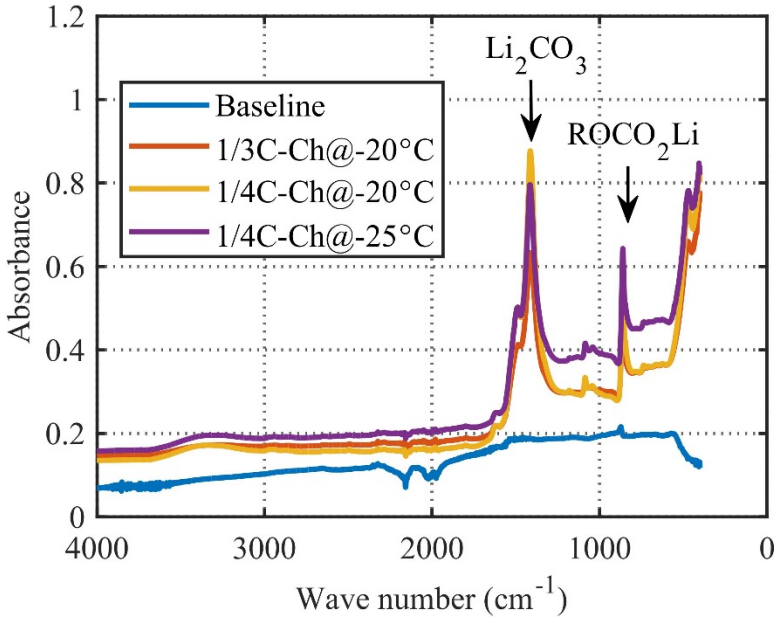

Fig. 48 FTIR analyses of cells cycled at various operating conditions

4.3 Mathematical principles

4.3.1 Modeling of lithium plating/stripping

In order to develop a physics-based electrochemical model to investigate the electrochemical performances of both fresh and aged LiBs at low temperatures, some assumptions need to be made in advance.

1. Degradation only takes place on anode.
2. Lithium deposition reaction is semi-reversible, which implies that the reduction rate is 2 times of the oxidation rate.
3. Film at the surface of anode particles in aged cells is a mixture of plated lithium, primary and secondary SEI.
4. Both the primary and secondary SEI are only a mixture of Li_2CO_3 and $CH_2OCO_2Li)_2$.
5. Primary SEI formed at initial cycles is considered as constant.
6. No mechanical failure nor gas generation is considered.
7. No overcharge or undercharge process is considered.

In the present model, the lithium deposition reaction is considered as side reaction, which competes with intercalation on anode at low temperatures. If the local anode overpotential becomes negative referring to Li^+/Li ($\eta_{Li^+/Li} < 0$), the lithium ions are inclined to deposit on instead of intercalating into the negative electrode, as described in Eq. (32).

$$Li^+ + e^- \leftrightarrow Li\,(s) \tag{32}$$

The total reaction rate (j_{total}^{Li}), can be divided to two components, main reaction rate (j^{Li}), and lithium deposition reaction rate ($j_{plating}^{Li}$). Both of main and lithium deposition reaction rate can be described using BV equation, as presented in Eq. (5) and Eq. (34), respectively. The lithium deposition reaction rate is selected from the minimum between 0 and $j_{plating}^{Li}$.

$$j_{total}^{Li} = j^{Li} + j_{plating}^{Li} \tag{33}$$

$$j_{plating}^{Li} = a_s i_{0,p} \left\{ \exp\left[\frac{\alpha_{a,p} n_p F}{RT} \eta_p \right] - \exp\left[-\frac{\alpha_{c,p} n_p F}{RT} \eta_p \right] \right\} \quad (34)$$

where $i_{0,p}$ is the exchange current density of lithium deposition reaction, which is a fitting parameter as a function of temperature due to the lack of reliable experimental data. n_p is the number of lithium ions involved in Eq. (32) with a value of 1. $\alpha_{a,p}$ and $\alpha_{c,p}$ are the dimensionless anodic and cathodic charge transfer coefficient, which are assumed to be a value of 0.33 and 0.67 [76], respectively, due to the assumption of semi-reversible lithium deposition reaction. The activation over-potential of lithium deposition reaction, η_p, is calculated by

$$\eta_p = \phi_s - \phi_e - U_{eq,p} - \frac{R_{film}}{a_s} j_{total}^{Li} \quad (35)$$

where ϕ_s, ϕ_e are the electrode and electrolyte potential, respectively. $U_{eq,p}$, the equilibrium potential, equals to 0, because the measurement is compared with a reference of lithium metal. R_{film} is the overall resistance of the surface film, as defined in Eq. (36).

$$R_{film} = \varepsilon_{Li}\left(\frac{\delta_{film}}{\kappa_{Li}} \right) + \varepsilon_{Li_2CO_3}\left(\frac{\delta_{film}}{\kappa_{Li_2CO_3}} \right) + \varepsilon_{(CH_2OCO_2Li)_2}\left(\frac{\delta_{film}}{\kappa_{(CH_2OCO_2Li)_2}} \right) \quad (36)$$

where κ_{Li} is the electronic conductivity of the plated lithium. $\kappa_{Li_2CO_3}$ and $\kappa_{(CH_2OCO_2Li)_2}$ are the ionic conductivity of Li_2CO_3 and $(CH_2OCO_2Li)_2$, respectively. ε_{Li}, $\varepsilon_{Li_2CO_3}$, and $\varepsilon_{(CH_2OCO_2Li)_2}$ are the volume fraction of lithium metal, Li_2CO_3 and $(CH_2OCO_2Li)_2$ in the film, respectively. δ_{film} is the thickness of the coated surface film.

$$\delta_{film} = \delta_{SEI} + \delta_p \quad (37)$$

where δ_{SEI} and δ_p are the thickness of SEI and plated lithium, respectively.

4.3.2 Analysis of the degradation effects

Since the lithium deposition reaction is partially irreversible, the lithium ions, as the reactants, are continuously consumed as shown in Eq. (32). q_{total}^{Li} is defined as the total amount of ion losses due to lithium deposition reaction, which can be calculated by integrating the reaction rate over the total volume of composite anode

$$q_{total}^{Li} = \int_{x=0}^{\delta_-} \left(\int_{t=0}^{t} j_{plating}^{Li}(x,\tau) d\tau \right) A dx \tag{38}$$

where δ_- is defined as the thickness of composite anode.

As part of metallic lithium in contact with electrolyte can be oxidized to form secondary SEI, a dimensionless parameter, λ, is introduced to denote the fraction of plated lithium that forms secondary SEI. The material balance of SEI and plated lithium can be expressed as

$$\frac{\partial c_{SEI}}{\partial t} = -\frac{1}{2F} \lambda j_{plating}^{Li} \tag{39}$$

$$\frac{\partial c_{Li}}{\partial t} = -\frac{1}{F} (1-\lambda) j_{plating}^{Li} \tag{40}$$

where c_{SEI} and c_{Li} are the molar concentration of SEI and plated lithium per unit volume of anode. In the model, the graphite particles are assumed to be spherical, and the surface film is assumed to be uniform in the thickness direction. As such, the amount of SEI and plated lithium can be transformed to an equivalent thickness of the surface film, defined as the ratio of the total volume of SEI and lithium metal to the specific surface area,

$$\frac{\partial \delta_{film}}{\partial t} = -\frac{\tilde{V}_{SEI}}{2 a_s F} c_{SEI} - \frac{\tilde{V}_{Li}}{a_s F} c_{Li} \tag{41}$$

where $\tilde{V}_{SEI}$ and $\tilde{V}_{Li}$ are the molar volume of SEI and metallic lithium. The first and second term in the right side of Eq. (41) denotes the thickness change of SEI and plated lithium, respectively.

Since both primary and secondary SEI are isolative to electrons, the growth of SEI can limit the accessible area of composite anode, which causes the reduction of volume fraction of the active anode material, ε_s, leading to capacity fade, as shown in Eq.(42).

$$\Delta\varepsilon_s = -k_s a_s \delta_{film} \tag{42}$$

where k_s is a dimensionless coefficient.

Since the plated lithium can react with the contact electrolyte solvents to form the secondary SEI as shown in Eq.(43) and Eq. (44), the consumption of electrolyte solvents resulting in the power fade can be analyzed by the decrease of the volume fraction of electrolyte, ε_e, in Eq. (45).

$$2\mathrm{Li} + \mathrm{EC} \rightarrow \mathrm{CH_2{=}CH_2} \uparrow + \mathrm{Li_2CO_3} \downarrow \tag{43}$$

$$2\mathrm{Li} + 2\mathrm{EC} \rightarrow \mathrm{CH_2{=}CH_2} \uparrow + (\mathrm{CH_2OCO_2Li})_2 \downarrow \tag{44}$$

$$\frac{\partial\varepsilon_e}{\partial t} = -\frac{\alpha\tilde{V}_e}{\delta\_FA} q_{total}^{Li} \tag{45}$$

where $\tilde{V}_e$ is the molar volume of the electrolyte. α is a dimensionless coefficient indicating how many moles of the electrolyte solvents are involved in the reaction when one mole of the metallic lithium is consumed. Under the assumption of the same reaction rate of Eq.(43) and Eq. (44), α equals to 0.75. Correspondingly, the decrease of the volume fraction of the electrolyte solvents leads to a decrease of the effective diffusion coefficient in the electrolyte.

$$D_e^{eff} = D_e \cdot \varepsilon_e \tag{46}$$

The increasing rate of the thickness and impedance of the DL are described in Eq.(47) and Eq.(48).

$$\frac{\partial \delta_{DL}}{\partial t} = -\frac{R_s \tilde{V}_{DL}}{2F} \lambda j^{Li}_{plating, x=\delta_-} \tag{47}$$

$$\Delta R_{DL} = \delta_{DL} / \kappa_{DL} \tag{48}$$

Where δ_{DL}, $\tilde{V}_{DL}$ and κ_{DL} are the thickness, molar volume and ion conductivity of the DL, respectively.

4.4 Results and discussions

4.4.1 Analysis of lithium plating under charging

According to the literature review, the lithium plating criteria is discussed from two aspects, potential and concentration, which are related to charge and mass transfer processes, respectively. At low temperatures, the sluggish charge transfer kinetics introduce a large overpotential as soon as the current is applied, especially for a high current-rate whatever the initial SOC is, which is regarded as charge transfer limitation (CTL). If the cell is charged at a relatively low current-rate, the charge transfer is not a sufficient rate-limiting factor. The poor solid diffusivity of lithium ions can cause a large concentration gradient over the radial direction of the particles, resulting in the accumulation of lithium ions on the surface of carbon particles, which is called “mass transfer limitation” (MTL).

4.4.1.1 Charge transfer limitation

When the temperatures are lower than -20°C, lithium plating becomes the dominant cause for degradation of LiBs. The effects of temperatures and charging C-rates on the lithium plating are discussed from Fig. 49 to Fig. 54. Fig. 49 shows the comparison of terminal voltage under CC-CV charging between experimental data and simulation results at various temperatures (-20/-25/-30°C). The solid lines and markers represent the experiments and simulations, respectively. The responses of terminal voltage have a reasonable match, which verifies the model accuracy.

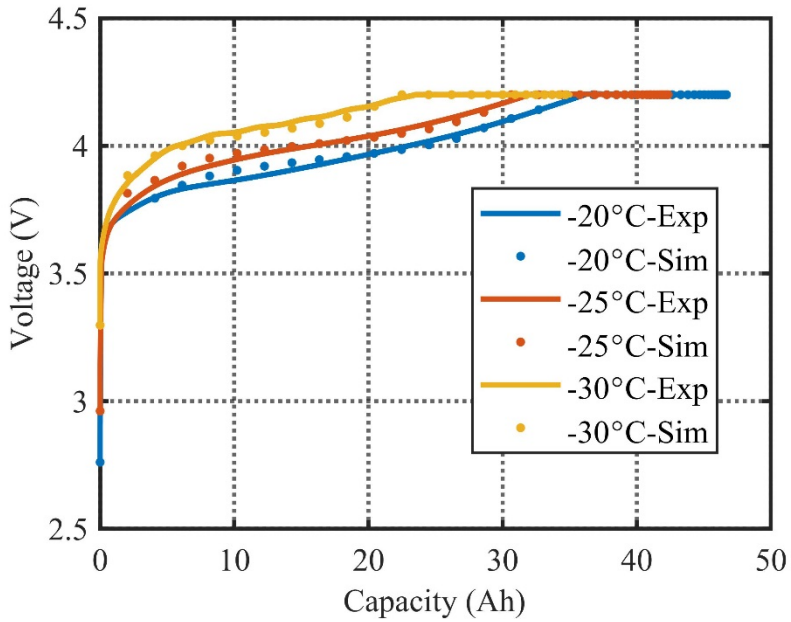

Fig. 49 Comparison of charge behaviors between experimental data and simulation results of the cells with 1/4C-rate current applied at -20/-25°C/-30°C

The electrochemical kinetics of lithium plating are governed by the overpotential as described in Eq. (34). When the overpotential of lithium plating (η_p) drops to be negative, the lithium plating is triggered. The distribution of overpotential of lithium plating along the anode

thickness direction at different temperatures (-20/-25/-30°C) is depicted in Fig. 50. Negative overpotential manifests the existence of lithium plating. As the decreasing temperatures, the value of overpotential becomes more negative, which leads to the increase of the corresponding terminal voltage at the same SOC as shown in Fig. 49. Moreover, the potential drop at the interface between composite anode and separator is larger than that at the other locations on anode, which implies that the lithium plating starts from the separator side.

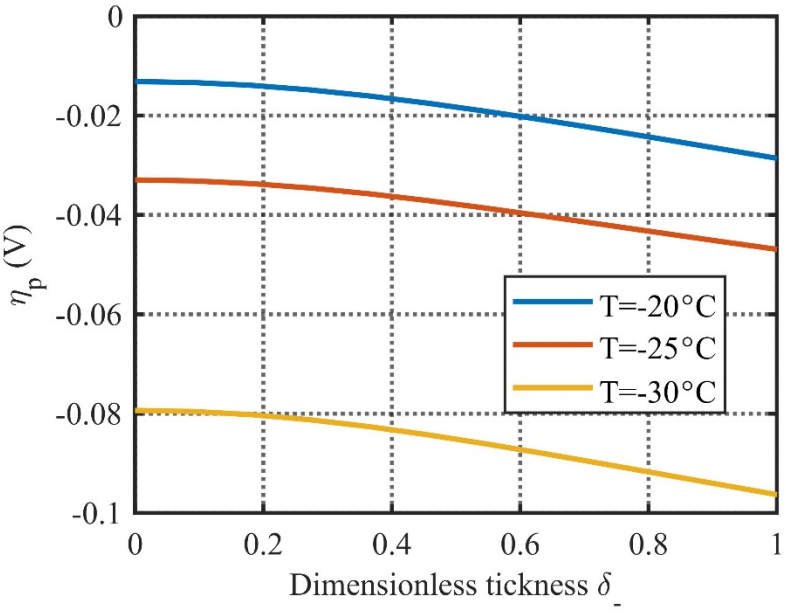

Fig. 50 Distribution of overpotential of lithium plating at -20/-25/30°C

The corresponding distribution of absolute reaction rate of lithium plating along the direction of anode thickness as a function of operating temperature is plotted in Fig. 51. The analysis implies that the reaction rate of lithium plating increases as the decrease of temperatures. In addition, the reaction rate of lithium plating near the separator side is larger due to the relative higher lithium ion concentration, which is consistent with the analyses of overpotentials.

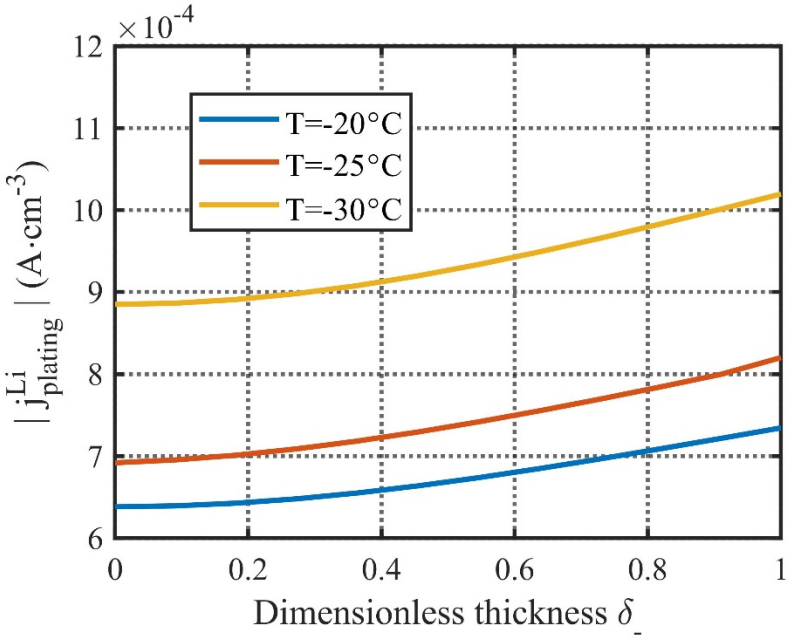

Fig. 51 Distribution of lithium deposition reaction rate at -20/-25/30°C

With the exception for the low operating temperature, high charging C-rate is another favorable factor to elicit lithium plating. The comparison of terminal voltage at CC-CV charging with various applied current rates (1/10C-rate, 1/4C-rate, 1/3C-rate and 1/2C-rate, respectively) at the operating temperature of -20°C between experiments and simulations is plotted in Fig. 52. The simulated evolution of terminal voltage in terms of the charging time has a reasonable match with the experimental one, which demonstrates the great predictive capability of electrochemical performance of LiBs by the model.

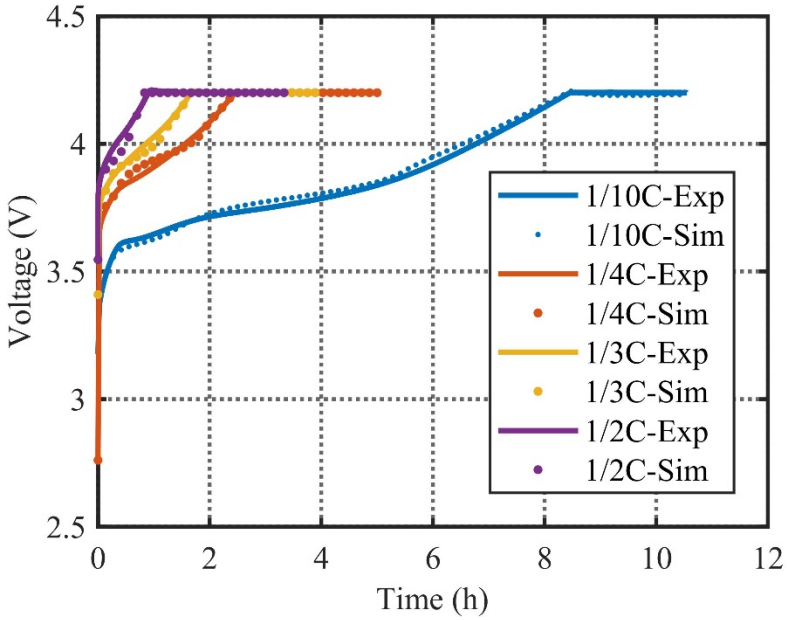

Fig. 52 Comparison of charge behaviors between experimental data and simulation results at different charging C-rates (1/10C, 1/4C, 1/3C and 1/2C, respectively) at -20°C

To extrapolate the influence of charging C-rates, the distributions of overpotential and reaction rate of lithium plating along the anode thickness direction are presented in Fig. 53 and Fig. 54, respectively. On one hand, the potential drop is enlarged as the increase of applied charging current. According to the potential governed criteria of lithium plating, no lithium deposition reaction occurs when the current of 1/10C-rate is applied to charge the cell, because the overpotential induced is positive. On the other hand, the lithium deposition reaction rate is zero when charged by 1/10C-rate current, which satisfies the conclusion that made by the analysis of overpotential evolution. In general, the high charging current is beneficial to prompt the lithium plating due to the correspondingly large potential drop that governed by the BV equation.

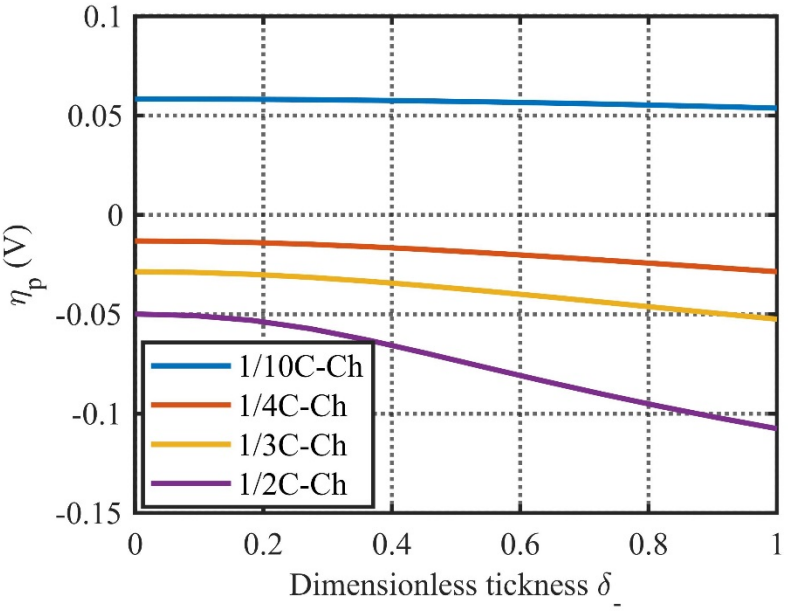

Fig. 53 Distribution of overpotential of lithium plating when charged at 1/10C, 1/4C, 1/3C and 1/2C, respectively

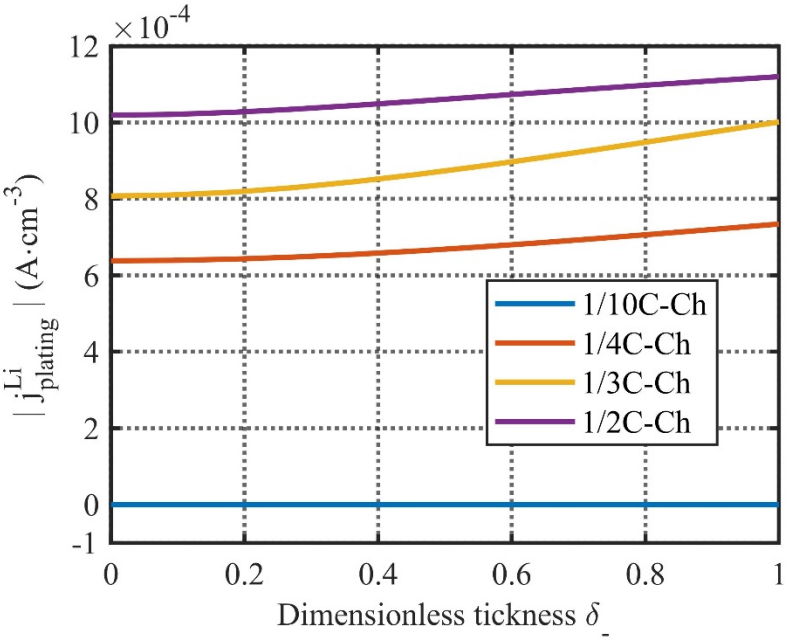

Fig. 54 Distribution of lithium deposition reaction rate when charged at 1/10C, 1/4C, 1/3C and 1/2C, respectively.

4.4.1.2 Mass transfer limitation

Another criterion of lithium plating corresponds to the mass transfer of lithium ions. At low temperatures, the diffusion of lithium ions in carbon particles is slowed down, leading to the accumulation of lithium ions at the interface between carbon particles and electrolyte during charging. When the surface concentration of lithium ions in carbon particles reaches or even exceeds the maximum value that the active material of the particles can maintain, the lithium plating is prompted. Fig. 55 displays the distribution of surface concentration of lithium ions across the anode when charged at various C-rates (1/2C-rate, 1/3C-rate and 1/4C-rate, respectively) and operating temperatures (-20/-25/-30°C). The maximum concentration that carbon particle can hold is plotted by a black dashed line. The surface concentration of lithium ions in solid phase increases as the increase of charging C-rates and temperatures. Other than charging the cell by 1/2C-rate applied current at -20°C (purple line), the surface concentration of anode particle is much smaller than the maximum value of the saturated one. Even though the gap between the surface and maximum concentration of lithium ions in anode cannot justify the existence of lithium plating, the distributions of overpotential presented in Fig. 50 and Fig. 53 give a robust support. In order to obtain the distribution of surface concentration under the excluded charging condition more clearly, the performance in the region near the separator where the lithium plating is originated due to the oversaturated surface concentration is zoomed in.

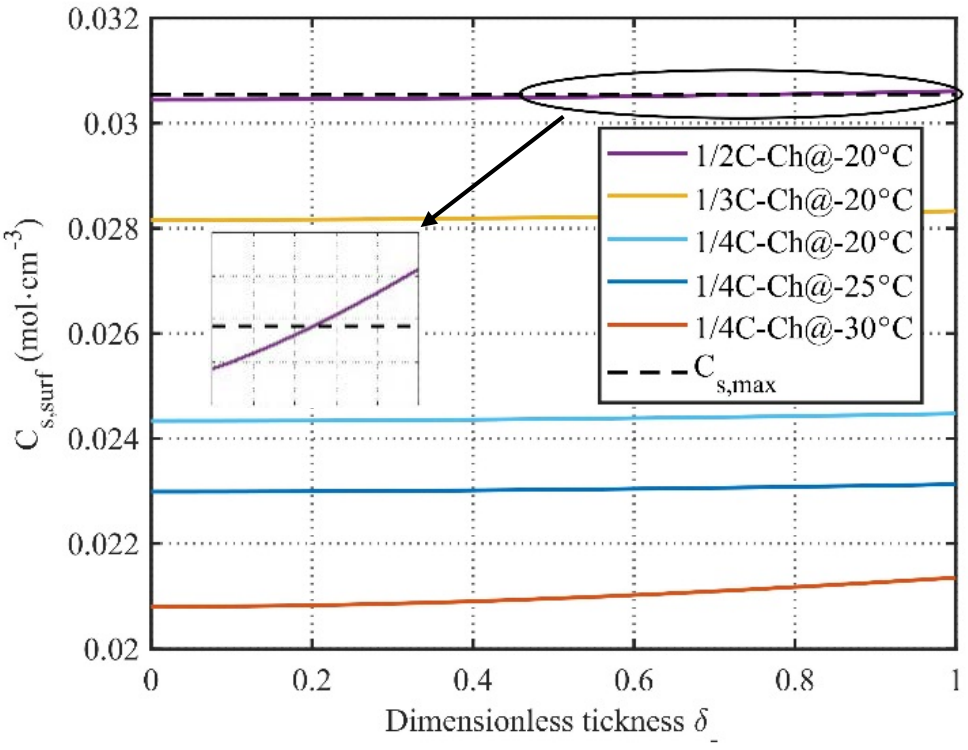

Fig. 55 Distribution of surface concentration of anode particles at different temperatures and charging C-rates

To better understand the mass transfer behaviors over the entire CC-CV charging process, the distribution of surface concentration over time at three different locations of the anode is shown in Fig. 56. The variation of terminal voltage is also plotted as a reference. The increasing rate of surface concentration at each location approaches its maximum at the end of CC charging, then turns over to drop gradually at CV charging. The concentration near the separator is larger than that at the other locations.

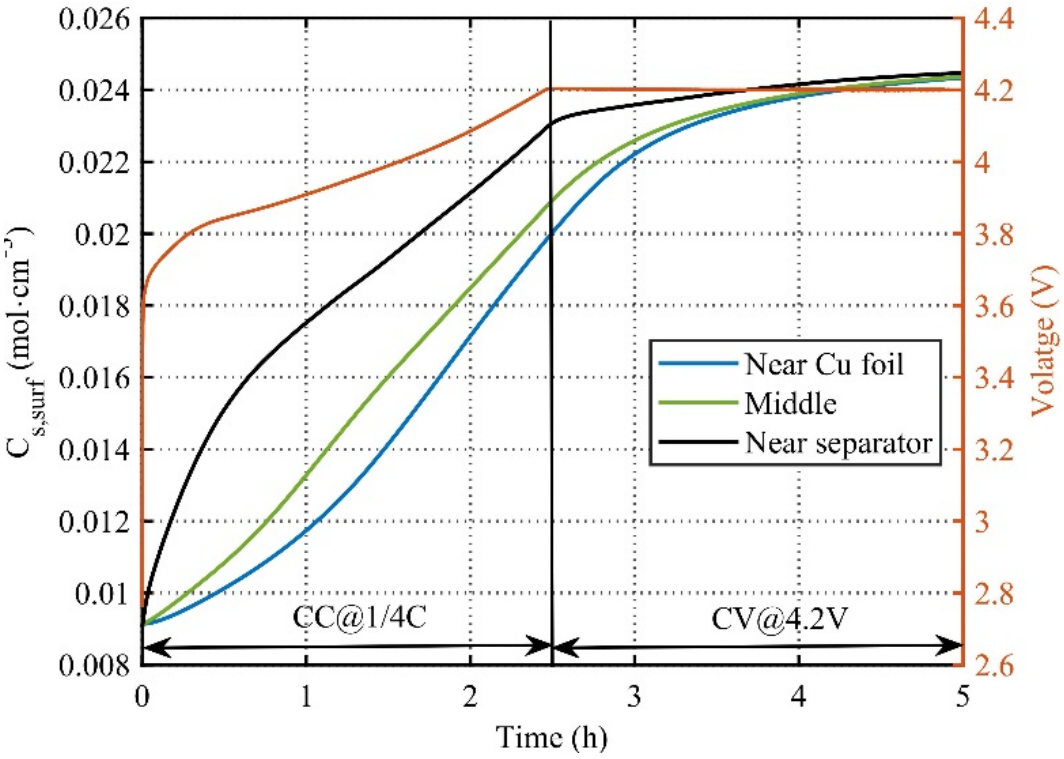

Fig. 56 Distribution of surface concentration of anode particles at various locations as a function of charging time at -20°C

Considering both CTL and MTL simultaneously, lithium plating is prone to take place at the interface between anode and separator due to both the higher overpotential and surface concentration of lithium ions. Additionally, compared the effects of overpotential and surface concentration under various operating conditions in terms of the temporal and spatial evolutions over CC-CV charging process, charge transfer limitation is a more severe cause for lithium plating.

4.4.2 Analysis of lithium stripping under discharging

A schematic diagram of the internal cell characteristics in the anode at the beginning of discharge is displayed in Fig. 57. When discharge the LiB after charging at low temperatures, extra

lithium ions coming from lithium stripping can be released on anode besides de-intercalation at the beginning. The output delivering current moving to the cathode includes that of both classical de-intercalation and lithium stripping. The extra voltage plateau represents the existence of lithium stripping and the width of the plateau is proportional to the amount of stripped lithium ions. Both single cycle and multiple cycle tests are performed to validate the developed electrochemical model.

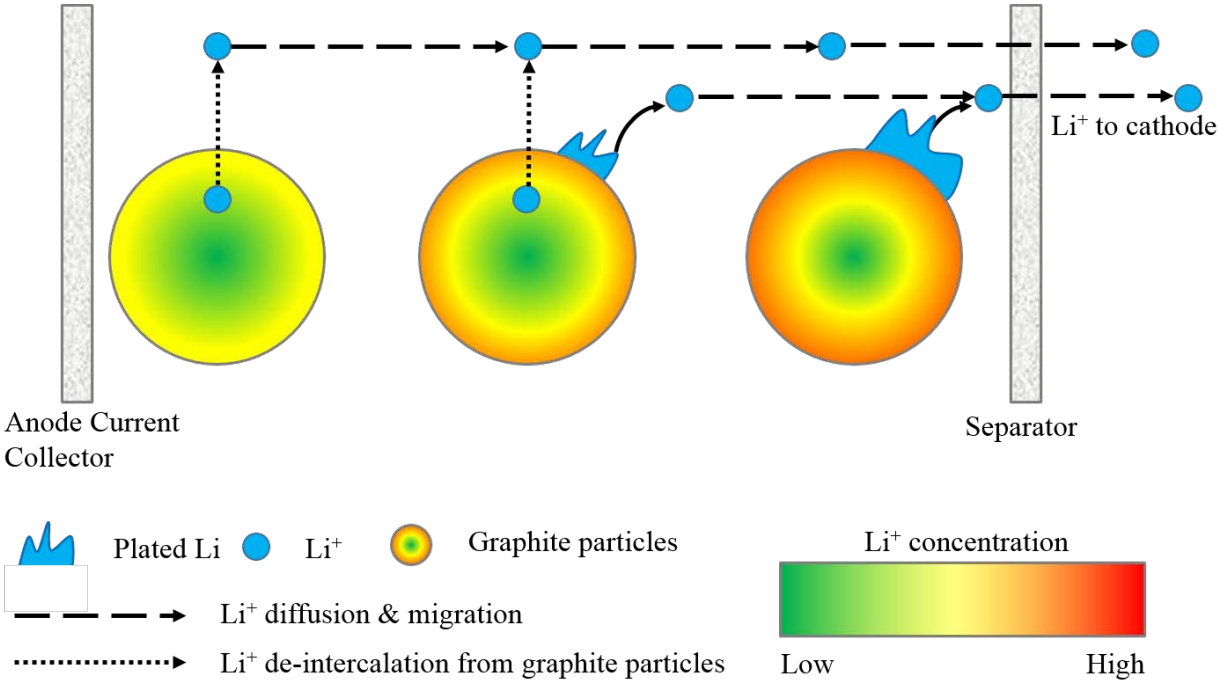

Fig. 57 Schematic diagram of internal cell characteristics in the anode at the beginning of discharge.

4.4.2.1 Single cycle

Fig. 58 shows the discharging voltage profiles at 3 different C-rates (1/10C, 1/4C and 1/3C) immediately after charging the cell to 100% SOC at the temperature of -20°C. The experiments

and simulations are plotted by solid lines and markers, respectively. The inset provides an enlarged view of the voltage profiles at the beginning of discharging in order to observe the voltage plateaus more clearly. The simulation results can well capture the experimental measurements of discharging voltage. In agreement with literatures, the voltage plateaus can be observed at the early stage of discharging at 1/4C and 1/3C, which relate to the peaks of the differential voltage profiles (dV/dQ) in Fig. 59. The characteristics of the peaks of dV/dQ is well estimated by the model with negligible discrepancies. The location where dV/dQ peak appears represents the end of lithium stripping. The discharge capacity at the dV/dQ peak equals to the total amount of the reversed capacity due to lithium stripping and the classical discharging capacity, which can be calculated by the integration of lithium dissolution reaction rate and main reaction rate over the electrode area and time, respectively. The reversed capacities of the cells with 1/4C and 1/3C discharging current applied are 2.18Ah and 2.72Ah, respectively. As the increase of discharging C-rates, more lithium ions can be released so that more capacity can be reversed.

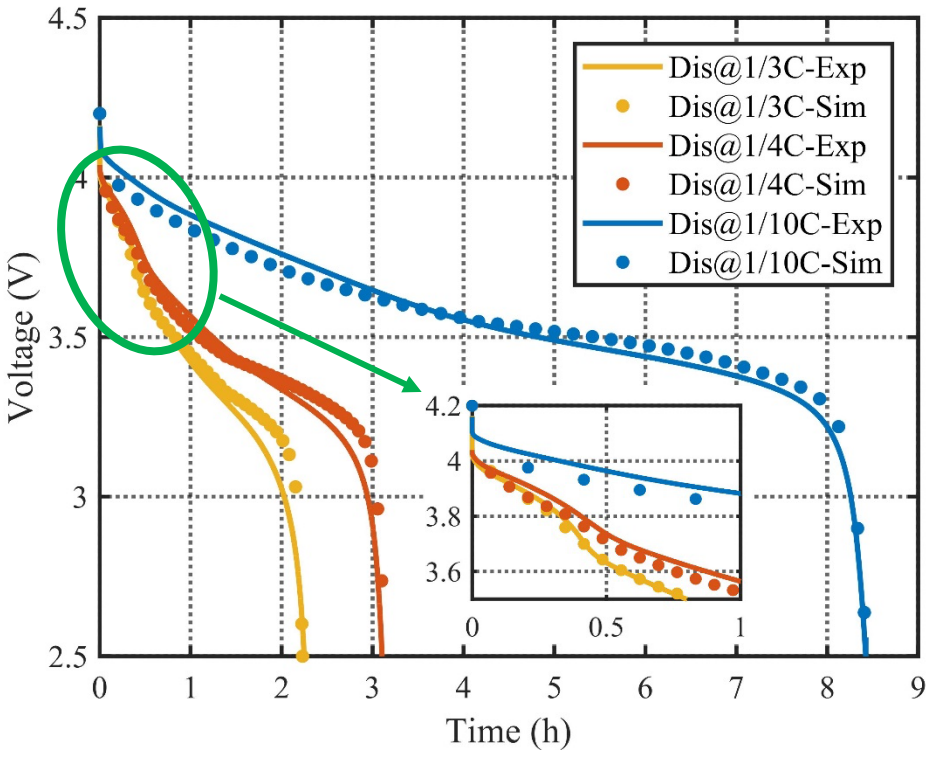

Fig. 58 Comparison of discharge behaviors between experimental data and simulation results at different discharging C-rates (1/10C, 1/4C and 1/3C, respectively) at -20°C

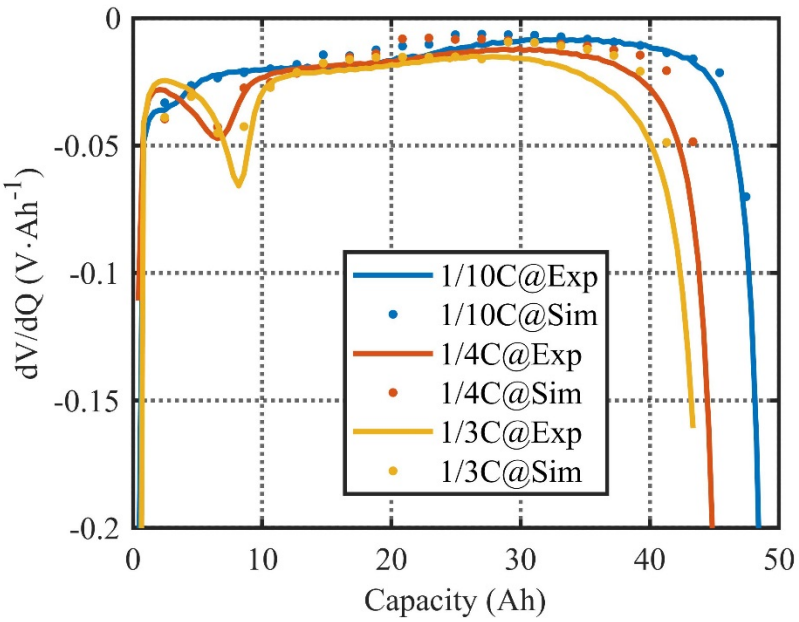

Fig. 59 Differential voltage analysis of the cells with different discharging C-rates (1/10C, 1/4C and 1/3C, respectively) applied at -20°C

Fig. 60 displays the comparison of discharging voltage profiles between experiments and simulations at different temperatures (-20/-25/-30°C), while its corresponding differential voltage analyses are shown in Fig. 61. The number of ions released by lithium stripping estimated by the developed model is proportional to the width of the extra voltage plateau at the beginning of discharging, which is approximate 2.18Ah, 3.14Ah and 4.31Ah for the cell discharged at -20°C, -25°C and -30°C, respectively. The lithium stripping is accelerated as the decrease of temperature.

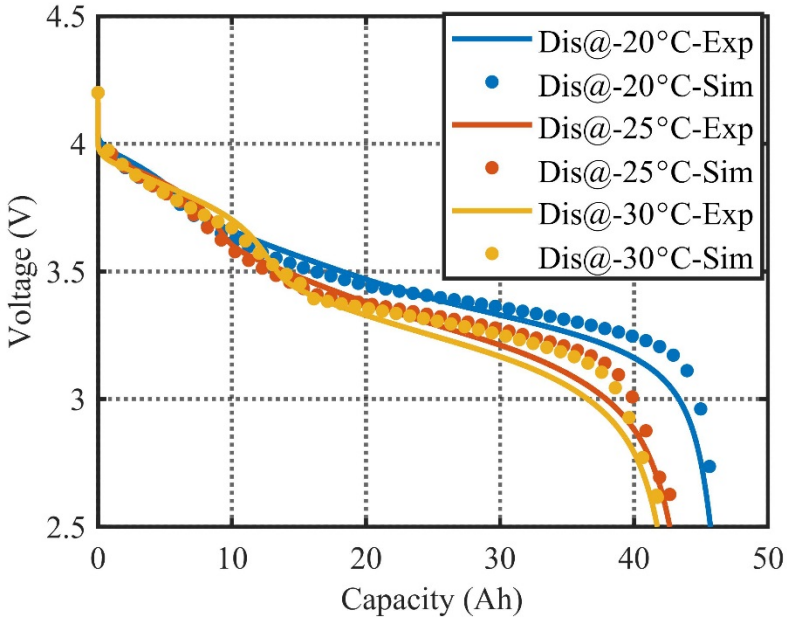

Fig. 60 Comparison of discharging voltage profiles between experiments and simulations at different temperatures

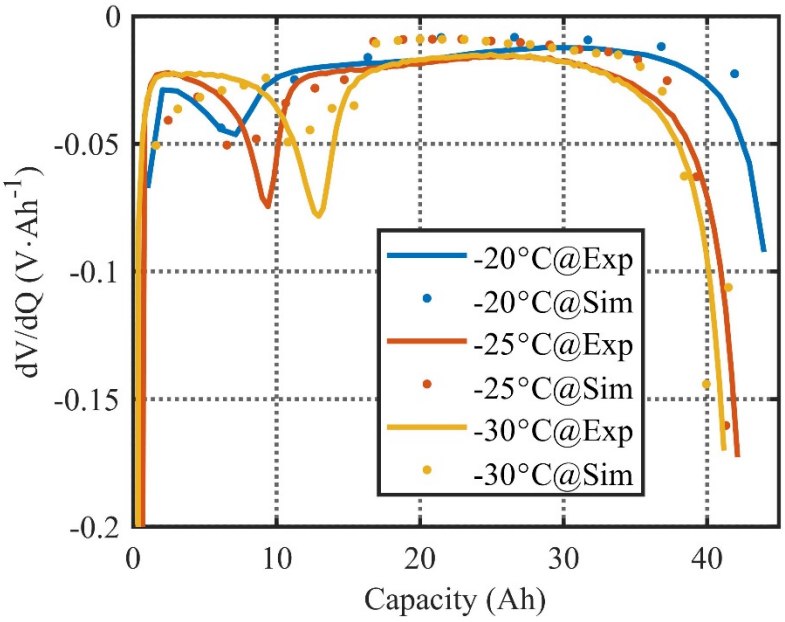

Fig. 61 Differential voltage analysis of the cells discharged at different temperatures

4.4.2.2 Multiple cycle

The top subplot of Fig. 62 plots the applied current profiles in the multiple cycle tests at different temperatures. The blue and orange solid lines represent the current profiles at the temperature of -20°C and -30°C, respectively. The middle and bottom subplots of Fig. 62 compare the terminal voltage between experimental measurements and simulation results at -20°C and -30°C, respectively. Both lithium plating and lithium stripping are considered in the validation of multiple cycle tests, and the modeling results have a great match with the experiments, which manifests the great capability of the model to predict the dynamic responses.

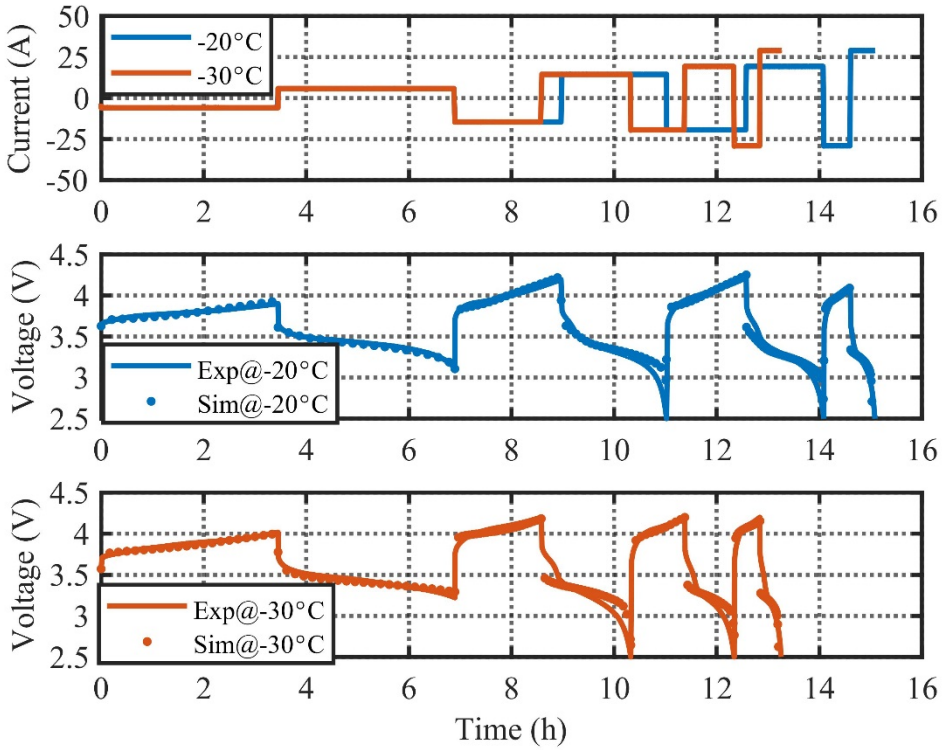

Fig. 62 Comparison of terminal voltage between experiments and simulations for multiple cycle tests at -20°C and -30°C.

4.4.3 Characteristics of lithium plating/stripping over cycling

The degradation effects of LiBs after extended cycling at low temperatures are inextricably linked to the lithium plating, including loss of recyclable lithium ions, loss of AM, growth of plated lithium and secondary SEI, growth of DL and the consumption of electrolyte solvents. The detailed analyses of the degradation related parameters and validation of the degradation model incorporating lithium plating/stripping are presented in section 4.4.3.1 and 4.4.3.2, respectively.

4.4.3.1 Analysis of degradation related parameters

To analyze the variation of the degradation related parameters inside the LiB over prolonged cycles, simulation results of lithium deposition reaction rate and other related parameters are investigated at -20°C. The distribution of lithium deposition reaction rate along the direction of anode thickness as a function of cycle number is depicted in Fig. 63. With the increase of cycle number, the lithium deposition reaction rate is accumulated at interface between carbon particles and electrolyte as the arrow indicates direction. In addition, the lithium deposition reaction rate is higher at the anode/separator interface. Correspondingly, the variations of other physical degradation parameters are plotted from Fig. 64 to Fig. 66.

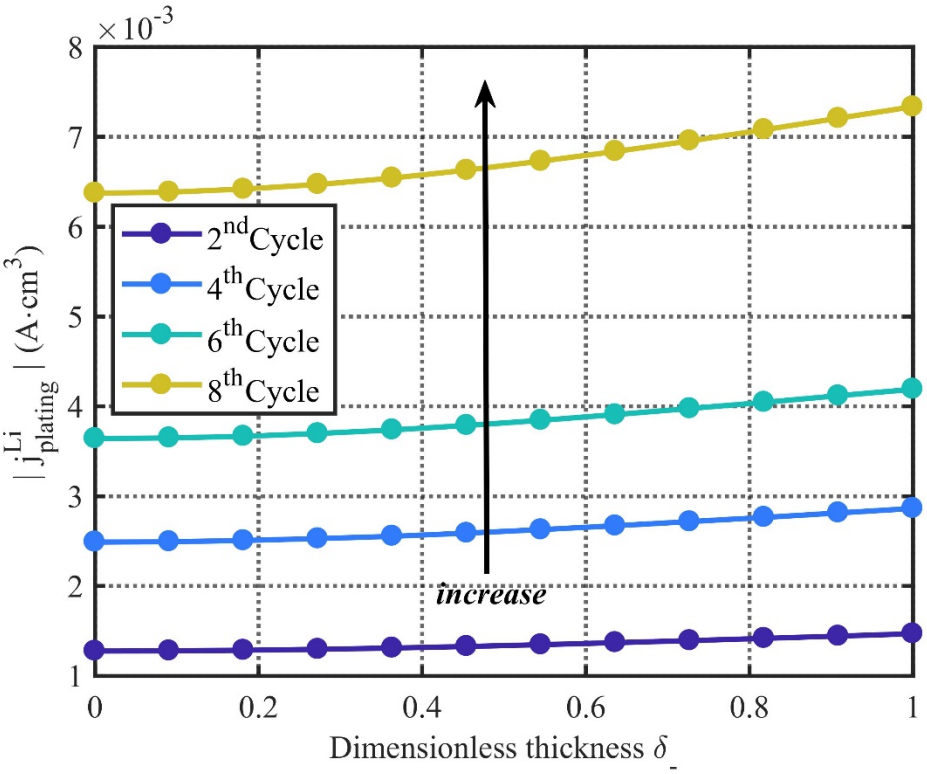

Fig. 63 Analysis of lithium deposition reaction rate along the direction of anode thickness as a function of cycle number

Since the capacity fade is mainly caused by ion loss and AM loss, the comparisons of capacity fade between experiments and simulations are presented in Fig. 64. Due to the continuous consumption of recyclable lithium ions as reactants in the reaction of lithium plating, the amount of ion loss (q_{total}^{Li}) is increased as the number of cycles increased, as shown in the blue shade. The amount of AM loss (yellow shade) increases with the increasing cycle number is calculated based on the reduced accessible area of particle surface. The total amount of ion loss and AM loss is compared with the actual capacity fade (green shade) measured by the experiments, which shows a great match.

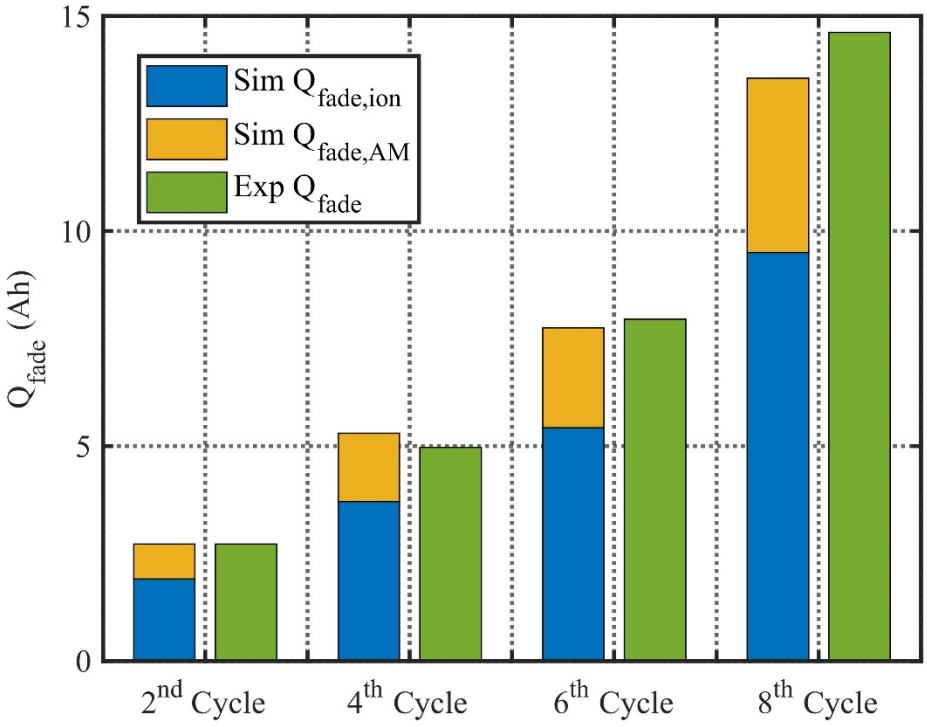

Fig. 64 Analysis of degradation parameters: Ion loss & AM loss

The variations of resistance of plated lithium ($R_{plating}$) and electrode volume fraction (ε_s) in terms of cycle number across the anode, which are related to the growth of plated lithium and loss of AM, are plotted in Fig. 65.

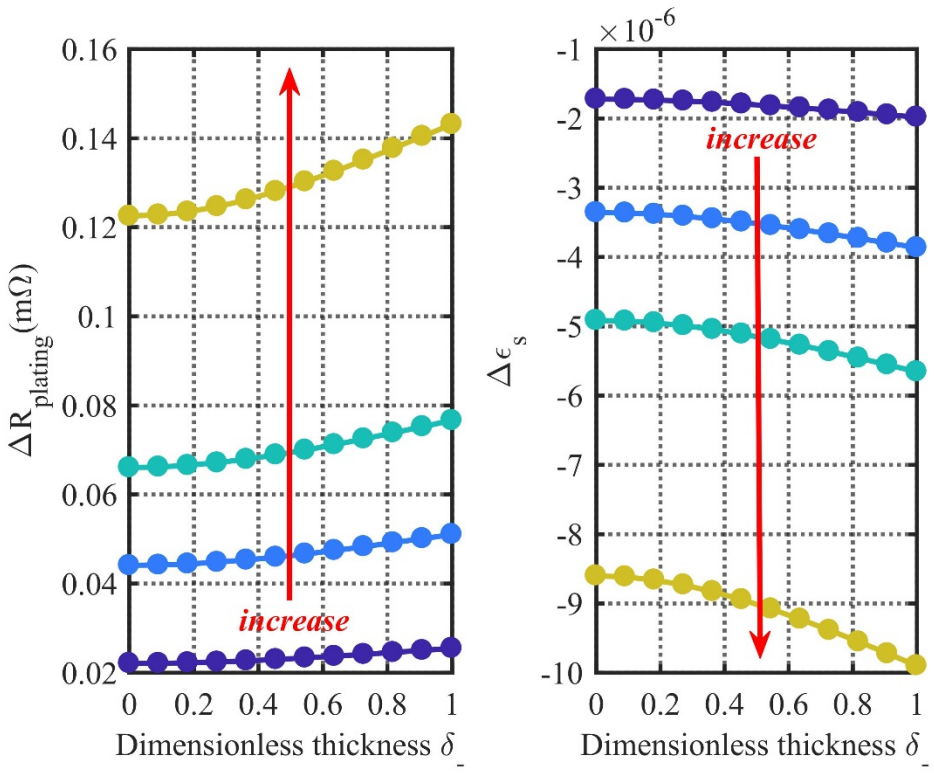

Fig. 65 Analysis of degradation parameters: Variation of resistance of plated lithium and volume fraction of anode.

As the reactants of the chemical reaction described in Eq. (43) and (44), electrolyte solvents are consumed continuously, which leads to the decrease of electrolyte volume fraction (ε_e), as shown in the upper subplot of Fig. 66. The lower subplot shows the increase of resistance of DL due to the growth of DL. The analyses of the degradation effects of lithium plating based on the variation of the electrochemical parameters can be summarized in Table 11.

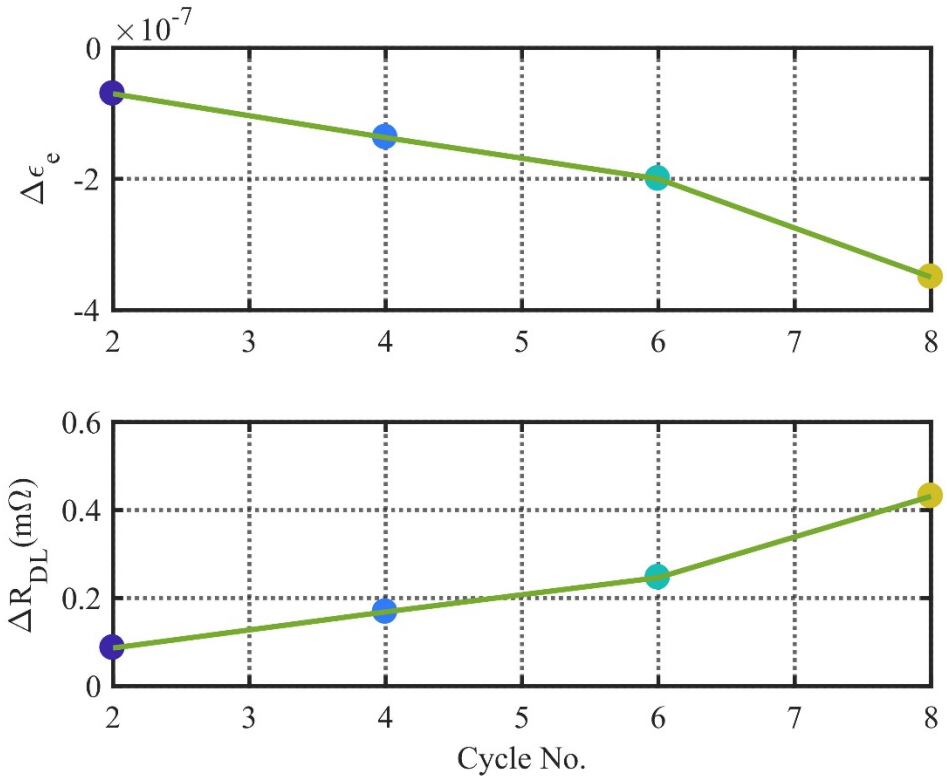

Fig. 66 Analysis of degradation parameters: Variation of volume fraction of electrolyte and resistance of DL

Table 11 Degradation effects and parameters of lithium deposition reaction

Causes	Effects	Degradation parameters	Consequences
Reaction rate of lithium plating $\left\|j_{plating}^{Li}\right\|\uparrow$	Ion loss	$q_{total}^{Li}(t)\uparrow$	Capacity fade
	AM loss	Electrode volume fraction $\varepsilon_s\downarrow$	Capacity fade
	Plated Li growth	Resistance of plated lithium $R_{plating}\uparrow$	Impedance rise
	DL growth	Resistance of DL $R_{DL}\uparrow$	Impedance rise
	Electrolyte consumption	Electrolyte volume fraction $\varepsilon_e\downarrow$	Impedance rise

4.4.3.2 Model validation of EoL

According to the analyses of overpotential and concentration in terms of temporal and spatial distribution, both the temperatures and charging C-rates have profound impacts on the lithium plating, while the temperatures and discharging C-rates have influences on the lithium stripping. To explore the effects on the prolonged cycles, both lithium plating and lithium stripping are taken into account. The comparisons of discharge terminal voltage between simulation results obtained using the physics-based degradation model and experimental measurements at various operating conditions for the cells performed single cycling are plotted from Fig. 67 to Fig. 70, while those for the cells performed multiple cycling tests are plotted in Fig. 71 and Fig. 72. The solid lines and markers represent the experiments and simulations, respectively.

The influences of charging C-rates on the long-term cycling tests are discussed between Fig. 67 and Fig. 68. The SOH of the LiBs decays faster at relatively higher charging currents (1/3C-rate). Furthermore, the effects of temperatures on degradation are summarized in Fig. 69 and Fig. 70. The dynamic responses of multiple cycles over prolonged cycling at -20°C and -30°C are discussed in Fig. 71 and Fig. 72, respectively. Besides the validation of the 6^{th} cycle at -30°C in Fig. 70, the other validations greatly capture the experiments. For the excepted case, the capacity fade is about 43.9%. Usually, the EV battery is considered as EoL when its capacity drops below 80% of its nominal capacity, or 70% at the worst case. When the battery continues to get further aged, not only lithium plating/stripping from the aspect of electrochemistry, but also mechanical failure needs to be considered. In this dissertation, the ignorance of mechanical failure makes the model not to be capable of predicting the electrochemical performance when the capacity fade of the cell reaches 43.9%.

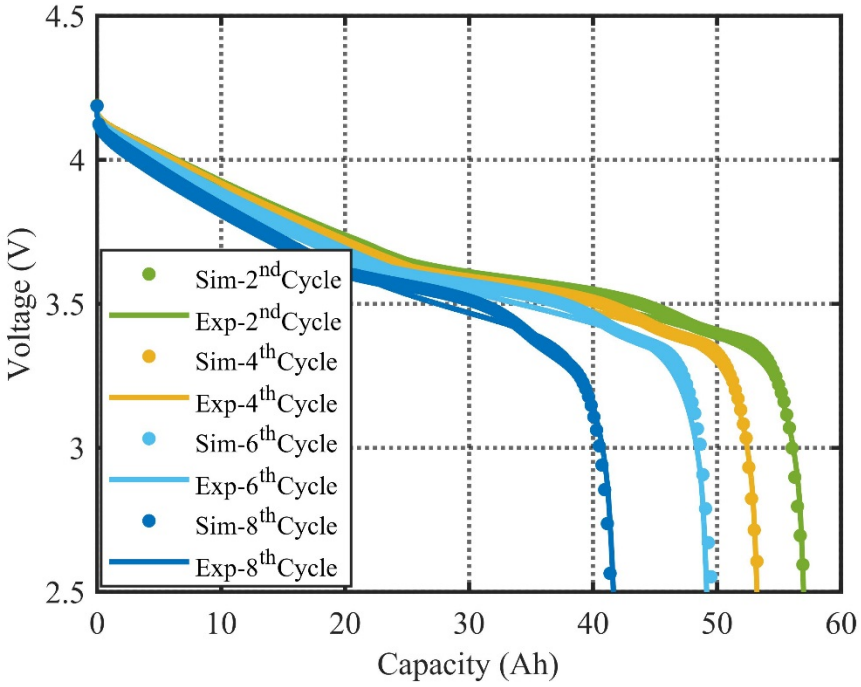

Fig. 67 Comparison of discharge behaviors of the cell cycled using 1/3C-rate charging/discharging current at -20ºC

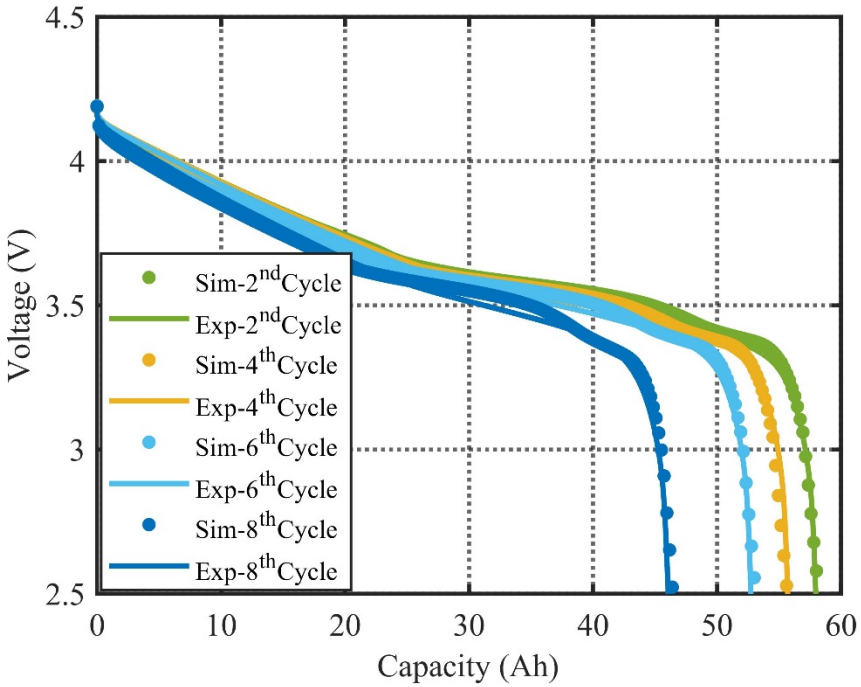

Fig. 68 Comparison of discharge behaviors of the cell cycled using 1/4C-rate charging/discharging current at -20ºC

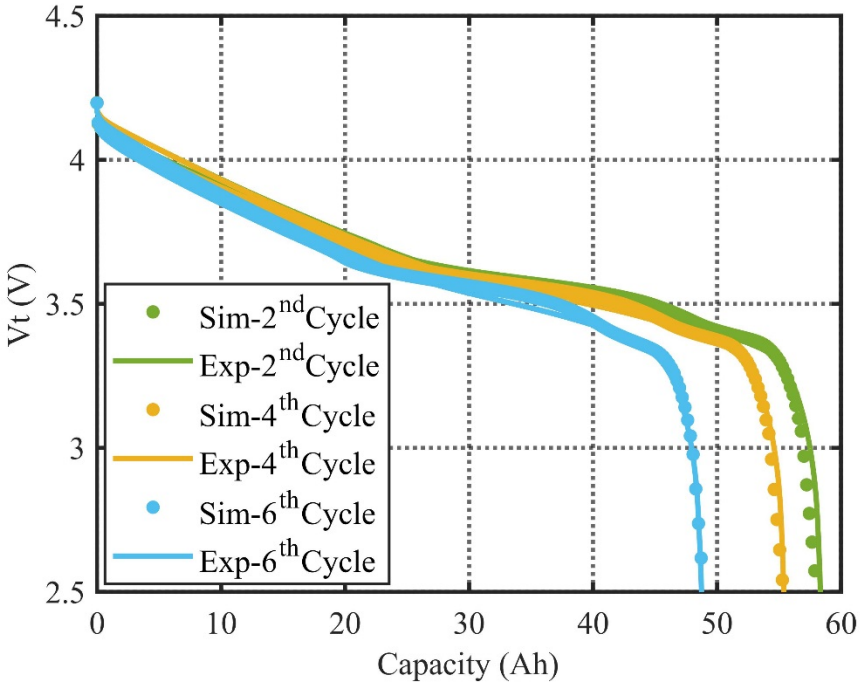

Fig. 69 Comparison of discharge behaviors of the cell cycled using 1/4C-rate charging/discharging current at -25ºC

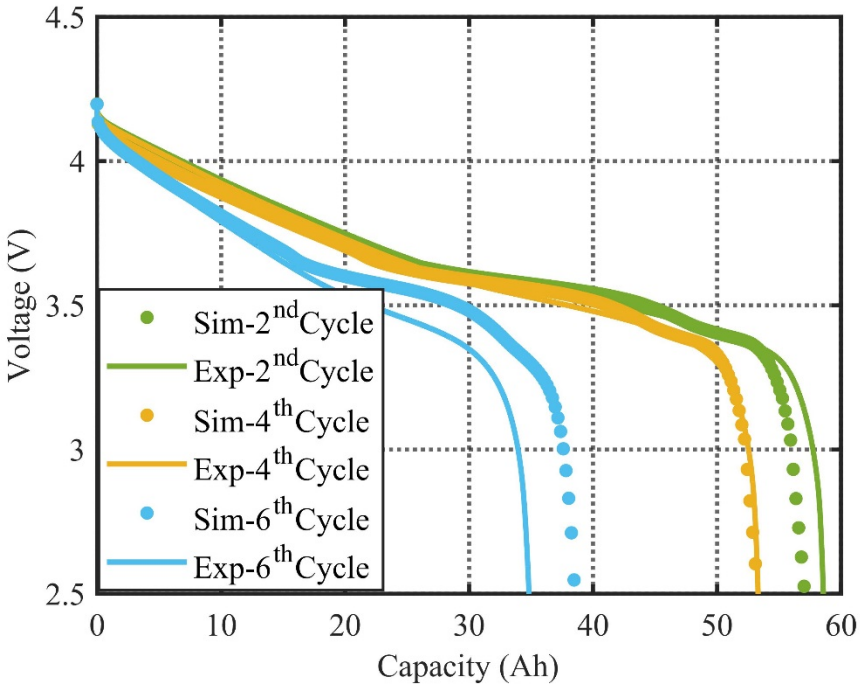

Fig. 70 Comparison of discharge behaviors of the cell cycled using 1/3C-rate charging/discharging current at -30ºC

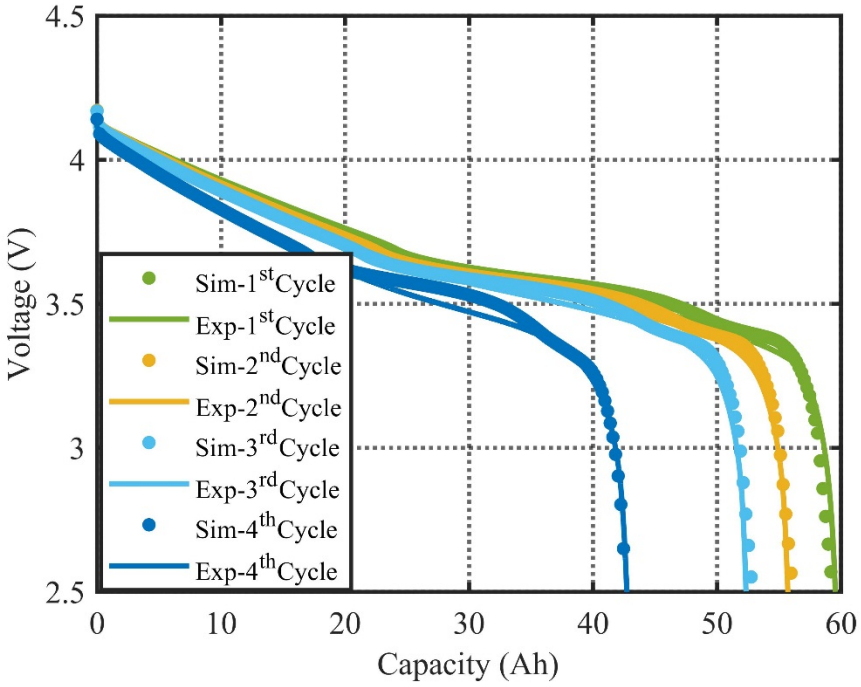

Fig. 71 Comparison of discharge behaviors of the multiple cycled cell at -20ºC

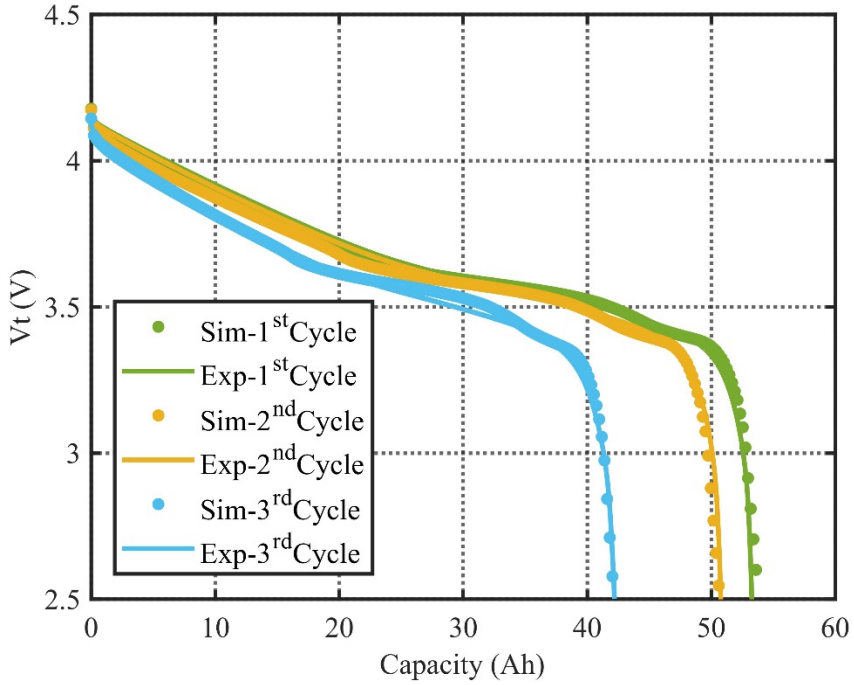

Fig. 72 Comparison of discharge behaviors of the multiple cycled cell at -30ºC

Capacity fade is one of the most significant criteria to evaluate performance of degraded LiBs. The comparisons of simulated capacity and the Ah-based measured capacity as the function of cycle number at various charging C-rates and temperatures are shown in the upper subplot of Fig. 73. The markers, circles and crosses, denote the measurements and simulations, respectively. Furthermore, the corresponding error between measurements and simulation results is plotted in the lower subplot. In order to display the capacity variations comparably, the SOH in terms of capacity and the corresponding estimation error are calculated by Eq.(30) and Eq.(31), respectively. With the exception of a relatively large deviation of the last capacity estimation at -30°C, other deviation of simulations over experiments is less than 3%.

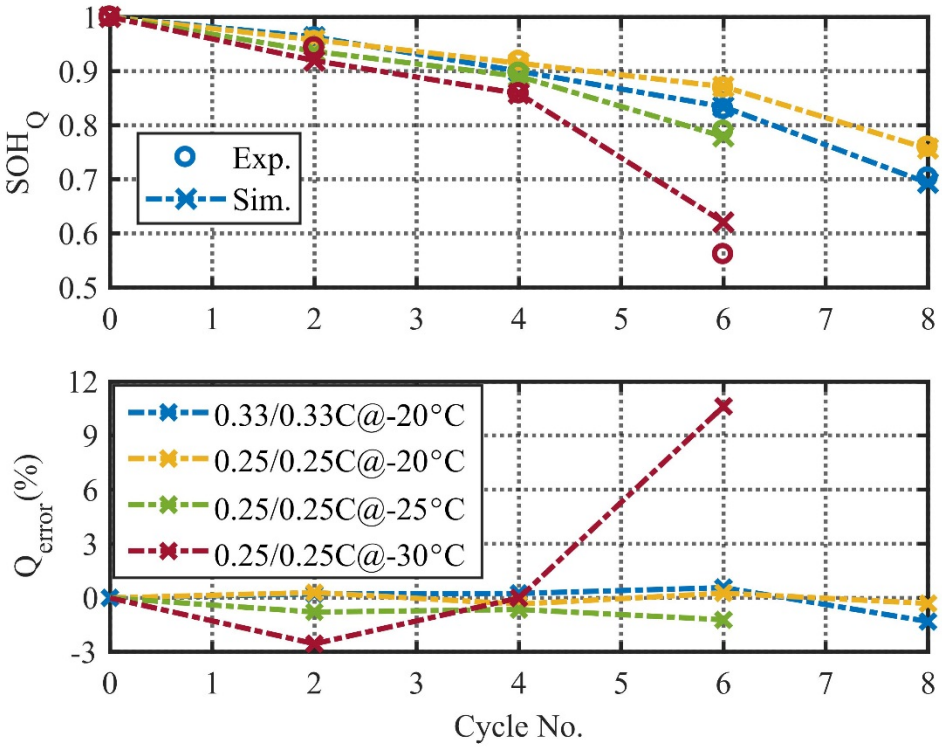

Fig. 73 Comparison between Ah-based measured capacity and simulated capacity at various charging C-rates (1/3C-rate, 1/4C-rate) and temperatures (-20/-25/-30°C).

The comparisons of capacity between simulations and experiments for the multiple cycling tests are plotted in Fig. 74. The error of capacity for multiple cycling tests is within 1.5% when the capacity fade is less than 30%.

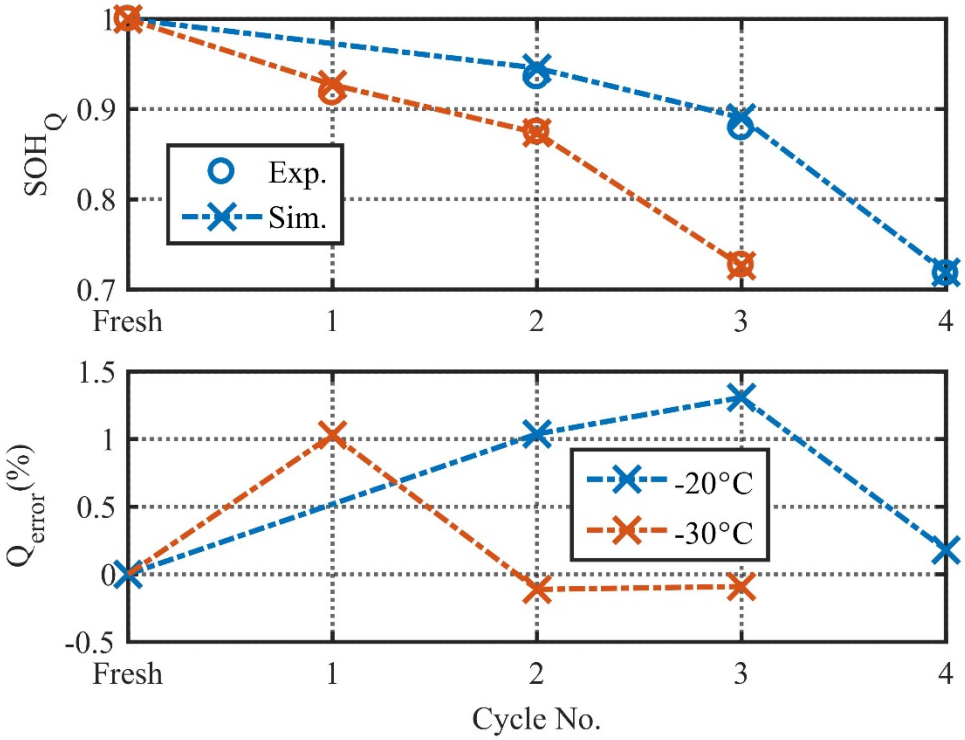

Fig. 74 Comparison between Ah-based measured capacity and simulated capacity for multiple cycling tests at -20 and -30°C.

4.5 Summary

Understanding the degradation mechanism and behaviors accounting for lithium plating/stripping is of great importance to assure the safe and durable use of LiBs at low temperatures. A physics-based electrochemical-thermal model is developed and validated to predict the aging characteristics of LiBs. The model is applied to explore the behaviors of

NMC/Carbon cells undergoing prolonged cycling, whose degradation can be accelerated by the lower operating temperatures and higher charging current rates.

The occurrence of lithium plating is limited by both charge and mass transfer processes, which correspond to the analyses of potentials and concentrations, respectively. The lithium plating starts to occur when the overpotential becomes negative or the surface Li^+ concentration in the solid phase exceeds the saturated Li^+ concentration of the carbon particles. Compare the effects of potential and concentration governed criteria, charge transfer limitation has more impacts on lithium plating, which implies that the lithium plating prefers starting from the anode/separator interface due to the higher potential gradient and Li^+ concentration.

The existence of lithium stripping is represented by an extra voltage plateau at the beginning of discharging. The amount of stripped lithium ions is proportional to the width of the extra voltage plateau. The differential voltage analysis is used to calculate the reversed capacity due to lithium stripping by the integration of lithium dissolution reaction rate over time and electrode area. With the increase of discharging current rates, more lithium ions can be stripped from the plated lithium. Lithium stripping is also accelerated by the decreasing temperature because larger amount of lithium ions are inclined to form plated lithium.

The model manifests the degradation effects of lithium plating/stripping, including loss of lithium inventory, loss of anode active material, growth of plated lithium, secondary SEI and DL, and consumption of electrolyte solvents, which are aggravated as the cycling proceeds. Furthermore, the model is validated by the accelerated cycling tests and multiple cycle tests performed at various operating conditions, which match reasonably with experimental measurements with respect to the terminal voltage and capacity retention. Despite the capacity drops below 70% of its nominal capacity, the error of the capacity estimation is within 3%.

Chapter 5. Conclusion and future work

An integrated ROM considering degradation effects at both high and low temperatures is proposed and validated against experiments for both fresh and cycled LiBs. The ion behaviors, including migration, diffusion and electrochemical kinetics, are described by the coupled PDEs. The special characteristics of LFP particles, two-phase transition and path dependence, are modeled using a shrinking core with a moving interface between a lithium-rich and a lithium-deficient phase. To further minimize the errors, a hybridized algorithm combining classical Coulomb counting method and EKF is incorporated into the developed ROM, especially for the SOC estimation. The average error of SOC and voltage estimation is kept within 5% and 2%, respectively.

Degradation causes and effects differ as the variation of operating temperature. At high temperatures, side reaction is regarded as the predominant cause of degradation, which can be accelerated by elevated temperatures, high SOC levels and large SOC cycling limits. The integrated model facilitates to represent the degradation effects, including loss of recyclable lithium ions, loss of AM, growth of SEI and DL and consumption of electrolyte solvents. The model is capable of estimating capacity and power with an accuracy of 2% and 3% until 1000 cycles, respectively. At low temperatures, the effects of side reaction are diminished gradually, while those of lithium plating/stripping become dominant on degradation, especially at extremely low temperatures (<-20°C). At charging, the lithium ions are inclined to deposit on instead of

intercalating into the solid matrix of anode. The analyses of lithium plating are performed in terms of potential and concentration corresponding to the charge and mass transfer processes, respectively. Either negative overpotential or oversaturated Li^+ surface concentration implies the occurrence of lithium plating. The degradation effects of lithium plating are aggravated with the decreasing operating temperature and increasing charging C-rates. At discharging, the existence of lithium stripping is denoted by an extra voltage plateau at the beginning. The amount of reversed capacity due to lithium stripping is proportional to the width of extra voltage plateau, which can be calculated with the help of the differential voltage analyses. The location where the peak of dV/dQ appears corresponds to the total amount of releasable capacity due to lithium stripping and classical discharging. The increase of discharging C-rates leads to more capacity reversed and less capacity fade. The integrated model manifests the degradation effects of both lithium plating and lithium stripping, which well captures the experimental measurements of terminal voltage and capacity retention. Besides the capacity drops below 70% of its nominal capacity, the error of the capacity estimation is within 3%.

In the dissertation, the integrated physics-based degradation model is developed either for side reaction dominant temperatures or for lithium plating/stripping dominant temperatures. The analyses at temperature range where both side reaction and lithium plating/stripping need to be considered are very few. In the future work, the model needs to be improved to facilitate the in-depth investigations on the side reaction and lithium plating/stripping at the same time. Furthermore, other degradation effects, such as mechanical failure and cathode degradation need to be considered for the deep cycling of the LiBs. Taking the charging efficiency of LiBs at low temperatures into account, the design of a suitable fast charging algorithm considering lithium plating/stripping can also be a promising topic.

References

[1] N. Nitta, F. Wu, J.T. Lee, G. Yushin, Li-ion battery materials: Present and future, Mater. Today. 18 (2015) 252–264. doi:10.1016/j.mattod.2014.10.040.

[2] M. Safari, C. Delacourt, Modeling of a commercial graphite/$LiFePO_4$ Cell, J. Electrochem. Soc. 158 (2011) A562–A571. doi:10.1149/1.3567007.

[3] X. Li, M. Xiao, S.Y. Choe, W.T. Joe, Modeling and analysis of $LiFePO_4$/Carbon battery considering two-phase transition during galvanostatic charging/discharging, Electrochim. Acta. 155 (2015) 447–457. doi:10.1016/j.electacta.2014.12.034.

[4] M. Doyle, T.F. Fuller, J. Newmann, Modeling of galvanostatic charge and discharge of the Lithium/Polymer/Insertion cell, J. Electrochem. Soc. 140 (1993) 1526–1532. doi:10.1149/1.2221597.

[5] V. Srinivasan, J. Newman, Discharge model for the lithium iron-phosphate electrode, J. Electrochem. Soc. 151 (2004) A1517–A1529. doi:10.1149/1.1785012.

[6] C. Wang, U.S. Kasavajjula, P.E. Arce, A discharge model for phase transformation electrodes: formulation, experimental validation, and analysis, J. Phys. Chem. C. 111 (2007) 16656–16663. doi:10.1021/jp074490u.

[7] U.S. Kasavajjula, C. Wang, P.E. Arce, Discharge model for $LiFePO_4$ accounting for the solid solution range, J. Electrochem. Soc. 155 (2008) A866–A874. doi:10.1149/1.2980420.

[8] A. Khandelwal, K.S. Hariharan, V. Senthil Kumar, P. Gambhire, S.M. Kolake, D. Oh, S. Doo, Generalized moving boundary model for charge-discharge of $LiFePO_4$/C cells, J.

Power Sources. 248 (2014) 101–114. doi:10.1016/j.jpowsour.2013.09.066.

[9] M. Safari, C. Delacourt, Mathematical modeling of lithium iron phosphate electrode: Galvanostatic charge/discharge and path dependence, J. Electrochem. Soc. 158 (2011) A63–A73. doi:10.1149/1.3515902.

[10] T.-S. Dao, C.P. Vyasarayani, J. McPhee, Simplification and order reduction of lithium-ion battery model based on porous-electrode theory, J. Power Sources. 198 (2012) 329–337. doi:10.1016/j.jpowsour.2011.09.034.

[11] N. Baba, H. Yoshida, M. Nagaoka, C. Okuda, S. Kawauchi, Numerical simulation of thermal behavior of lithium-ion secondary batteries using the enhanced single particle model, J. Power Sources. 252 (2014) 214–228. doi:10.1016/j.jpowsour.2013.11.111.

[12] K.A. Smith, C.D. Rahn, C.-Y. Wang, Model order reduction of 1D diffusion systems via residue grouping, J. Dyn. Syst. Meas. Control. 130 (2008) 011012-1-011012-8. doi:10.1115/1.2807068.

[13] V.R. Subramanian, V. Boovaragavan, V. Ramadesigan, M. Arabandi, Mathematical model reformulation for lithium-ion battery simulations: galvanostatic boundary conditions, J. Electrochem. Soc. 156 (2009) A260–A271. doi:10.1149/1.3065083.

[14] L. Cai, R.E. White, Reduction of model order based on proper orthogonal decomposition for lithium-ion battery simulations, J. Electrochem. Soc. 156 (2009) A154–A161. doi:10.1149/1.3049347.

[15] V.S. Kumar, Reduced order model for a lithium ion cell with uniform reaction rate approximation, J. Power Sources. 222 (2013) 426–441. doi:10.1016/jjpowsour.2012.09.013.

[16] G.L. Plett, Extended Kalman filtering for battery management systems of LiPB-based HEV battery packs - Part 1. Background, J. Power Sources. 134 (2004) 252–261.

doi:10.1016/j.jpowsour.2004.02.031.

[17] S. Santhanagopalan, R.E. White, State of charge estimation for electrical vehicle batteries, Proc. IEEE Int. Conf. Control Appl. (2008) 690–695. doi:10.1109/CCA.2008.4629656.

[18] A.J. Salkind, C. Fennie, P. Singh, T. Atwater, D.E. Reisner, Determination of state-of-charge and state-of-health of batteries by fuzzy logic methodology, J. Power Sources. 80 (1999) 293–300. doi:10.1016/S0378-7753(99)00079-8.

[19] M. Charkhgard, M. Farrokhi, State-of-charge estimation for lithium-ion batteries using neural networks and EKF, IEEE Trans. Ind. Electron. 57 (2010) 4178–4187. doi:10.1109/TIE.2010.2043035.

[20] S. Santhanagopalan, R.E. White, Online estimation of the state of charge of a lithium ion cell, J. Power Sources. 161 (2006) 1346–1355. doi:10.1016/j.jpowsour.2006.04.146.

[21] D. Di Domenico, A. Stefanopoulou, G. Fiengo, Lithium-ion battery state of charge and critical surface charge estimation using an electrochemical model-based Extended Kalman filter, J. Dyn. Syst. Meas. Control. 132 (2010) 061302. doi:10.1115/1.4002475.

[22] R. Klein, N.A. Chaturvedi, J. Christensen, J. Ahmed, R. Findeisen, A. Kojic, Electrochemical model based observer design for a lithium-ion battery, IEEE Trans. Control Syst. Technol. 21 (2013) 289–301. doi:10.1109/TCST.2011.2178604.

[23] K.D. Stetzel, L.L. Aldrich, M.S. Trimboli, G.L. Plett, Electrochemical state and internal variables estimation using a reduced-order physics-based model of a lithium-ion cell and an extended Kalman filter, J. Power Sources. 278 (2015) 490–505. doi:10.1016/j.jpowsour.2014.11.135.

[24] M. Kassem, J. Bernard, R. Revel, S. Pélissier, F. Duclaud, C. Delacourt, Calendar aging of a graphite/$LiFePO_4$ cell, J. Power Sources. 208 (2012) 296–305.

doi:10.1016/j.jpowsour.2012.02.068.

[25] R.P. Ramasamy, R.E. White, B.N. Popov, Calendar life performance of pouch lithium-ion cells, J. Power Sources. 141 (2005) 298–306. doi:10.1016/j.jpowsour.2004.09.024.

[26] M. Dubarry, V. Svoboda, R. Hwu, B. Yann Liaw, Incremental capacity analysis and close-to-equilibrium OCV measurements to quantify capacity fade in commercial rechargeable lithium batteries, Electrochem. Solid-State Lett. 9 (2006) A454–A457. doi:10.1149/1.2221767.

[27] J. Wang, P. Liu, J. Hicks-Garner, E. Sherman, S. Soukiazian, M. Verbrugge, H. Tataria, J. Musser, P. Finamore, Cycle-life model for graphite-$LiFePO_4$ cells, J. Power Sources. 196 (2011) 3942–3948. doi:10.1016/j.jpowsour.2010.11.134.

[28] H.-F. Jin, Z. Liu, Y.M. Teng, J. kui Gao, Y. Zhao, A comparison study of capacity degradation mechanism of $LiFePO_4$-based lithium ion cells, J. Power Sources. 189 (2009) 445–448. doi:10.1016/j.jpowsour.2008.12.124.

[29] J. Schmalstieg, S. Käbitz, M. Ecker, D.U. Sauer, A holistic aging model for $Li(NiMnCo)O_2$ based 18650 lithium-ion batteries, J. Power Sources. 257 (2014) 325–334. doi:10.1016/j.jpowsour.2014.02.012.

[30] P. Ramadass, B. Haran, P.M. Gomadam, R.E. White, B.N. Popov, Development of first principles capacity fade model for Li-ion cells, J. Electrochem. Soc. 151 (2004) A196–A203. doi:10.1149/1.1634273.

[31] S. Santhanagopalan, Q. Zhang, K. Kumaresan, R.E. White, Parameter estimation and life modeling of lithium-ion cells, J. Electrochem. Soc. 155 (2008) A345–A353. doi:10.1149/1.2839630.

[32] G. Sikha, B.N. Popov, R.E. White, Effect of porosity on the capacity fade of a lithium-ion

battery, J. Electrochem. Soc. 151 (2004) A1104–A1114. doi:10.1149/1.1759972.

[33] H.J. Ploehn, P. Ramadass, R.E. White, Solvent diffusion model for aging of lithium-ion battery cells, J. Electrochem. Soc. 151 (2004) A456–A462. doi:10.1149/1.1644601.

[34] Q. Zhang, R.E. White, Capacity fade analysis of a lithium ion cell, J. Power Sources. 179 (2008) 793–798. doi:10.1016/j.jpowsour.2008.01.028.

[35] Y. Zhang, C.-Y. Wang, X. Tang, Cycling degradation of an automotive $LiFePO_4$ lithium-ion battery, J. Power Sources. 196 (2011) 1513–1520. doi:10.1016/j.jpowsour.2010.08.070.

[36] J. Groot, M. Swierczynski, A.I. Stan, S.K. Kaer, On the complex ageing characteristics of high-power $LiFePO_4$/graphite battery cells cycled with high charge and discharge currents, J. Power Sources. 286 (2015) 475–487. doi:10.1016/j.jpowsour.2015.04.001.

[37] P. Verma, P. Maire, P. Novák, A review of the features and analyses of the solid electrolyte interphase in Li-ion batteries, Electrochim. Acta. 55 (2010) 6332–6341. doi:10.1016/j.electacta.2010.05.072.

[38] M. Safari, C. Delacourt, Aging of a commercial graphite/$LiFePO_4$ Cell, J. Electrochem. Soc. 158 (2011) A1123–A1135. doi:10.1149/1.3614529.

[39] J. Vetter, P. Novák, M.R. Wagner, C. Veit, K.C. Möller, J.O. Besenhard, M. Winter, M. Wohlfahrt-Mehrens, C. Vogler, A. Hammouche, Ageing mechanisms in lithium-ion batteries, J. Power Sources. 147 (2005) 269–281. doi:10.1016/j.jpowsour.2005.01.006.

[40] A. Barré, B. Deguilhem, S. Grolleau, M. Gérard, F. Suard, D. Riu, A review on lithium-ion battery ageing mechanisms and estimations for automotive applications, J. Power Sources. 241 (2013) 680–689. doi:10.1016/j.jpowsour.2013.05.040 Review.

[41] R. Fu, S.Y. Choe, V. Agubra, J. Fergus, Development of a physics-based degradation model for lithium ion polymer batteries considering side reactions, J. Power Sources. 278 (2015)

506–521. doi:10.1016/j.jpowsour.2014.12.059.

[42] K. Striebel, A. Guerfi, J. Shim, M. Armand, M. Gauthier, K. Zaghib, $LiFePO_4$/gel/natural graphite cells for the BATT program, J. Power Sources, 2003: pp. 951–954. doi:10.1016/S0378-7753(03)00295-7.

[43] K. Striebel, J. Shim, V. Srinivasan, J. Newman, Comparison of $LiFePO_4$ from different sources, J. Electrochem. Soc. 152 (2005) A664–A670. doi:10.1149/1.1862477.

[44] K. Amine, J. Liu, I. Belharouak, High-temperature storage and cycling of C-$LiFePO_4$/graphite Li-ion cells, Electrochem. Commun. 7 (2005) 669–673. doi:10.1016/j.elecom.2005.04.018.

[45] K. Zaghib, N. Ravet, M. Gauthier, F. Gendron, A. Mauger, J.B. Goodenough, C.M. Julien, Optimized electrochemical performance of $LiFePO_4$ at 60^0C with purity controlled by SQUID magnetometry, J. Power Sources. 163 (2006) 560–566. doi:10.1016/j.jpowsour.2006.09.030.

[46] P. Liu, J. Wang, J. Hicks-Garner, E. Sherman, S. Soukiazian, M. Verbrugge, H. Tataria, J. Musser, P. Finamore, Aging mechanisms of $LiFePO_4$ batteries deduced by electrochemical and structural analyses, J. Electrochem. Soc. 157 (2010) A499–A507. doi:10.1149/1.3294790.

[47] H. Ekstrom, G. Lindbergh, A model for predicting capacity fade due to SEI formation in a commercial graphite/$LiFePO_4$ cell, J. Electrochem. Soc. 162 (2015) A1003–A1007. doi:10.1149/2.0641506jes.

[48] G. Ning, B. Haran, B.N. Popov, Capacity fade study of lithium-ion batteries cycled at high discharge rates, 117 (2003) 160–169. doi:10.1016/S0378-7753(03)00029-6.

[49] M. Safari, M. Morcrette, A. Teyssot, C. Delacourt, Multimodal physics-based aging model

for life prediction of Li-Ion batteries, J. Electrochem. Soc. 156 (2009) A145–A153. doi:10.1149/1.3043429.

[50] N. Omar, M.A. Monem, Y. Firouz, J. Salminen, J. Smekens, O. Hegazy, H. Gaulous, G. Mulder, P. Van den Bossche, T. Coosemans, J. Van Mierlo, Lithium iron phosphate based battery - Assessment of the aging parameters and development of cycle life model, Appl. Energy. 113 (2014) 1575–1585. doi:10.1016/j.apenergy.2013.09.003.

[51] P. Gambhire, K.S. Hariharan, A. Khandelwal, S.M. Kolake, T. Yeo, S. Doo, A physics based reduced order aging model for lithium-ion cells with phase change, J. Power Sources. 270 (2014) 281–291. doi:10.1016/j.jpowsour.2014.07.127.

[52] C. Kupper, W.G. Bessler, Multi-scale thermo-electrochemical modeling of performance and aging of a $LiFePO_4$ /graphite lithium-ion cell, J. Electrochem. Soc. 164 (2017) A304–A320. doi:10.1149/2.0761702jes.

[53] R. Darling, J. Newmann, Modeling side reactions in composite $Li_yMn_2O_4$ electrodes, J. Electrochem. Soc. 145 (1998) 990–998. doi:10.1149/1.1838376.

[54] C. Delacourt, M. Safari, Life simulation of a graphite/$LiFePO_4$ cell under cycling and storage, J. Electrochem. Soc. 159 (2012) A1283–A1291. doi:10.1149/2.049208jes.

[55] M. Safari, C. Delacourt, Simulation-based analysis of aging phenomena in a commercial graphite/$LiFePO_4$ Cell, J. Electrochem. Soc. 158 (2011) A1436–A1447. doi:10.1149/2.103112jes.

[56] Z. Li, J. Huang, B. Yann Liaw, V. Metzler, J. Zhang, A review of lithium deposition in lithium-ion and lithium metal secondary batteries, J. Power Sources. 254 (2014) 168–182. doi:10.1016/j.jpowsour.2013.12.099.

[57] H.J. Ploehn, P. Ramadass, R.E. White, Solvent diffusion model for aging of lithium-ion

battery cells, J. Electrochem. Soc. 151 (2004) A456. doi:10.1149/1.1644601.

[58] D. Anseán, M. Dubarry, A. Devie, B.Y. Liaw, V.M. García, J.C. Viera, M. Gonzalez, Operando lithium plating quantification and early detection of a commercial $LiFePO_4$ cell cycled under dynamic driving schedule, J. Power Sources. In press (2017). doi:10.1016/j.jpowsour.2017.04.072.

[59] J.C. Burns, D.A. Stevens, J.R. Dahn, In-situ detection of lithium plating using high precision coulometry, J. Electrochem. Soc. 162 (2015) A959–A964. doi:10.1149/2.0621506jes.

[60] M. Petzl, M.A. Danzer, Nondestructive detection, characterization, and quantification of lithium plating in commercial lithium-ion batteries, J. Power Sources. 254 (2014) 80–87. doi:10.1016/j.jpowsour.2013.12.060.

[61] S. Tippmann, D. Walper, L. Balboa, B. Spier, W.G. Bessler, Low-temperature charging of lithium-ion cells part I: Electrochemical modeling and experimental investigation of degradation behavior, J. Power Sources. 252 (2014) 305–316. doi:10.1016/j.jpowsour.2013.12.022.

[62] Y. Ji, Y. Zhang, C.-Y. Wang, Li-ion cell operation at low temperatures, J. Electrochem. Soc. 160 (2013) A636–A649. doi:10.1149/2.047304jes.

[63] M. Petzl, M. Kasper, M.A. Danzer, Lithium plating in a commercial lithium-ion battery - A low-temperature aging study, J. Power Sources. 275 (2015) 799–807. doi:10.1016/j.jpowsour.2014.11.065.

[64] A. Senyshyn, M.J. Mhlbauer, O. Dolotko, H. Ehrenberg, Low-temperature performance of Li-ion batteries: The behavior of lithiated graphite, J. Power Sources. 282 (2015) 235–240. doi:10.1016/j.jpowsour.2015.02.008.

[65] V. Zinth, C. Von Lüders, M. Hofmann, J. Hattendorff, I. Buchberger, S. Erhard, J. Rebelo-

Kornmeier, A. Jossen, R. Gilles, Lithium plating in lithium-ion batteries at sub-ambient temperatures investigated by in situ neutron diffraction, J. Power Sources. 271 (2014) 152–159. doi:10.1016/j.jpowsour.2014.07.168.

[66] T. Waldmann, A. Iturrondobeitia, M. Kasper, N. Ghanbari, F. Aguesse, E. Bekaert, L. Daniel, S. Genies, I.J. Gordon, M.W. Löble, E. De Vito, M. Wohlfahrt-Mehrens, Review—Post-mortem analysis of aged lithium-ion batteries: Disassembly methodology and physico-chemical analysis techniques, J. Electrochem. Soc. 163 (2016) 2149–2164. doi:10.1149/2.1211609jes.

[67] A. Friesen, S. Hildebrand, F. Horsthemke, M. Borner, R. Kl€opsch, P. Niehoff, F.M. Schappacher, M. Winter, Al_2O_3 coating on anode surface in lithium ion batteries: Impact on low temperature cycling and safety behavior, J. Power Sources. 363 (2017) 70–77. doi:10.1016/j.jpowsour.2017.07.062.

[68] M. Ouyang, Z. Chu, L. Lu, J. Li, X. Han, X. Feng, G. Liu, Low temperature aging mechanism identification and lithium deposition in a large format lithium iron phosphate battery for different charge profiles, J. Power Sources. 286 (2015) 309–320. doi:10.1016/j.jpowsour.2015.03.178.

[69] C. Uhlmann, J. Illig, M. Ender, R. Schuster, E. Ivers-Tiffée, In situ detection of lithium metal plating on graphite in experimental cells, J. Power Sources. 279 (2015) 428–438. doi:10.1016/j.jpowsour.2015.01.046.

[70] B. Stiaszny, J.C. Ziegler, E.E. Krauß, J.P. Schmidt, E. Ivers-Tiffée, Electrochemical characterization and post-mortem analysis of aged $LiMn_2O_4$-$Li(Ni_{0.5}Mn_{0.3}Co_{0.2})O_2$/graphite lithium ion batteries. Part I: Cycle aging, J. Power Sources. 251 (2014) 439–450. doi:10.1016/j.jpowsour.2013.11.080.

[71] B. Zhao, Y. Jiang, H. Zhang, H. Tao, M. Zhong, Z. Jiao, Morphology and electrical properties of carbon coated $LiFePO_4$ cathode materials, J. Power Sources. 189 (2009) 462–466. doi:10.1016/j.jpowsour.2008.12.069.

[72] M. Klett, R. Eriksson, J. Groot, P. Svens, K. Ciosek Högström, R.W. Lindström, H. Berg, T. Gustafson, G. Lindbergh, K. Edström, Non-uniform aging of cycled commercial $LiFePO_4$/graphite cylindrical cells revealed by post-mortem analysis, J. Power Sources. 257 (2014) 126–137. doi:10.1016/j.jpowsour.2014.01.105.

[73] T. Waldmann, M. Wilka, M. Kasper, M. Fleischhammer, M. Wohlfahrt-Mehrens, Temperature dependent ageing mechanisms in lithium-ion batteries - A Post-mortem study, J. Power Sources. 262 (2014) 129–135. doi:10.1016/j.jpowsour.2014.03.112.

[74] S.J. An, J. Li, Y. Sheng, C. Daniel, D.L. Wood Iii, Long-term lithium-ion battery performance improvement via ultraviolet light treatment of the graphite anode, J. Electrochem. Soc. 163 (2016) 2866–2875. doi:10.1149/2.0171614jes.

[75] W. Lu, C.M. López, N. Liu, J.T. Vaughey, A. Jansen, D.W. Dees, Overcharge effect on morphology and structure of carbon electrodes for lithium-ion batteries, J. Electrochem. Soc. 159 (2012) A566. doi:10.1149/2.jes035205.

[76] P. Arora, Mathematical Modeling of the lithium deposition overcharge reaction in lithium-ion batteries using carbon-based negative electrodes, J. Electrochem. Soc. 146 (1999) 3543. doi:10.1149/1.1392512.

[77] M. Tang, P. Albertus, J. Newman, Two-dimensional modeling of lithium deposition during cell charging, J. Electrochem. Soc. 156 (2009) A390. doi:10.1149/1.3095513.

[78] R.D. Perkins, A. V. Randall, X. Zhang, G.L. Plett, Controls oriented reduced order modeling of lithium deposition on overcharge, J. Power Sources. 209 (2012) 318–325.

doi:10.1016/j.jpowsour.2012.03.003.

[79] H. Ge, T. Aoki, N. Ikeda, S. Suga, T. Isobe, Z. Li, Y. Tabuchi, J. Zhang, Investigating lithium plating in lithium-ion batteries at low temperatures using electrochemical model with NMR assisted parameterization, J. Electrochem. Soc. 164 (2017) A1050–A1060. doi:10.1149/2.0461706jes.

[80] X.G. Yang, Y. Leng, G. Zhang, S. Ge, C.Y. Wang, Modeling of lithium plating induced aging of lithium-ion batteries: Transition from linear to nonlinear aging, J. Power Sources. 360 (2017) 28–40. doi:10.1016/j.jpowsour.2017.05.110.

[81] M.C. Smart, B. V. Ratnakumar, Lithium plating in lithium-ion cells, ECS Trans. 25 (36) (2010) 241–252. doi:10.1149/1.3393860.

Appendix

Table 12 Model parameters for BoL (LFP/graphite cells)

Category	Parameter	Negative electrode	Separator	Positive electrode	unit
Geometry and volume fractions	Thickness, δ	72×10^{-6}	20×10^{-6}	108×10^{-6}	m
	Particle radius, R_s	3.72×10^{-6}		0.475×10^{-6}	m
	Active material volume fraction, ε_s	0.5814		0.5589	
	Polymer phase volume fraction, ε_p	0.0369	0.5464	0.0243	
	Conductive filler volume fraction, ε_f	0.0069		0.0243	
	Porosity, ε_e	0.3749	0.4536	0.3925	
Li^+ concentrations	Stoichiometry at 0% *SOC*: $x_{0\%}$, $y_{0\%}$	0.02		0.84	
	Stoichiometry at 100% *SOC*: $x_{100\%}$, $y_{100\%}$	0.94		0.16	
	Average electrolyte concentration, c_e	1.2×10^3	1.2×10^3	1.2×10^3	mol m^{-3}
	Exchange current density coefficient, i_0	13.2×10^4		6.79×10^4	A m^{-2}
Kinetic and transport properties	Charge-transfer coefficient, α_a, α_c	0.5, 0.5		0.5, 0.5	
	Solid phase diffusion coefficient, D_s	Ds = f(T)			$m^2\ s^{-1}$
	Solid phase conductivity, σ	100		1	S m^{-1}
	Electrolyte phase Li^+ diffusion coefficient, D_e	De = f(T)			$m^2\ s^{-1}$
	Bruggeman's porosity exponent, p	1.5	1.5	1.5	
	Electrolyte phase ionic conductivity, κ	$\kappa = 1106c_e \exp\left(-8900c_e^{1.4}\right)$			S m^{-1}
	Li^+ transference number, t_0^+	0.363	0.363	0.363	

Equilibrium potential of LFP	$U_{equ+}(y) = 3.4323 + 0.8428\exp\left(-80.2493y^{1.3198}\right) + 3.2474\times10^{-6}\exp\left(20.2645y^{3.8003}\right) - 3.2482\times10^{-6}\exp\left(20.2646y^{3.7995}\right)$

Table 13 Model parameters for EoL (LFP/graphite cells)

Parameter	Value	Source
Exchange current density of side reaction, $i_{0,side}$ (A m^{-2})	2.28 × 10^{-7} at 25°C 2.62× 10^{-7} at 40°C 2.73 × 10^{-7} at 55°C	Optimized by comparing simulation to the self-discharge data
Standard equilibrium potential of side reaction, $U^{\Theta}_{eq,side}$ (V)	0.2	Optimized by comparing simulation to the experimental data
Molar volume of SEI, $\tilde{V}_{SEI}$ (mol m^{-3})	2×10^{6}	Obtained by assuming the initial thickness of SEI is 2 nm
Ionic conductivity of SEI, κ_{SEI} (S m^{-1})	4×10^{-7}	Optimized by comparing simulation to the terminal voltage under cycling
isolation rate of active anode materials due to SEI, k_s	15	Optimized by comparing simulation to measured capacity fade
molar volume of DL, $\tilde{V}_{DL}$ (mol m^{-3})	7.56×10^{9}	Used from literature [33]
ionic conductivity of DL, κ_{DL} (S m^{-1})	0.1	Optimized by comparing simulation to the terminal voltage under cycling
molar volume of electrolyte, $\tilde{V}_e$ (mol m^{-3})	3.25×10^{8}	Optimized by comparing simulation to the terminal voltage under cycling

Table 14 List of model parameters (a: Manufacture; b: model validation; c: literature) for NMC/Carbon cells

Category	Parameter	Negative electrode	Separator	Positive electrode	unit	
Geometry and volume fractions	Thickness, δ	84×10^{-6}	8.9×10^{-6}	77.5×10^{-6}	m	a
	Particle radius, R_s	10.7×10^{-6}		17.5×10^{-6}	m	a
	Active material volume fraction, ε_s	0.7033		0.6748		a
	Porosity, ε_e	0.247	0.5	0.243		a
Li^+ concentrations	Stoichiometry at 0% *SoC*: $x_{0\%}$, $y_{0\%}$	0.3		0.81		b
	Stoichiometry at 100% *SoC*: $x_{100\%}$, $y_{100\%}$	0.77		0.49		b
	Maximum electrode concentration $c_{s,max}$	30.5×10^3		49.8×10^3	mol m^{-3}	a
	Average electrolyte concentration, c_e	1.2×10^3	1.2×10^3	1.2×10^3	mol m^{-3}	a
Kinetic and transport properties	Exchange current density coefficient, i_0	13.2×10^4		6.79×10^4	A m^{-2}	c
	Charge-transfer coefficient, α_a, α_c	0.5, 0.5		0.5, 0.5		c
	Solid phase diffusion coefficient, D_s	Ds = f(T)			m^2 s^{-1}	b
	Solid phase conductivity, σ	100		10	S m^{-1}	c
	Electrolyte phase Li^+ diffusion coefficient, D_e	De = f(T)			m^2 s^{-1}	b
	Bruggeman's porosity exponent, p	1.5	1.5	1.5		c
	Electrolyte phase ionic conductivity, κ	$\kappa = 1106c_e\exp\left(-8900c_e^{1.4}\right)$			S m^{-1}	c
	Li^+ transference number, t_0^+	0.363	0.363	0.363		c
	Equilibrium potential of anode	$U_{eq-}(y) = 8.00229 + 5.0647x - 12.578x^{0.5} - 8.6322\times10^{-4}x^{-1} + 2.1765\times10^{-5}x^{1.5} - 0.46016\exp(15\times(0.06-x)) - 0.55364\exp(-2.4326\times(x-0.92))$				c
Lithium deposition reaction model	Exchange current density of lithium deposition reaction, $i_{0,side}$ (A m^{-2})	4.55×10^{-8} at -20°C 5.0×10^{-8} at -25°C 8.51×10^{-8} at -30°C				b
	Standard equilibrium potential of lithium plating, $U_{eq,p}$ (V)	0				c

Molar volume of Li, $\widetilde{V}_{Li}$ (mol m^{-3})	7.69×10^{4}	c
isolation rate of active anode materials due to lithium plating, k_s	10	b
molar volume of electrolyte, $\widetilde{V}_e$ (mol m^{-3})	3.25×10^{8}	c